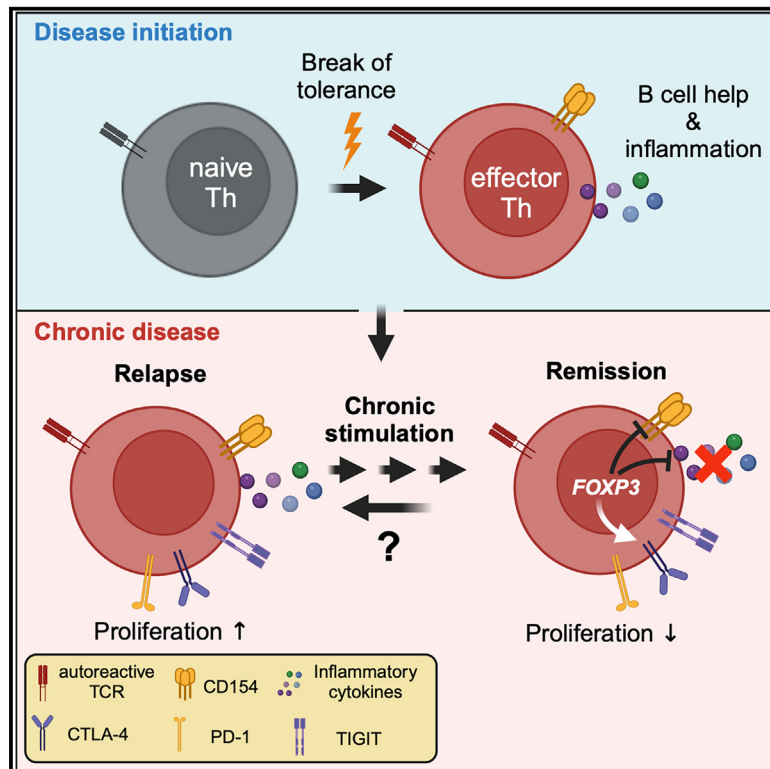


# Immunity

## Autoantigen-specific CD4<sup>+</sup> T cells acquire an exhausted phenotype and persist in human antigen-specific autoimmune diseases

### Graphical abstract



### Authors

Carina Saggau, Petra Bacher, Daniela Esser, ..., Friedemann Paul, Frank Leyholdt, Alexander Scheffold

### Correspondence

alexander.scheffold@uksh.de

### In brief

CD4<sup>+</sup> T cells are important contributors to autoimmune disease pathology. Saggau, Bacher et al. characterize autoantigen-specific CD4<sup>+</sup> T helper cells in various human autoimmune diseases, revealing features of exhaustion. These findings provide insight into CD4<sup>+</sup> T cell exhaustion in the context of chronic stimulation and suggest a role for exhausted autoantigen-specific CD4<sup>+</sup> Th cells in promoting humoral autoimmunity.

### Highlights

- Auto-Th cells from AID patients have an exhausted-like (ThEx) phenotype
- Auto-ThEx cell frequencies are stable for years despite successful therapy
- ThEx cells respond to checkpoint inhibition and provide B cell help
- ThEx phenotype development during chronic stimulation *in vitro* is regulated by FOXP3



Article

# Autoantigen-specific CD4<sup>+</sup> T cells acquire an exhausted phenotype and persist in human antigen-specific autoimmune diseases

Carina Saggau,<sup>1,30</sup> Petra Bacher,<sup>1,2,30</sup> Daniela Esser,<sup>3</sup> Mahdi Rasa,<sup>1,4</sup> Silja Meise,<sup>1</sup> Nicola Mohr,<sup>1</sup> Nora Kohlstedt,<sup>1</sup> Andreas Hutloff,<sup>1,2</sup> Sarah-Sophie Schacht,<sup>1</sup> Justina Dargvainiene,<sup>3</sup> Gabriela Rios Martini,<sup>1,2</sup> Klarissa H. Stürner,<sup>3,5</sup> Ina Schröder,<sup>3</sup> Robert Markewitz,<sup>3</sup> Johannes Hartl,<sup>6</sup> Maria Hastermann,<sup>7</sup> Ankeliën Duchow,<sup>7</sup> Patrick Schindler,<sup>7</sup> Mareike Becker,<sup>8,9</sup> Carolin Bautista,<sup>10</sup> Judith Gottfreund,<sup>11</sup> Jörn Walter,<sup>11</sup> Julia K. Polansky,<sup>12,13</sup>

(Author list continued on next page)

<sup>1</sup>Institute of Immunology, Christian-Albrechts-University of Kiel and University Hospital Schleswig-Holstein (UKSH), Kiel, Germany

<sup>2</sup>Institute of Clinical Molecular Biology, Christian-Albrechts-University of Kiel, Kiel, Germany

<sup>3</sup>Institute of Clinical Chemistry, University Hospital Schleswig-Holstein, Kiel, Germany

<sup>4</sup>Leibniz Institute on Aging – Fritz Lipmann Institute (FLI), Jena, Germany

<sup>5</sup>Department of Neurology, University Hospital Schleswig-Holstein, Kiel, Germany

<sup>6</sup>Department of Medicine, University Medical Center Hamburg-Eppendorf, 20246 Hamburg, Germany

<sup>7</sup>Experimental and Clinical Research Center, Max Delbrück Center for Molecular Medicine and Charité Universitätsmedizin Berlin, Berlin, Germany

<sup>8</sup>Institute of Experimental Dermatology, Lübeck, Germany

<sup>9</sup>Department of Pediatric Dermatology, Catholic Children's Hospital Wilhelmstift, Hamburg, Germany

<sup>10</sup>Department of Dermatology, Allergy and Venerology, University Hospital Schleswig-Holstein, Campus Lübeck, Lübeck, Germany

<sup>11</sup>Department of Genetics and Epigenetics, Saarland University, Saarbrücken, Germany

<sup>12</sup>Berlin Institute of Health (BIH) at Charité Universitätsmedizin Berlin, BIH Center for Regenerative Therapies (BCRT), Augustenburger Platz 1, 13353 Berlin, Germany

<sup>13</sup>German Rheumatism Research Centre, a Leibniz Institute (DRFZ), Charité Platz 1, 10117 Berlin, Germany

<sup>14</sup>Neuroimmunology and MS Research Section (NIMS), Neurology Clinic, University of Zurich, University Hospital Zurich, Zurich, Switzerland

<sup>15</sup>Cellerys AG, Wagistrasse 21, 8952 Schlieren, Switzerland

<sup>16</sup>Leibniz Institute for Science and Mathematics Education, Kiel, Germany

<sup>17</sup>Mikrobiologisches Institut – Klinische Mikrobiologie, Immunologie und Hygiene, Universitätsklinikum Erlangen und Friedrich-Alexander-Universität (FAU) Erlangen-Nürnberg, Wasserturmstr. 3/5, 91054 Erlangen, Germany

<sup>18</sup>DRESDEN-concept Genome Center, Technology Platform at the Center for Molecular and Cellular Bioengineering (CMCB), Technical University of Dresden, Dresden, Germany

<sup>19</sup>Miltenyi Biotec B.V. & Co. KG, Friedrich-Ebert-Straße 68, 51429 Bergisch Gladbach, Germany

<sup>20</sup>Department of Dermatology and Allergy, University Hospital Schleswig-Holstein, Kiel, Germany

<sup>21</sup>Institute of Experimental Dermatology, University of Lübeck, Department of Dermatology, University Hospital Schleswig-Holstein, Campus Lübeck, Lübeck, Germany

(Affiliations continued on next page)

## SUMMARY

Pro-inflammatory autoantigen-specific CD4<sup>+</sup> T helper (auto-Th) cells are central orchestrators of autoimmune diseases (AIDs). We aimed to characterize these cells in human AIDs with defined autoantigens by combining human leukocyte antigen (HLA)-tetramer-based and activation-based multidimensional *ex vivo* analyses. In aquaporin4-antibody-positive neuromyelitis optica spectrum disorder (AQP4-NMOSD) patients, auto-Th cells expressed CD154, but proliferative capacity and pro-inflammatory cytokines were strongly reduced. Instead, exhaustion-associated co-inhibitory receptors were expressed together with FOXP3, the canonical regulatory T cell (Treg) transcription factor. Auto-Th cells responded *in vitro* to checkpoint inhibition and provided potent B cell help. Cells with the same exhaustion-like (ThEx) phenotype were identified in soluble liver antigen (SLA)-antibody-autoimmune hepatitis and BP180-antibody-positive bullous pemphigoid, AIDs of the liver and skin, respectively. While originally described in cancer and chronic infection, our data point to T cell exhaustion as a common mechanism of adaptation to chronic (self-)stimulation across AID types and link exhausted CD4<sup>+</sup> T cells to humoral autoimmune responses, with implications for therapeutic targeting.



Mingxing Yang,<sup>12</sup> Reza Naghavian,<sup>14,15</sup> Mareike Wendorff,<sup>2,16</sup> Ev-Marie Schuster,<sup>17</sup> Andreas Dahl,<sup>18</sup> Andreas Petzold,<sup>18</sup> Susanne Reinhardt,<sup>18</sup> Andre Franke,<sup>2</sup> Marek Wieczorek,<sup>19</sup> Lea Henschel,<sup>19</sup> Daniel Berger,<sup>19</sup> Guido Heine,<sup>20</sup> Maike Holtsche,<sup>21</sup> Vivien Häußler,<sup>22</sup> Christian Peters,<sup>1</sup> Enno Schmidt,<sup>21</sup> Simon Fillatreau,<sup>23,24,25</sup> Dirk H. Busch,<sup>26</sup> Klaus-Peter Wandinger,<sup>3</sup> Kilian Schober,<sup>17,27</sup> Roland Martin,<sup>14,15,28,29</sup> Friedemann Paul,<sup>7,30</sup> Frank Leyboldt,<sup>3,5,30</sup> and Alexander Scheffold<sup>1,30,31,\*</sup>

<sup>22</sup>Clinic and Polyclinic for Neurology, University Medical Center Hamburg-Eppendorf, 20246 Hamburg, Germany

<sup>23</sup>Université Paris Cité, CNRS, INSERM, Institut Necker Enfants Malades-INEM, 75015 Paris, France

<sup>24</sup>Université Paris Cité, Faculté de Médecine, Paris, France

<sup>25</sup>AP-HP, Hôpital Necker-Enfants Malades, Paris, France

<sup>26</sup>Institute for Medical Microbiology, Immunology and Hygiene, Technical University of Munich, Munich, Germany

<sup>27</sup>Medical Immunology Campus Erlangen, Friedrich-Alexander-Universität (FAU) Erlangen-Nürnberg, Schlossplatz 1, 91054 Erlangen, Germany

<sup>28</sup>Institute of Experimental Immunology, University of Zurich, Wintherturerstrasse 191, 8057 Zurich, Switzerland

<sup>29</sup>Department of Clinical Neuroscience, Karolinska Institute, Center for Molecular Medicine, Karolinska University Hospital, Stockholm, Sweden

<sup>30</sup>These authors contributed equally

<sup>31</sup>Lead contact

\*Correspondence: [alexander.scheffold@uksh.de](mailto:alexander.scheffold@uksh.de)

<https://doi.org/10.1016/j.immuni.2024.08.005>

## INTRODUCTION

Autoimmune diseases (AIDs) result from the breakdown of self-tolerance mechanisms, leading to a chronic inflammatory autoimmune reaction and to tissue destruction. This process is orchestrated by autoantigen-specific CD4<sup>+</sup> T helper (auto-Th) cells via pro-inflammatory cytokines and B cell help, resulting in autoantibody production,<sup>1–3</sup> as demonstrated in multiple animal models of AIDs. In humans, the extremely low frequency (10<sup>–4</sup> to 10<sup>–5</sup> CD4<sup>+</sup> T cells<sup>4</sup>) of autoantigen-specific T cells and technical restrictions regarding their identification have generated considerable variability.<sup>4–7</sup> Autoreactive T cells are detected in both, healthy donors (HDs) and AID patients,<sup>8</sup> but displayed increased proliferation and pro-inflammatory cytokine production in AID.<sup>1,9</sup> These findings largely rely on functional assays, involving prolonged *in vitro* antigen activation, which modulate the cellular phenotype and restrict the analysis to T cell subsets with measurable antigen reactivity. Only a few direct *ex vivo* analyses using peptide/HLA tetramers are available. In these, autoantigen-specific effector and regulatory T cells (Tregs) are seen in HDs<sup>10–12</sup> and AID patients,<sup>13–15</sup> with either reduced numbers of Tregs<sup>12,14,15</sup> or with a distinctive peripheral T helper (Tph) cell phenotype in AID patients, including pro-inflammatory cytokine production.<sup>16,17</sup> Indeed, pro-inflammatory auto-Th cells play a central role by initiating pathogenic autoantibody production and supporting tissue inflammation in animal models.<sup>18–23</sup> Auto-Th cells with a pro-inflammatory or B cell helper profile are seen in AID patients,<sup>16,24–31</sup> but comprehensive *ex vivo* analyses are missing.

How such pro-inflammatory auto-Th cells cope with chronic stimulation in human AID is not clear. Other situations of chronic antigen stimulation, such as cancer or chronic viral infections, result in T cell exhaustion, characterized by the progressive loss of cytokine expression, proliferative potential, and upregulation of inhibitory receptors (immune checkpoints). Exhaustion can be partially reversed by immune checkpoint inhibitors, providing the basis for successful therapies against cancer.<sup>32,33</sup> T cell exhaustion may play a role in AIDs,<sup>33–35</sup> and exhausted autoantigen-specific CD8<sup>+</sup>

T cells were detected in murine and human type 1 diabetes (T1D).<sup>35,36</sup> However, exhausted auto-Th cells may escape standard detection techniques,<sup>4–7</sup> and it is currently unclear whether auto-Th cell exhaustion occurs in human AIDs.<sup>37</sup>

Here, we have addressed these questions by characterizing directly *ex vivo* auto-Th cells in four different antigen-specific AIDs, targeting the brain, optic nerve and spinal cord<sup>38,39</sup> (aquaporin4-antibody-positive neuromyelitis optica spectrum disorder [AQP4-NMOSD]) and myelin oligodendrocyte glycoprotein antibody-associated disease [MOGAD]), the liver (autoimmune hepatitis [AIH]), and the skin (bullous pemphigoid [BP]), respectively. All four AIDs are characterized by highly disease-specific autoantibodies targeting the astroglial water channel AQP4,<sup>40</sup> the oligodendroglial outer-myelin sheath glycoprotein MOG, the soluble liver antigen (SLA),<sup>16,29,31</sup> and collagen XVII (BP180),<sup>30,41</sup> respectively. Primarily, we studied patients with the prototypic, highly chronic and relapse-prone disease AQP4-NMOSD, allowing us to apply two complementary technologies for direct *ex vivo* auto-Th analysis, antigen-reactive T cell enrichment (ARTE),<sup>42–44</sup> and AQP4-peptide/HLA class II tetramers, developed herein. High-affinity auto-Th cells were increased in patients and indeed displayed an exhaustion-like (ThEx) phenotype according to molecular, phenotypic, and functional analyses. However, they retained potent B cell helper activity, illustrated by *ex vivo* expression of CD40 ligand (CD154) and functional assays *in vitro*. The same phenotype was prevalent in auto-Th cells from patients with AIH or BP but not in patients with MOGAD, an AID targeting the same organ as AQP4-NMOSD but considerably less chronic and more prone to monophasic courses. Thus, our results identify exhaustion-like inactivation as a common pathway of autoantigen-specific T cells in chronic AIDs, which has important implications for their therapeutic targeting.

## RESULTS

### Increased frequencies of AQP4-specific effector memory CD4<sup>+</sup> T cells in AQP4-NMOSD patients

To provide an unbiased *ex vivo* characterization of rare autoreactive T cells, we used ARTE. ARTE allowed the

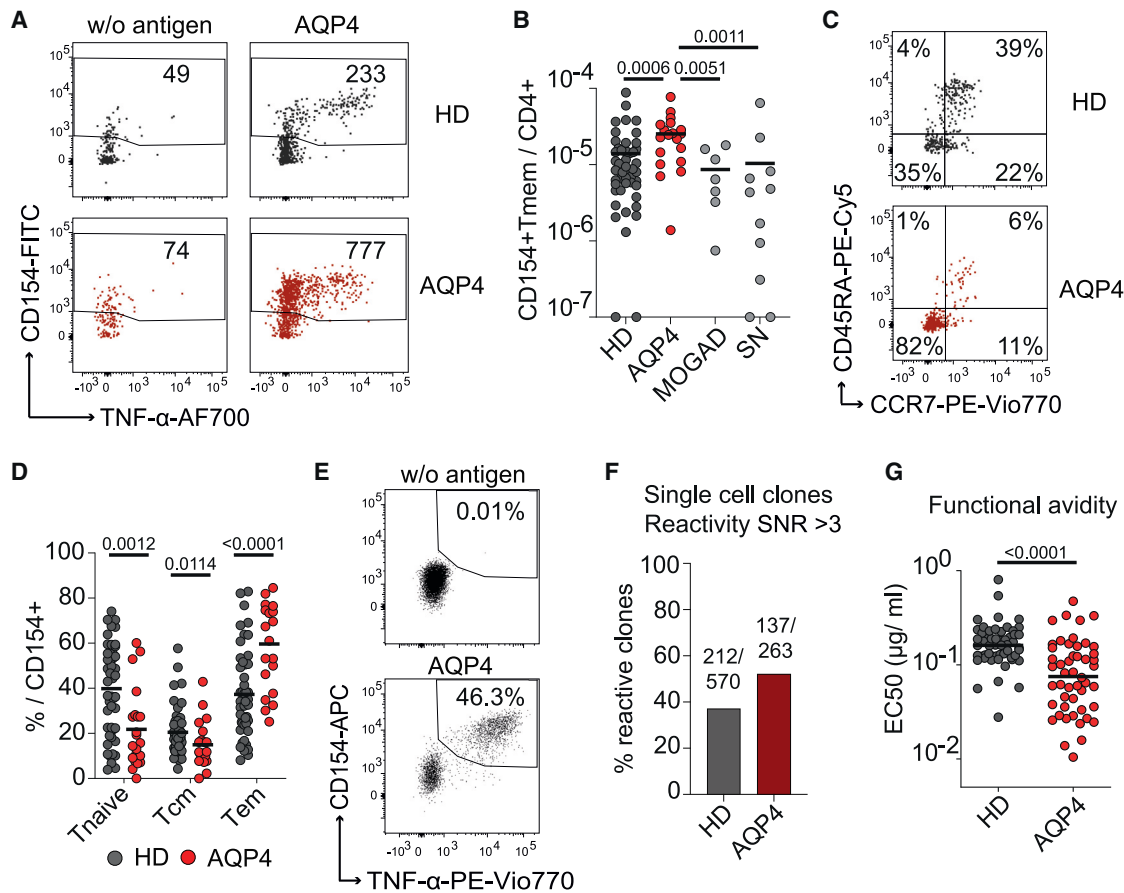


**Figure 1. Increased frequencies of AQP4-reactive CD4<sup>+</sup> T cells in NMOSD patients**

(A) Dot plot examples of the *ex vivo* detection of AQP4-reactive CD4<sup>+</sup> T cells by ARTE. Cell counts after magnetic enrichment from  $4 \times 10^7$  PBMCs are indicated. (B) Frequencies of AQP4-reactive CD154<sup>+</sup>CD45RA<sup>-</sup> memory CD4<sup>+</sup> T cells (Tmem) in healthy donors (HDs,  $n = 48$ ) and NMOSD patients,  $n = 38$  (AQP4,  $n = 20$ ; MOGAD,  $n = 7$ ; SN,  $n = 11$ ). (C) Dot plot examples of AQP4-reactive CD154<sup>+</sup> cells from HD and an AQP4-NMOSD patient (AQP4). Percentages of cells within CD154<sup>+</sup> are indicated. (D) Proportion of naive, central memory, and effector memory T cells within AQP4-reactive CD154<sup>+</sup> T cells in HD ( $n = 48$ ) and AQP4-NMOSD patients (AQP4,  $n = 20$ ). (E–G) AQP4-reactive CD154<sup>+</sup> single-cell clones from HD and AQP4-NMOSD patients were restimulated with AQP4 and graded antigen doses. (E) Dot plot example after single-cell clone restimulation with AQP4 or without antigen. Percentages of reactive CD154<sup>+</sup>TNF $\alpha$ <sup>+</sup> cells are indicated. (F) Proportion of AQP4-reactive T cell clones from HD and AQP4-NMOSD patients (signal-to-noise ratio (SNR) >3% and reactivity > 5%). (G) EC<sub>50</sub> values were calculated from dose-response curves from HD (HD,  $n = 54$ ) and AQP4-NMOSD patients (AQP4,  $n = 49$ ). Each symbol in (B) and (D) represents one donor, each symbol in (G) represents one T cell clone, and horizontal lines indicate mean in (B), (D), and (G). Statistical differences: two-tailed Mann-Whitney test in (B), (D), and (G). Significance was set at  $p < 0.05$ .

characterization of foreign antigen-specific<sup>42–44</sup> and autoantigen-specific T cells<sup>42,45,46</sup> with high sensitivity and precision (Figures S1A and S1B). AQP4-NMOSD<sup>47</sup> patients were prospectively recruited independent of whether in stable remission ( $n = 22$ , 79%) or during active disease flares ( $n = 6$ , 21%). Control cohorts were also prospectively recruited: MOGAD<sup>48,49</sup> ( $n = 25$ ) is a distinct central nervous system and glial autoantigen-specific demyelinating disease that is less chronic and relapse-prone, compared with AQP4-NMOSD, autoantibody double-seronegative (SN-)NMOSD ( $n = 11$ ), a heterogeneous group of patients without detection of glial autoantibodies,<sup>47</sup> and HDs ( $n = 65$ ) (clinical information is provided in Tables S1 and S2). Peripheral blood mononuclear cells (PBMCs) from patients (AQP4-NMOSD,  $n = 19$ ; MOGAD,  $n = 10$ ; and SN-NMOSD,  $n = 11$ ) and HDs ( $n = 48$ )

were stimulated with AQP4 peptide pools for 7 h, and reactive T cells were detected according to upregulation of CD154 (CD40L). CD154<sup>+</sup> cells were magnetically enriched from 25 to 50 million PBMCs to detect T cells at low frequencies (detection limit = 1 in  $10^6$ ).<sup>4,42</sup> AQP4-reactive T cells were identified in patients and HDs at frequencies between  $10^{-6}$  and  $10^{-4}$  (Figures 1A and 1B). Significantly increased frequencies of AQP4-specific T cells were detected in AQP4-NMOSD patients versus controls (Figure 1B). Furthermore, AQP4-reactive T cells from AQP4-NMOSD patients had mainly an effector memory phenotype (CD45RA<sup>-</sup>CCR7<sup>-</sup>), whereas naive and central memory phenotypes were reduced, compared with HDs (Figures 1C and 1D). To confirm their antigen-specificity, *ex vivo* antigen-reactive T cell-enriched AQP4-reactive memory T cells were cloned from individual

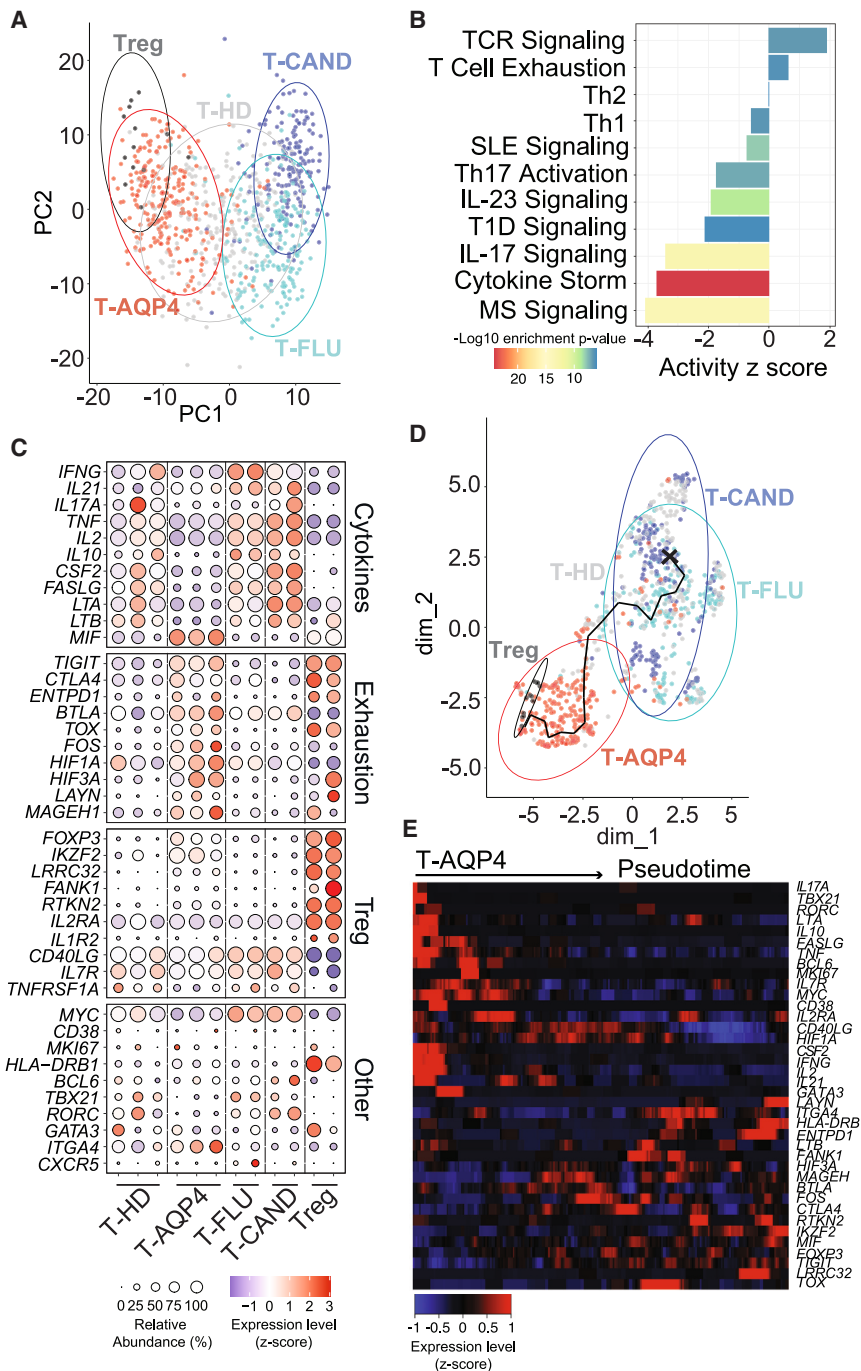


**Figure 2. Single-cell RNA sequencing of human AQP4-reactive CD4<sup>+</sup> T cells**

CD154<sup>+</sup> T cells specific for AQP4 ( $n = 3$  each), *C. albicans* (MP65) ( $n = 2$ ), or influenza (HA) ( $n = 2$ ), and phorbol 12-myristate 13-acetate (PMA)- and ionomycin-activated CD137<sup>+</sup> regulatory T cells (Tregs) from two NMO/MSD patients were FACS sorted into 96-well plates and analyzed by single-cell RNA sequencing (Smart-seq2).

(A) PCA plot comparing the various T cell populations (for PC1, 2.9% variance explained; for PC2, 1.9% variance explained).

(B) The top enriched canonical pathways based on differentially expressed genes (adjusted  $p < 0.05$ ) between healthy donors and NMO/MSD patients, as determined by ingenuity pathway analysis (IPA).

(C) Normalized expression of selected marker genes.

(D) Trajectory plot of cells ordered along the pseudotime overlaid with the color code representing the individual specificities used in (A).

(E) Heatmap depicting gene expression of selected marker genes of T-AQP4 cells along the trajectory.

furthermore have a higher functional affinity for AQP4 and are enriched in effector/memory cells.

### AQP4-specific CD4<sup>+</sup> T cells from NMO/MSD patients display a unique ThEx phenotype

Next, we aimed to deeply characterize these AQP4-specific T cells. We performed single-cell RNA sequencing (scRNA-seq) of *ex vivo* FACS-purified CD154<sup>+</sup>CD45RO<sup>+</sup> AQP4-specific memory T cells from AQP4-NMO/MSD patients (T-AQP4) and healthy (T-HD) donors ( $n = 3$  per group). We sorted the memory T cell subsets to focus on the disease-relevant cells. Owing to the limited number of specific T cells, a plate-based Smart-seq2 (Switching mechanism at the 5' end of the RNA transcript) approach was used, restricting the analysis to a maximum of 96 sorted cells per sample. For comparison, FACS-purified CD154<sup>+</sup> *C. albicans* MP65-specific (T-CAND), influenza HA-specific (T-FLU), and polyclonally activated CD137<sup>+</sup>CD25<sup>+</sup>CD127<sup>-</sup> Tregs ( $n = 2$  each) were used, resembling prototypic effector T cells (Th1, Th17) and Tregs, respectively.<sup>43,50,51</sup> Principle-component analysis (PCA) revealed a clear difference between AQP4-NMO/MSD patients and HDs and identified a distinct cluster for T-AQP4, clearly separated from both pathogen-specific effector T cells, T-CAND, and T-FLU (Figure 2A). These data indicate that autoreactive CD4<sup>+</sup> T cells have a distinct molecular profile in this AID.

Interestingly, ingenuity pathway analysis (IPA) between T-AQP4 and T-HD revealed that several pathways related to

fluorescence-activated cell sorting (FACS)-sorted cells from 14 AQP4-NMO/MSD patients ( $n = 263$ ) and 12 HDs ( $n = 570$ ), using optimized protocols (see STAR Methods section). Of these clones, 52.5% and 38.4%, respectively, reacted against AQP4 (Figures 1E and 1F). We also measured T cell antigen avidity of these clones via graded AQP4 peptide restimulation. Increased functional avidity was observed from AQP4-NMO/MSD patient-derived versus HD-derived T cell clones (Figure 1G). In conclusion, AQP4-NMO/MSD patients displayed an increased abundance of AQP4-reactive CD4<sup>+</sup> T cells, which

cytokine signaling and AID signaling were negatively associated with T-AQP4. In contrast, pathways related to exhaustion and T cell receptor (TCR) signaling were instead activated within T-AQP4 (Figure 2B). Gene expression profile comparison confirmed these associations (Figure 2C; top 50 differentially expressed genes in Figure S2A). Gene signature analysis suggested an enrichment of Tfh as well as Treg but a reduction of effector T cell marker genes in T-AQP4 (Figure S3D). T-AQP4 displayed a lower expression of inflammatory mediators (including *IFNG*, *IL17A*, *TNF*, *IL2*, *CSF2*, *FASLG*, *LTA*, and *LTB*) and a downregulation of Th1, Th2, Th17 as well as T follicular helper (Tfh) lineage-defining transcription factors (*TBX21*, *GATA3*, and *RORC*). In particular, the Tfh signature genes (*CXCR5*, *BCL6*, and *IL21*) were reduced or absent. The only cytokine strongly expressed in T-AQP4 was macrophage migration inhibitory factor (*MIF*), which has been reported previously to contribute to AQP4-NMOSD disease severity.<sup>52</sup> In addition, *ITGA4* (coding for integrin- $\alpha 4$ ) was upregulated exclusively in T-AQP4. Integrin- $\alpha 4$  is a key adhesion molecule for memory T cells required for crossing the blood-brain barrier, suggesting that T-AQP4 has enhanced capacity to migrate to the brain tissue. However, genes characteristic for T cell exhaustion were upregulated in T-AQP4, including inhibitory receptor genes such as *TIGIT* and *CTLA4*, but also *ENTPD1*, *BTLA*, *LAYN*, and *MAGEH1*, as well as transcription factors such as *TOX*, *FOS*, *HIF1A*, and *HIF3A*. Of note, the Treg signature genes *FOXP3* and *IKZF2* were also upregulated in T-AQP4. However, T-AQP4 differed from natural Tregs, as both *FOXP3* and *IKZF2* were expressed at a much lower level compared with Tregs, and several other Treg signature genes such as *IL2RA*, *LRRC32*, *IL1R2*, *RTKN2*, or *FANK1* were decreased or absent. In contrast, key Th cell molecules such as *CD40L* or *IL7R*—which are suppressed in Tregs—were expressed by T-AQP4.

Importantly, genes indicating ongoing T cell activation *in vivo*, such as *MKI67*, *MYC*, *CD38*, or *HLA-DRB1*,<sup>43,44,53</sup> were not expressed at a higher level in T-AQP4. This observation, together with the high expression of inhibitory receptors and low cytokine expression in these cells, suggests that autoreactive CD4<sup>+</sup> T cells are functionally exhausted in AQP4-NMOSD.

To investigate the potential developmental origin of the T-AQP4 cells, we performed a pseudotime trajectory analysis using the single-cell transcriptome data, which revealed an evolutionary path from classical effector T cells (T-FLU and T-CAND) to T-AQP4, associated with the progressive downregulation of pro-inflammatory cytokines (*CSF2*, *IFNG*, *IL17A*, *IL21*, *IL2*, *TNF*, *LTA*, *LTB*, and *FASLG*) and the acquisition of exhaustion and Treg genes (*ENTPD1*, *TOX*, *TIGIT*, *CTLA4*, *IKZF2*, and *FOXP3*) (Figure 2D). The same trajectory was also identified within the T-AQP4 cells (Figure 2E). To identify potential regulatory modules within this transcriptional profile, we performed an undirected bioinformatic protein network analysis based on all differentially expressed genes between T-HD and T-AQP4 (Figure S3). This identified *FOXP3* as the central node tightly connected with all downregulated cytokines, *FOS* and *MYC*. Upregulated exhaustion markers were also part of this network but were less closely connected to *FOXP3*, as compared with the cytokines. To confirm this, we analyzed the single-cell RNA expression data when grouping the cells into high, intermediate, or low expression of *FOXP3* (Figure S3A). This demonstrated a strong negative cor-

relation of *FOXP3* with *MYC* and the majority of inflammatory cytokine genes (*IFNG*, *IL21*, *IL17A*, *IL2*, *CSF2*, *FASL*, *LTA*, and *LTB*), whereas a positive correlation was seen for *MIF* and *ITGA4* as well as for some (e.g., *CTLA4*, *BTLA*, and *MAGEH1*) but not for all (e.g., *TIGIT*, *TOX*, *PDCD1*, *ENTPD1*, and *HIF1A/3A*) exhaustion/T-AQP4 markers. Overall, this suggested at least a partial *FOXP3*-dependent regulation of the ThEx signature, in particular the downregulation of cytokines. Next, scRNA-seq-derived TCR sequences were used to relate T cell clonality to the transcriptional profile. Clonally expanded (clone frequency > 1) and non-expanded (clone frequency = 1) T cells displayed a similar expression of the selected T cell-related genes (Figure S4B), suggesting that most of the identified T-AQP4 cells share hallmarks of the ThEx profile. Since only a subset of ThEx cells expressed *FOXP3*, we tested whether those may represent a separate, clonally distinct lineage. However, one-third of the TCRs were shared by *FOXP3*<sup>+</sup> and *FOXP3*<sup>-</sup> T cells (Figure S3C). Thus, *FOXP3* expression is not clonally restricted, supporting the hypothesis of a continuous developmental progression of ThEx cells, including the acquisition of *FOXP3* by a subset of cells. Overall, the scRNA-seq data identified an ThEx phenotype of autoreactive CD4<sup>+</sup> T cells from AQP4-NMOSD patients, characterized by stepwise loss of pro-inflammatory T cell cytokine expression and acquisition of co-inhibitory receptors (CIRs), as well as the expression of the canonical Treg signature genes *FOXP3* and *HELIOS*, but not other key Treg signature molecules.

### Cytometric protein profiling confirmed the ThEx phenotype of AQP4-reactive T cells

To confirm these gene expression patterns at the protein level, we used multicolor flow cytometry of antigen-specific T cells after ARTE, combining key cytokines, immune checkpoints, and transcription factors characteristic for exhausted and Tregs. Indeed, all analyzed inhibitory receptors (*TIGIT*, *PD1*, *CTLA-4*, and *CD39*) as well as *FOXP3* and *HELIOS* (Figures 3A and S4A) were upregulated in T-AQP4 cells, whereas the major inflammatory cytokines (tumor necrosis factor alpha [TNF- $\alpha$ ], interleukin [IL]-2, interferon [IFN]- $\gamma$ , IL-17A, and granulocyte-macrophage colony-stimulating factor [GM-CSF]) were reduced (Figures 3B and S4B). Of note, Tfh markers *CXCR5* and *IL-21* were also low and comparable to HDs (Figures 3B and S4D). Most of the AQP4-specific T cells expressed *TOX*, a transcription factor associated with T cell exhaustion, even though a similar frequency was observed in HDs (Figures S4C and S4D). Chronic (*CD38*, *ICOS*) T cell activation markers were either not differentially expressed between AQP4-NMOSD patients and HDs or were rather reduced in AQP4-NMOSD patients (Figures S4C and S4D). Importantly, all the identified exhaustion and Treg markers were restricted to memory type cells and not found on the small fraction of patient-derived naive AQP4-specific T cells (Figures S4E and S4F). We also analyzed the co-expression of inhibitory receptors and found that in AQP4-NMOSD patients, T cells expressing two or more checkpoint molecules simultaneously are strongly enriched (Figure 3C). Also, *FOXP3* expression was the highest within T-AQP4 cells expressing more than one inhibitory receptor (Figure 3D). Conversely, loss of cytokine expression (Figure 3E) as well as the acquisition of single (*CTLA-4* and *TIGIT*) or multiple inhibitory receptors and the

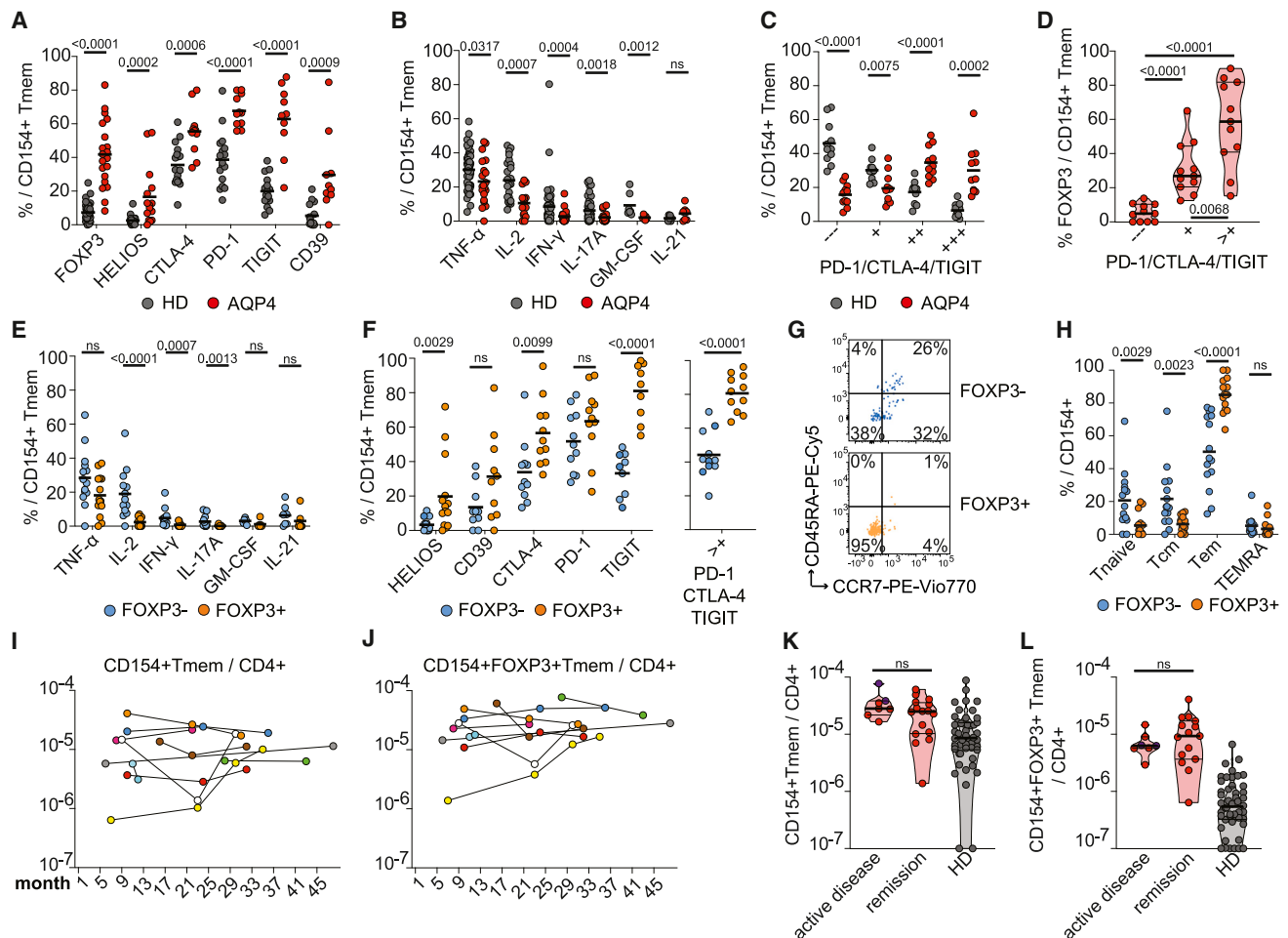


**Figure 3. AQP4-reactive T cells from NMOSD patients show an exhausted FOXP3<sup>+</sup> phenotype (ThEx)**

*Ex vivo* cytometric characterization of AQP4-reactive CD154<sup>+</sup> Tmem cells following ARTE.

(A and B) (A) *Ex vivo* proportion of indicated markers from healthy donors (HDs,  $n = 6-47$ ) and AQP4-NMOSD patients (AQP4,  $n = 10-20$ ) and (B) cytokine expression in healthy donors (HDs,  $n = 7-47$ ) and AQP4-NMOSD patients (AQP4,  $n = 7-20$ ).

(C) *Ex vivo* proportion of cells co-expressing the indicated number of co-inhibitory receptors within AQP4-reactive CD154<sup>+</sup> Tmem (HD,  $n = 11$ ; AQP4,  $n = 11$ ).

(D) Proportion of FOXP3<sup>+</sup> AQP4-reactive CD154<sup>+</sup> Tmem from AQP4-NMOSD patients expressing none, single, or >1 co-inhibitory receptor ( $n = 11$ ).

(E) Cytokine production of AQP4-reactive Foxp3<sup>-</sup> and Foxp3<sup>+</sup>CD154<sup>+</sup> Tmem in AQP4-NMOSD patients (AQP4,  $n = 6-14$ ).

(F) Proportion of AQP4-reactive FOXP3<sup>-</sup> and FOXP3<sup>+</sup>CD154<sup>+</sup> Tmem from AQP4-NMOSD patients (AQP4,  $n = 9-14$ ) expressing one or >1 co-inhibitory receptor.

(G) Dot plot examples of AQP4-reactive CD154<sup>+</sup> T cells from an AQP4-NMOSD patient; FOXP3<sup>+</sup> (orange dots) and FOXP3<sup>-</sup> cells (blue dots).

(H) Proportion of naive, central memory, and effector memory T cells and TEMRA cells within FOXP3<sup>+</sup> and FOXP3<sup>-</sup> AQP4-reactive CD154<sup>+</sup> T cells from AQP4-NMOSD patients ( $n = 15$ ).

(I and J) Kinetics of AQP4-reactive CD154<sup>+</sup> Tmem and (J) CD154<sup>+</sup>FOXP3<sup>+</sup> Tmem frequencies in AQP4-NMOSD patients ( $n = 10$ , different colored dots).

(K and L) Frequencies of CD154<sup>+</sup> Tmem and (L) CD154<sup>+</sup>FOXP3<sup>+</sup> Tmem in healthy donors (HDs,  $n = 48$ ) and AQP4-NMOSD patients grouped according to their clinical status: active disease ( $n = 7$ , new onset, or relapse, <3 months since last disease flare, one patient measured twice [purple dots], and stable remission [ $n = 15$ ]).

Each symbol in (A)–(F) and (H)–(L) represents one donor; horizontal lines indicate mean. Truncated violin plots with quartiles and range are shown in (D), (K), and (L). Statistical differences: two-tailed Mann-Whitney test or unpaired t test in (A)–(F), (H), (K), and (L). Decision was based on an upstream normal distribution test. ns = not significant; significance was set at  $p < 0.05$ .

Treg marker HELIOS (Figure 3F) were increased within the FOXP3<sup>+</sup> subset. FOXP3<sup>+</sup> T-AQP4 was almost completely confined to the effector memory subset (>70%) (Figures 3G and 3H). Similar to the transcriptional level (Figure 2), the ThEx cells also showed their Th cell origin and their clear phenotypic differences to Tregs at the protein level. They expressed CD127 and CD154 but not CD137, a marker for antigen-activated Tregs, while Treg signature proteins were absent

(CD25) or reduced (FOXP3, HELIOS, CTLA-4, TIGIT, and CD39) (Figures S4I and S4J). ThEx cells also expressed low levels of cytokines, which were completely absent in CD137<sup>+</sup> Tregs.

We also determined the frequency of T cells with a ThEx phenotype within the total memory CD4<sup>+</sup> T cell pool (total ThEx; Figures S5A–S5D). Total ThEx cells as defined by co-expression of >1 CIR are common in HDs, and their frequencies were reduced in AQP4-NMOSD (Figures S5B and S5C).

However, only about 1%–2% of all CD154<sup>+</sup>CD137<sup>−</sup> memory T cells expressed FOXP3 (Figure S5B), and these were enriched to up to 7% within the >1 CIR-positive subset (Figure S5D). These data show that ThEx development contributes to physiological immune regulation, but the induction of FOXP3 co-expression is restricted to a very small CD4<sup>+</sup> T cell subset, present in both HDs and AID patients.

Together, these data confirmed that T-AQP4 was characterized by simultaneous upregulation of various immune checkpoints, FOXP3, and HELIOS and by the loss of cytokine expression. Furthermore, FOXP3 expression marks a particularly pronounced ThEx phenotype of effector memory T cells. Indeed, as an individual marker, the frequency of FOXP3<sup>+</sup> cells within AQP4-reactive CD4<sup>+</sup> T cells alone was sufficient to discriminate AQP4-NMOSD patients from HDs as well as from MOGAD and SN-NMOSD patients at cellular level (Figure S4G).

We also had the opportunity to perform longitudinal measurements in patients over a period of up to 4 years. Within this period, the frequency of total AQP4-specific and FOXP3<sup>+</sup> AQP4-specific T cells did not show major alterations (Figures 3I and 3J). Next, we correlated ThEx frequencies and phenotype with the patients' clinical status. At the time of analysis, the majority of our AQP4-NMOSD cohort (Table S2) was on continuous therapy, whereas a small group was in the active disease phase ( $n = 7$ , new onset, or relapse, <3 months since last disease flare, one patient was analyzed twice during active disease). The frequency of total AQP4-specific and FOXP3<sup>+</sup> AQP4-specific T cells did not differ significantly between groups (Figures 3K and 3L), but patients in remission displayed an increased proportion of auto-Th cells expressing FOXP3 (Figure S5H).

Overall, cytometric plus transcriptional profiling and bioinformatic analysis suggest the stepwise acquisition of a ThEx phenotype (co-expression of multiple inhibitory receptors and loss of cytokines) and expression of FOXP3 as a novel marker for ThEx effector Th cells. Auto-ThEx cells have the capacity to persist long term in patients including in those who are in stable remission. Thus, we identified a novel phenotype of auto-Th cells, which may contribute to their persistence despite the chronic presence of antigen and/or immunosuppression.

### Checkpoint inhibition releases proliferation blockade

ThEx cells maintain the capacity to express CD154, representing the most important co-stimulatory molecule for B cells, essential for pathogenic antibody generation. However, the accumulation of inhibitory receptors on AQP4-reactive T cells suggested that ThEx cells may have reduced effector functions and proliferative capacity, as suggested by the absence of Ki67 expression (Figure 2C). Conversely, reduced proliferation of ThEx cells *in vivo* may prevent their deletion due to chronic antigen presentation and may reduce their sensitivity to anti-inflammatory therapies targeting actively dividing cells such as azathioprine or methotrexate, frequently used for AID treatment. To determine the functional potential of AQP4-specific ThEx, we tried to expand FACS-purified CD154<sup>+</sup>CD45RO<sup>+</sup> T cells *in vitro*. Consistent with the ThEx phenotype, we observed an extremely low cloning efficiency (mean 10.8%,  $n = 14$ ) of patient-derived AQP4-specific memory T cells, as compared with memory T cells from HDs (mean 41.9%,  $n = 12$ ) (Figure 4A). However, antibody blockade of CTLA-4 and PD-1 ligand interaction increased the cloning effi-

ciency of patient-derived memory T cells from approximately 11% (mean, range 0%–33.3%) to up to 35% (mean, range 20.8%–66.6%,  $n = 5$ ). In contrast, this checkpoint inhibition (CI) had no significant effect on the cloning efficiency of AQP4-specific memory T cells derived from HDs (Figure 4A). This indicates that CTLA-4 and PD-1 restrict the proliferation and expansion of AQP4-specific ThEx cells from AQP4-NMOSD patients and that this growth inhibition is at least partially reversible.

### Patient-derived AQP4-specific ThEx cell clones retain memory B cell helper activity

To further investigate their functionality, ThEx cell clones obtained by *in vitro* CTLA-4 and PD-1 blockade, as indicated above, were tested for *in vitro* B cell helper activity, as a key pathogenic function of autoantibody-mediated diseases. Heterologous HLA-matched naive and memory B cells were co-cultured with AQP4-specific T cell clones ( $n = 7$ ) derived from two NMOSD patients for 5 days in the presence of the AQP4 peptide pool. The majority of patient-derived AQP4-reactive CD4<sup>+</sup> T cell clones induced strong plasmablast formation (up to 82%; Figures 4B and 4C). In contrast, AQP4-specific memory T cell clones ( $n = 10$ ) derived from two HDs did not induce plasmablast formation (Figure 4C). No plasmablast formation was induced in naive B cells (Figure 4C), in accordance with the lack of the key Tfh signature genes BCL-6 and CXCR5 (Figures S5E and S5F). Thus, *in vitro* expanded AQP4-specific T cells represent Tph-like rather than Tfh-like features, as identified in AID patients before.<sup>16,17,54</sup> Plasmablast formation was strongly suppressed by the combined blockade of CD154 and IL-21 (from about 70–80% to 14%–40%) and was critically dependent on the presence of AQP4 peptides (Figures 4C, S5G, and S5H). Remarkably, most reactivated ThEx clones retained FOXP3 expression, albeit at reduced levels (Figures 4D and 4E). In addition, there was a clear trend, although not statistically significant because of the variability of replicates, toward higher expression of TIGIT and PD-1—two signature molecules of Tfh and Tph cells—on patient-derived memory T cell clones, compared with that of AQP4-specific clones from HDs, whereas CTLA-4 expression was similar (Figures 4D and 4E). Furthermore, patient-derived T cell clones also regained the ability to produce cytokines (Figures 4D and 4F compared with Figure 3B). Although IL-21 was undetectable intracellularly, *in vitro* blocking of IL-21 inhibited plasmablast formation (Figure 4C), suggesting that it is also produced at functionally relevant quantities. Finally, all analyzed AQP4-specific T cell clones were highly methylated at the Treg-specific demethylated region (TSDR) in the FOXP3 locus, similar to CD154<sup>+</sup> conventional T cells (Tcon) sorted *ex vivo* (Figure 4G). For comparison, the TSDR was highly demethylated in CD137<sup>+</sup> Tregs sorted *ex vivo* as well as Tregs after prolonged *in vitro* expansion, which is the molecular fingerprint of stable thymic derived Tregs. Thus, ThEx cells represent a therapy-resistant T cell subset with the capacity to persist in patients and to induce pathogenic B cell responses upon reactivation.

### Auto-ThEx cells are common in chronic organ-specific AIDs

Having observed the long-term persistence of ThEx cells in the highly chronic disease AQP4-NMOSD, we next wondered whether patients suffering from a related—albeit considerably

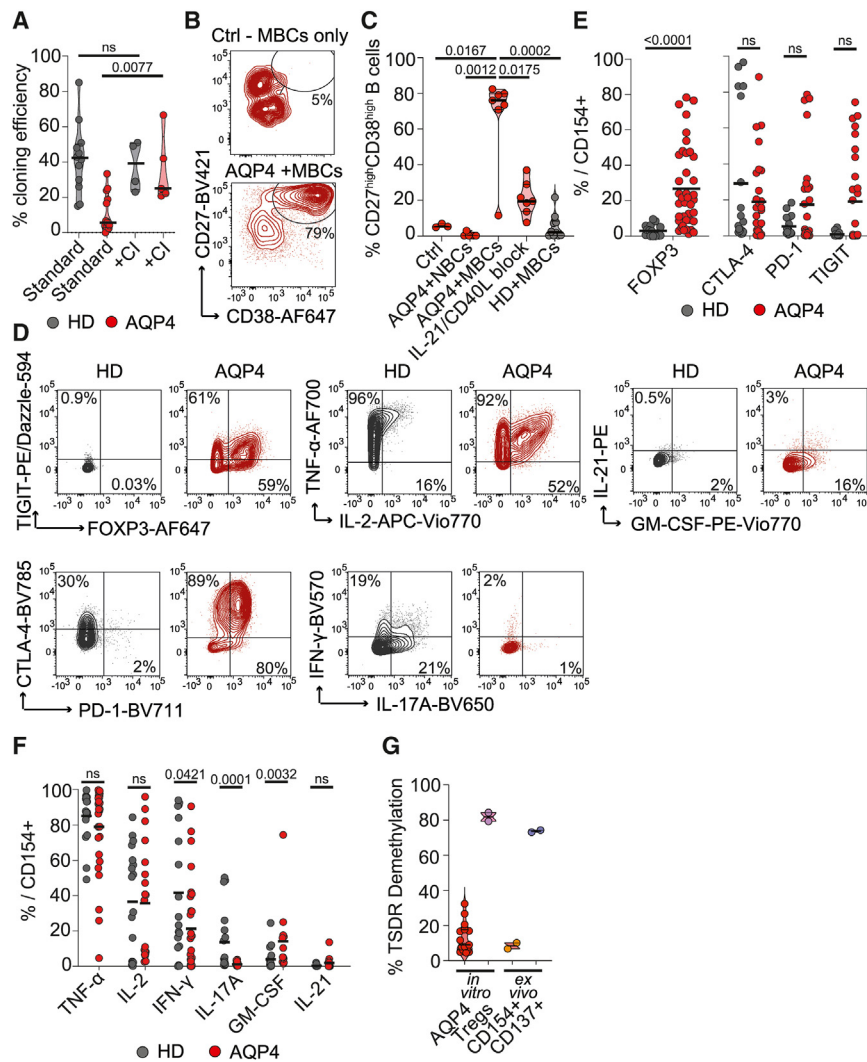


**Figure 4. *In vitro* AQP4-reactive CD4<sup>+</sup> T cell single-cell cloning and B cell helper assay**

AQP4-reactive CD154<sup>+</sup> T cells were single-cell FACS sorted into 96-well plates, expanded with CD3/CD28 and autologous APC in the presence or absence of checkpoint blockade (CI).

(A) Cloning efficiency without (HD,  $n = 12$ ; AQP4,  $n = 14$ ) or with CI (HD,  $n = 4$ ; AQP4,  $n = 5$ ).

(B and C) HLA-matched naive B cells (NBCs,  $n = 6$ ) or memory B cells (MBCs) were co-cultured with or without (Ctrl,  $n = 3$ ) expanded AQP4-reactive T cell clones (HD,  $n = 10$ ; AQP4,  $n = 7$ ) in the presence of the AQP4 peptide pool for 5 days. Plasmablast formation was defined as CD27<sup>high</sup>CD38<sup>high</sup> induction. Blocking anti-CD40L and soluble IL-21 receptor were added as indicated ( $n = 7$ ).

(D–F) Contour plot examples and summary of AQP4-reactive T cell clones from healthy donors (HDs) and AQP4-NMOSD patients (AQP4) after antigen restimulation stained for (E) co-inhibitory receptors (HD,  $n = 18$ ; AQP4,  $n = 29$ –39) and (F) cytokines (HD,  $n = 9$ –18; AQP4,  $n = 13$ –29).

(G) TSDR methylation of expanded AQP4-reactive T cell clones from AQP4-NMOSD patients (AQP4,  $n = 15$ ), expanded Treg lines ( $n = 2$ ), and *ex vivo* PMA- and ionomycin-activated CD154<sup>+</sup> and CD137<sup>+</sup> T cells from AQP4-NMOSD patients ( $n = 2$ ). Each symbol in (A) and (G) represents one donor. Each symbol in (C), (E), (F), and (G) represents one T cell clone. Horizontal lines indicate mean. Truncated violin plots with quartiles and range are shown in (A) and (G). Statistical differences: two-tailed Mann-Whitney test in (A), (C), (E), and (F). ns = not significant; significance was set at  $p < 0.05$ .

(D–F) Contour plot examples and summary of AQP4-reactive T cell clones from healthy donors (HDs) and AQP4-NMOSD patients (AQP4) after antigen restimulation stained for (E) co-inhibitory receptors (HD,  $n = 18$ ; AQP4,  $n = 29$ –39) and (F) cytokines (HD,  $n = 9$ –18; AQP4,  $n = 13$ –29).

(G) TSDR methylation of expanded AQP4-reactive T cell clones from AQP4-NMOSD patients (AQP4,  $n = 15$ ), expanded Treg lines ( $n = 2$ ), and *ex vivo* PMA- and ionomycin-activated CD154<sup>+</sup> and CD137<sup>+</sup> T cells from AQP4-NMOSD patients ( $n = 2$ ). Each symbol in (A) and (G) represents one donor. Each symbol in (C), (E), (F), and (G) represents one T cell clone. Horizontal lines indicate mean. Truncated violin plots with quartiles and range are shown in (A) and (G). Statistical differences: two-tailed Mann-Whitney test in (A), (C), (E), and (F). ns = not significant; significance was set at  $p < 0.05$ .

less chronic and often monophasic—glial autoantibody-specific demyelinating AID (MOGAD) showed less prominent presence of ThEx cells in their blood (Figures 5A–5F, S6A, and S6B). The clinical information on the cohort is provided in Table S2. Indeed, MOG-reactive T cells were neither increased in MOGAD patients as reported before<sup>28</sup> nor displayed TEM enrichment or any increased expression of CIRs or reduced cytokine expression as compared with memory T cells from HDs (Figures 5A–5D, S6A, and S6B). Instead, they contained a large fraction of naive T cells suggesting limited contact to MOG *in vivo*. In line with this, CI had no effect on cloning efficiency of MOG-reactive memory T cells (Figure 5E) and patient-derived MOG-specific T cell clones displayed low functional avidity to antigen (Figure 5F). Altogether, blood-derived MOG-specific T cells are minimally affected by MOG antigen *in vivo*, suggesting fundamentally different T cell responses in MOGAD versus AQP4-NMOSD.

If the presence of ThEx cells is associated with chronicity, we next sought to determine whether the ThEx phenotype is a common phenotype in highly chronic AIDs affecting other organs. We further analyzed patients with AIH and BP (clinical information provided in Tables S3 and S4), characterized by spe-

cific autoantibodies against SLA and BP180, respectively. SLA-specific Th cells were increased in autoantibody-positive AIH patients. While frequency of BP180-specific Th cells was not significantly increased in BP patients (Figures S6C and S6D), a strong expression of cutaneous lymphocyte-associated antigen (CLA) suggested skin-associated priming selectively in BP patients (Figure S6G). Similar to AQP4-NMOSD, effector memory auto-Th cells expressing more than one CIR were significantly increased in AIH and BP patients. This subset also showed maximal expression of FOXP3, albeit with higher variability, as compared with NMOSD (Figures 5G–5J). Furthermore, auto-Th cells expressed less cytokines in both AIDs than in healthy controls (Figures S6F and S6H).

In summary, ThEx cell formation appears to be common in chronic human AIDs targeting distinct antigens and organs, including AQP4-NMOSD, AIH, and BP. However, some AID—specifically MOGAD—appear to be T cell immunological different.

#### TCRs identified via scRNA-seq recognize AQP4 peptides

We also wanted to confirm the antigen-specificity of the TCRs identified by *ex vivo* scRNA-seq and to define their peptide/HLA targets, using NMOSD as a model. Within the 96 cells analyzed per sample, T-AQP4 exhibited significant clonal expansions (Figure 6A). Of the 234 AQP4-T cell TCRs analyzed, 54.3% were

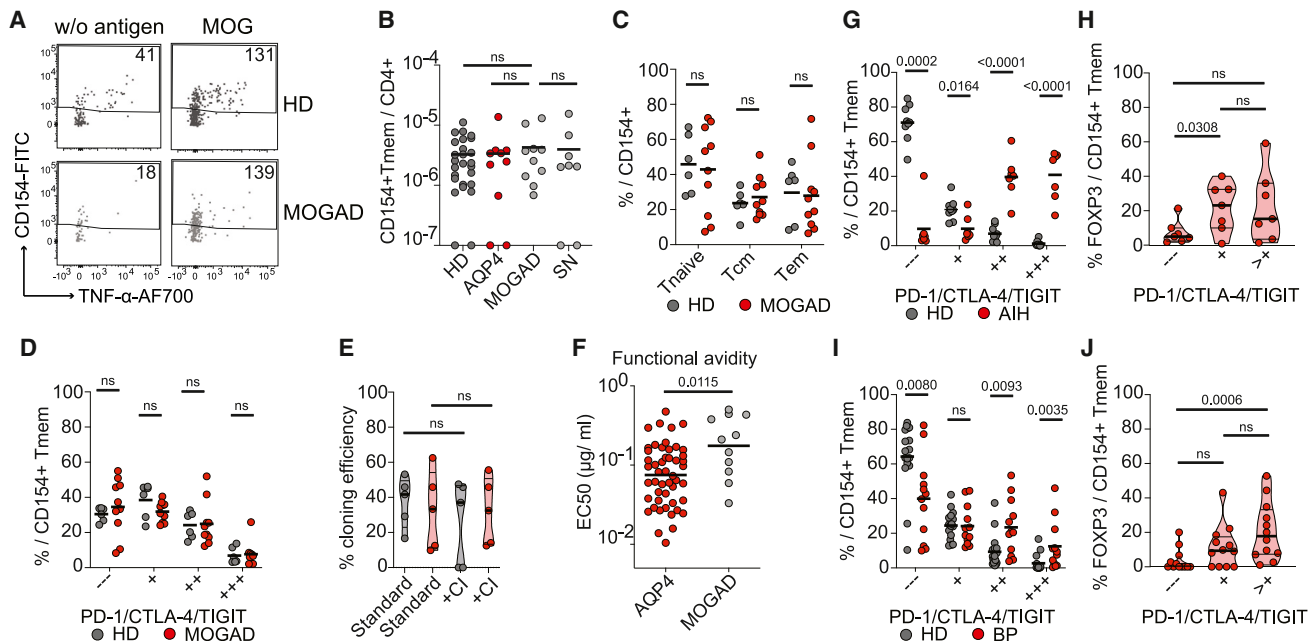


**Figure 5. Auto-ThEx cells are present in various AIDs**

(A) Dot plot examples for the *ex vivo* detection of MOG-reactive CD4<sup>+</sup> T cells by ARTE from  $3 \times 10^7$  PBMCs, cell counts are indicated.  
 (B) Frequencies of MOG-reactive CD154<sup>+</sup>CD45RA<sup>-</sup> memory CD4<sup>+</sup> T cells (Tmem), (HD,  $n = 26$  and patients,  $n = 28$ ) (AQP4,  $n = 10$ ; MOG antibody-associated disease [MOGAD],  $n = 10$ ; seronegative [SN],  $n = 8$ ).  
 (C) Proportion of naive, central memory, and effector memory T cells within MOG-reactive CD154<sup>+</sup> T cells (HD,  $n = 6$ ; MOGAD,  $n = 10$ ).  
 (D) *Ex vivo* proportion of MOG-reactive CD154<sup>+</sup> Tmem co-expressing the indicated number of co-inhibitory receptors (HD,  $n = 6$ ; MOGAD,  $n = 10$ ).  
 (E) Cloning efficiency of MOG-reactive CD154<sup>+</sup> T cells from healthy donors and MOGAD patients without (HD,  $n = 5$ ; MOGAD,  $n = 5$ ) or with (HD,  $n = 5$ ; MOGAD,  $n = 5$ ) checkpoint inhibitors.  
 (F) EC<sub>50</sub> values were determined from dose-response curves after antigen restimulation (AQP4,  $n = 49$  and MOGAD patients [MOGAD],  $n = 11$ ).  
 (G) *Ex vivo* proportion of SLA-reactive CD154<sup>+</sup> Tmem cells co-expressing the indicated number of co-inhibitory receptors from healthy donors (HDs,  $n = 9$ ) and AIH patients (AIH,  $n = 7$ ).  
 (H) Proportion of FOXP3<sup>+</sup> SLA-reactive CD154<sup>+</sup> Tmem from AIH patients expressing none, single, or >1 co-inhibitory receptor ( $n = 7$ ).  
 (I) *Ex vivo* proportion of cells co-expressing the indicated number of co-inhibitory receptors within BP180-reactive CD154<sup>+</sup> Tmem (HD,  $n = 17$ ; BP,  $n = 12$ ).  
 (J) Proportion of FOXP3<sup>+</sup> BP180-reactive CD154<sup>+</sup> Tmem from BP patients expressing none, single, or >1 co-inhibitory receptor.  
 Each symbol in (B)–(D) and (G)–(J) represents one donor, each symbol in (E) and (F) represents one T cell clone, and horizontal lines indicate mean in (B)–(D), (G), and (I). Truncated violin plots with quartiles and range are shown in (E), (H), and (J). Statistical differences: two-tailed Mann-Whitney test or unpaired t test in (B)–(J). Decision was based on an upstream normal distribution test. ns = not significant; significance was set at  $p < 0.05$ .

detected more than once (clone size 2.4%–9.9%). Overall, these expanded clones accounted for 41%–72% of the total sequenced AQP4-specific TCR repertoire from the three AQP4-NMOSD patients analyzed, suggesting an oligoclonal T cell response, which was similar to T-CAND cells (58%–67% of total TCR repertoire) and T-FLU cells (30% of total TCR repertoire) (Figure 6A). To confirm their epitope specificity, TCRs were re-expressed via orthotopic TCR replacement using CRISPR-Cas9 knockin into the TCR alpha constant (*TRAC*) locus of primary human CD4<sup>+</sup> T cells. Simultaneously, the TCR beta constant (*TRBC*) locus was knocked out to ensure correct TCR- $\alpha/\beta$  pairing<sup>55,56</sup> (Figures S7A and S7B). A total of 20 TCRs were re-expressed (Figure S7C), derived from expanded clonotypes from three AQP4-NMOSD patients, representing 28%–60% of the sequenced AQP4-specific TCR repertoire of each patient. Of these re-expressed TCRs, 85% (17 of 20) reacted against the AQP4 peptide pool, confirming their specific *ex vivo* detection (Figures 6B and 6C).

Next, we performed epitope mapping of the re-expressed AQP4 TCRs via single-peptide stimulation. Each TCR repertoire

derived from one individual patient recognized one major epitope (>60% of tested clones). However, the epitopes did not overlap between the patients. In one patient, six out of seven re-expressed TCRs (representing about 44% of the AQP4-specific TCR repertoire) recognized one single peptide (p26, amino acid [aa] 101–115) and one TCR recognized another peptide (p32, aa 125–139) (Figure S7D). All seven TCRs were restricted to HLA-DQ6.2 (DQA1\*01:02, DQB1\*06:02) as shown by use of specific HLA-DR, -DP, -DQ blocking antibodies (Figure S7E), HLA typing of the patients (Table S5) and restimulation of AQP4-specific T cell clones with a mono-allelic HLA-DQ6.2-expressing cell line (Figure S7F). Interestingly, HLA-DQ6 was over-represented within our small NMOSD cohort (9 out of 22 typed samples [41%] versus 15%–20% in Europe<sup>57,58</sup>, Table S5). T cells from three HLA-DQ6.2<sup>+</sup> patients also strongly reacted against a pool of selected immunodominant peptides (p25–27, aa 97–119 and p30–32, aa 117–139) in the ARTE assay (Figures S7G and S7H). Overall, this suggested that peptide AQP4<sub>101–115</sub> may represent a major T cell epitope in HLA-DQ6.2<sup>+</sup> NMOSD patients.

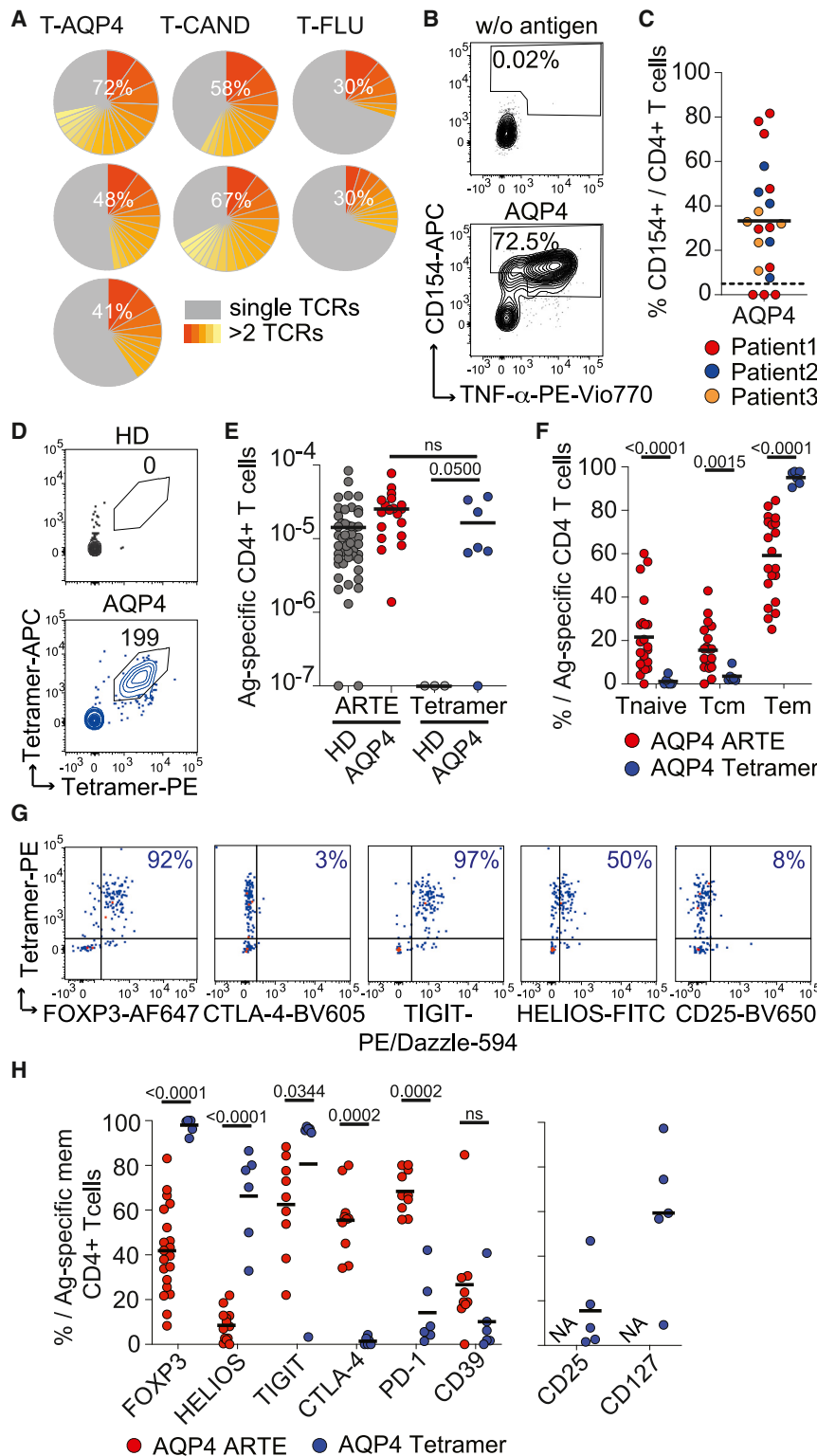


**Figure 6. TCR re-expression and peptide/HLA tetramer staining of AQP4-specific T cells**

(A) Pie charts of T cell receptor (TCR) repertoire of antigen-reactive T cells from NMO/D patients (AQP4, T-AQP4,  $n = 3$ ; *C. albicans*, T-CAND,  $n = 2$ ; and influenza, T-FLU,  $n = 2$ ). Percentage of clonally expanded TCRs ( $>1$ ) are indicated. (B and C) TCRs were re-expressed via orthotopic TCR replacement. (B) Contour plot example with and without restimulation. (C) Proportion of reactive TCRs (signal-to-noise ratio [SNR]  $>3\%$  and  $>5\%$  reactivity). (D–H) Peptide26/HLA-DQ6.2 tetramer (PE + APC) staining of PBMCs from HLA-DQ6.2<sup>+</sup> healthy donors (HDs,  $n = 3$ ) and AQP4-NMO/D patients (AQP4,  $n = 7$ ). (D) Contour plot examples after magnetic enrichment from  $3 \times 10^7$  PBMCs (cell counts indicated). (E–H) Comparison of antigen-specific CD4<sup>+</sup> T cells detected by ARTE or by tetramer enrichment. (E) Frequencies in healthy donors (HD ARTE,  $n = 48$ ; HD tetramer,  $n = 3$ ) and AQP4-NMO/D patients (AQP4 ARTE,  $n = 19$ ; AQP4 tetramer,  $n = 7$ ) and (F) phenotype (AQP4 ARTE,  $n = 22$ ; AQP4 tetramer,  $n = 6$ ). (G) Phenotype of tetramer-positive CD4<sup>+</sup> T cells (dot plot examples). (H) ARTE versus tetramer enrichment: comparison of indicated marker expression (AQP4 ARTE,  $n = 9–20$ ; AQP4 tetramer,  $n = 5–6$ ). For CD25 and CD127, no ARTE data are available (NA). Each symbol in (E), (F), and (H) represents one donor. Each symbol in (C) represents one transgenic TCR. Horizontal lines indicate mean. Statistical differences: two-tailed Mann-Whitney test in (E), (F), and (H). ns = not significant; significance was set at  $p < 0.05$ .

(Figure S7I) and analyzed HLA-DQ6.2<sup>+</sup> NMO/D patients ( $n = 7$ ) and HDs ( $n = 3$ ), using combined tetramer staining and magnetic enrichment. As shown in Figures 6D and 6E, tetramer-positive T cells were exclusively detected in PBMCs from patients (6 out of 7) but not in HLA-DQ6<sup>+</sup> HDs. Their frequency ranged from  $10^{-6}$  to  $10^{-4}$ , similar to the frequencies detected via the ARTE assay. AQP4-specific tetramer-positive CD4<sup>+</sup> T cells were almost exclusively effector memory cells (Figures 6F and S7J) and displayed a high expression of FOXP3, HELIOS, and TIGIT (Figures 6G and 6H). Tetramer-positive CD4<sup>+</sup> T cells did not express CD25 but instead expressed low levels of CD127 (Figures 6G and 6H), further

**Peptide-HLA-DQ6 tetramer staining confirms the *ex vivo* FOXP3<sup>+</sup> ThEx phenotype**

To test the relevance of peptide AQP4<sub>101–115</sub> restricted by HLA-DQ6.2 and to independently confirm the T-AQP4 phenotype, we generated AQP4<sub>101–115</sub>/HLA-DQ6.2 tetramers

supporting their effector T cell origin. Tetramer-positive CD4<sup>+</sup> T cells also lacked Ki67, CD38, and ICOS (Figures S7K and S7L). Interestingly, the expression of exhaustion markers such as PD-1, CTLA-4, and CD39 was reduced on cells identified by the tetramer, compared with

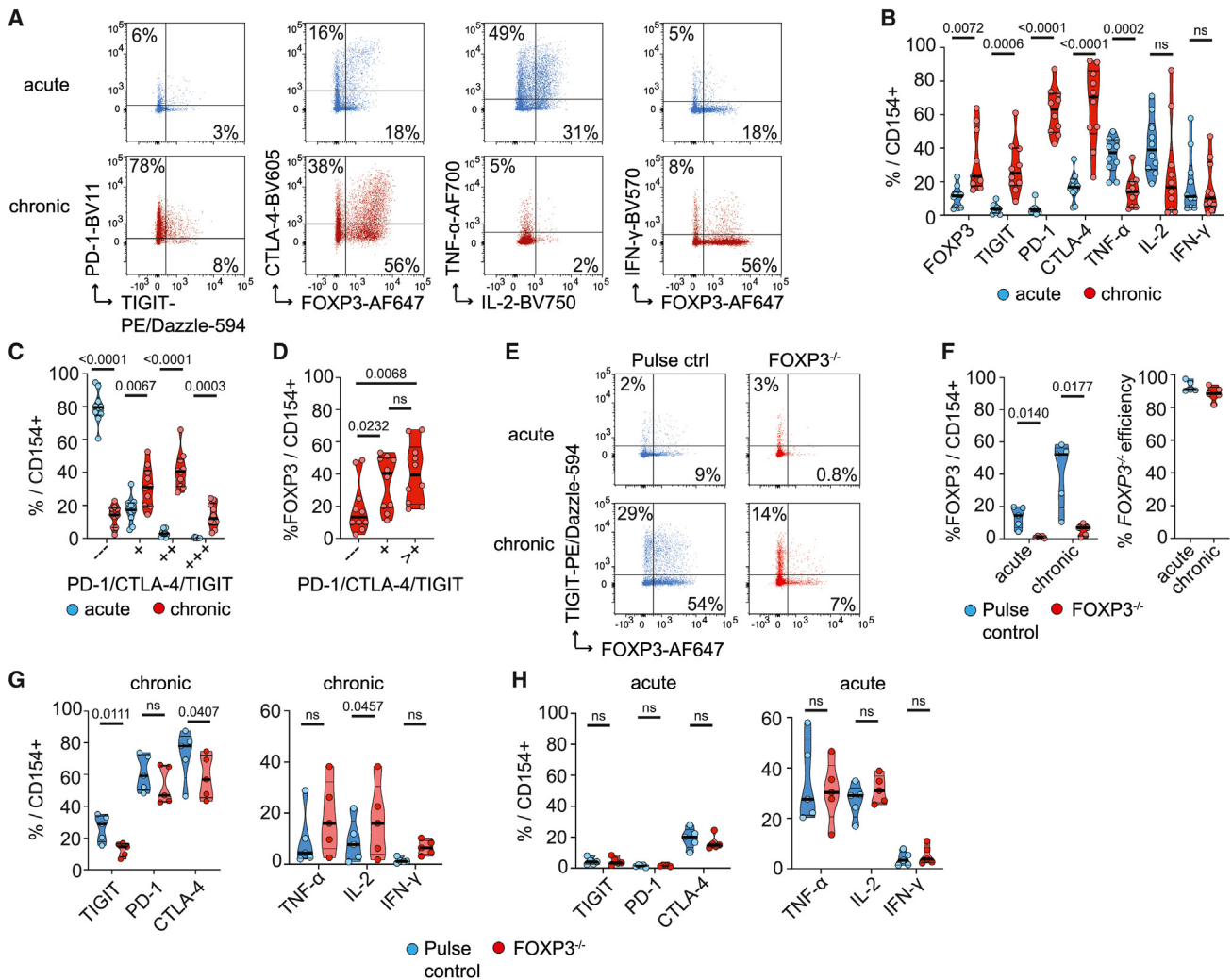


**Figure 7. FOXP3 regulates the ThEx phenotype induced by chronic stimulation *in vitro***

Naive CD4<sup>+</sup> T cells plus autologous APCs were stimulated with staphylococcal enterotoxin b (SEB) once (acute) or daily (chronic) for 7 days.

(A) Dot plot examples of CD4<sup>+</sup> T cells.

(B) Proportion of FOXP3, co-inhibitory receptor, and cytokine expressing cells ( $n = 10$ ).

(C) Proportion of cells expressing the indicated number of co-inhibitory receptors ( $n = 10$ ).

(D) Proportion of chronically stimulated FOXP3<sup>+</sup> CD154<sup>+</sup> T cells expressing none, single, or >1 co-inhibitory receptor ( $n = 10$ ).

(E–H) Before the start of chronic stimulation, FOXP3 was deleted using CRISPR-Cas9. (E) Dot plot examples comparing the pulse control and the FOXP3<sup>-/-</sup>.

(F) Proportion of cells expressing FOXP3 within once (acute) or chronically stimulated cells with or without FOXP3 deletion ( $n = 5$ ) and efficiency of FOXP3 deletion.

(G and H) Proportion of cells expressing co-inhibitory receptors and cytokines within CD154<sup>+</sup> T cells with or without FOXP3 deletion after (G) chronic stimulation ( $n = 5$ ) and (H) acute stimulation ( $n = 5$ ).

Each symbol in (B)–(D) and (F)–(H) represents one donor. Truncated violin plots with quartiles and range are shown in (B)–(D) and (F)–(H). Statistical differences: two-tailed Mann-Whitney test or unpaired t test in (B)–(D) and (F). Wilcoxon matched-pairs signed rank test or two-tailed paired t test in (G) and (H). Decision was based on an upstream normal distribution test. ns = not significant; significance was set at  $p < 0.05$ .

AQP4-reactive T cells detected via ARTE (Figure 6H). This suggests that ThEx cells are poised *in vivo* to rapidly up-regulate these markers during the 7-h activation period performed prior to the ARTE assay. In summary, these analyses confirmed that AQP4-reactive effector/memory CD4<sup>+</sup> T cells have reached an ThEx stage in AQP4-NMOSD patients, marked by the constitutive expression of FOXP3, HELIOS, and TIGIT, as well as by the rapid (<7 h) upregulation of CTLA-4 and PD-1 upon antigen stimulation.

### FOXP3 regulates the ThEx phenotype induced by chronic *in vitro* stimulation

To test the possibility that chronic stimulation is indeed driving the ThEx phenotype, we developed an *in vitro* protocol with daily polyclonal stimulation of purified CD4 T cells *in vitro* and compared it with single stimulation (Figure 7). After a 7-day chronic stimulation—but not after a single stimulation—a ThEx phenotype was induced, including strong upregulation of FOXP3, TIGIT, PD-1, and CTLA-4 as well as decreased

expression of cytokines such as IL-2 and TNF- $\alpha$ , while IFN- $\gamma$  was not affected (Figures 7A and 7B). Similar to the *ex vivo* ThEx phenotype, cells co-expressing multiple CIRs were increased and also expressed FOXP3 (Figures 7C and 7D). Next, we performed a *FOXP3*<sup>-/-</sup> using CRISPR-Cas9 before the start of chronic stimulation (Figures 7E–7H). The *FOXP3*<sup>-/-</sup> reduced FOXP3 expression by 80%–90% (Figures 7E and 7F). At the same time, expression of TIGIT and CTLA-4 was significantly reduced, and the expression of IL-2, TNF- $\alpha$ , and IFN- $\gamma$  increased. In contrast, *FOXP3*<sup>-/-</sup> prior to a single stimulation had no significant effect on CIR and cytokine expression (Figures 7G and 7H). These data demonstrate that chronic stimulation can be sufficient to drive key aspects of the ThEx phenotype and further suggest that FOXP3 is functionally involved in this process and inversely regulates expression of signature CIRs and inflammatory cytokines.

## DISCUSSION

We identified auto-Th cells in AQP4-NMOSD patients characterized by a ThEx phenotype and expression of the canonical Treg master transcription factor FOXP3. The same ThEx phenotype was prominent in auto-Th cells of two additional chronic organ-specific AIDs of the liver and the skin, suggesting a common exhaustion-like pathway in chronic antigen-specific autoimmunity. Interestingly, MOG-specific T cells were minimally affected by antigen in patients with the more often monophasic and less chronic/relapse-prone MOGAD. This could indicate either T cell ignorance due to the sequestration of MOG in the central nervous system (in contrast to systemically present autoantigens in the other AIDs) or a tissue-restricted T cell response. These different response patterns, how they correlate with chronicity, and how they classify other AIDs need to be investigated in future experiments. Indeed, auto-ThEx cells maintained the capacity to express CD154, persisted during immunotherapy-induced AID remission, and could be reactivated *in vitro*. All these identify auto-ThEx cells as therapy-resistant, reactivatable, and potentially pathogenic T cell memory, which may thus contribute to disease chronicity and propensity to relapse. Moreover, we provide proof of concept for the role of exhaustion-like programming among autoantigen-specific CD4<sup>+</sup> T cells in prototypic antigen-specific AIDs, suggesting that T cells rely on similar mechanisms to adapt to chronic antigen stimulation in AIDs, cancer, and chronic infections. This reveals novel cellular targets and pathways for therapeutic intervention and disease monitoring.

A dominant role for exhausted autoantigen-specific T cells in AID patients is at odds with the current view of pro-inflammatory activated T cells driving chronic autoimmunity.<sup>37</sup> Previous studies in AIDs, including NMOSD, mainly identify T cells with pro-inflammatory or B cell helper function.<sup>16,24–31</sup> However, the current standard readouts for auto-Th cell identification (proliferation, pro-inflammatory cytokines) may selectively miss exhausted, non-proliferative ThEx cells, as identified herein. In fact, T cell exhaustion in AIDs may even be expected given the chronic presence of (auto)antigens, similar to tumors or chronic infections. Consistently, a CD8<sup>+</sup> T cell transcriptional profile of exhaustion correlates with beneficial outcome in AID<sup>35,59</sup> and response to immunotherapies.<sup>60</sup> Inhibitory receptor deficiencies or checkpoint therapies

can cause or exacerbate AIDs,<sup>37,61</sup> and exhausted CD8 and CD4 T cells are present in inflamed tissues of T1D<sup>36,62</sup> and systemic lupus erythematosus (SLE)<sup>63</sup> models. Here, we demonstrated exhaustion on the level of autoantigen-specific T cells in AID patients. ThEx cells were independent of the type of immunotherapy, disease duration, or severity, suggesting that these pathogenic memory cells persist long term and escape immunosuppressive therapies used in our patient cohorts (Table S2). Although auto-Th frequencies did not significantly vary over time, a balance between exhaustion and pro-inflammatory Th cells would be in line with previous studies linking elevated cytokines to disease severity.<sup>25,27</sup> In AQP4-NMOSD, the proportion of FOXP3<sup>+</sup> auto-ThEx was slightly increased during therapy-induced remission, and ThEx was less pronounced in BP patients, who on average have a shorter time from onset of disease to blood sampling (Table S4). However, this needs to be confirmed in larger patient cohorts with different AID types and time points. In any case, the long-term persistence of (re-)activatable autoantigen-specific ThEx cells in patients in remission may well explain the less-than-perfect treatment efficacy of steroid-sparing agents,<sup>64–67</sup> depletion of CD19/CD20 memory B cells,<sup>68,69</sup> as well as exacerbation of disease by  $\beta$ -IFN.<sup>27,70</sup> Expanded populations of auto-Th cells as well as the ThEx cell phenotype were virtually absent in HDs, further suggesting that exhaustion actively modulates the pathogenic T cell response in patients rather than restricts autoreactivity development in HDs.<sup>61</sup>

An intriguing molecular change that we observed was the induction of FOXP3 in exhausted autoreactive T-AQP4 cells. ThEx cells resembled conventional T cells rather than Tregs, based on TCR clonal heterogeneity, phenotypic and transcriptional profiling, *FOXP3* TSDR methylation, and reactivation potential. FOXP3<sup>+</sup> AQP4-specific ThEx cells were absent in HDs, indicating that they are not derived from an unstable thymic Treg precursor, as described in various AIDs<sup>71,72</sup> including NMOSD.<sup>73–76</sup> FOXP3 expression in conventional human CD4<sup>+</sup> T cells negatively regulates cytokine production and proliferation<sup>77</sup> and prevents apoptosis upon repetitive TCR stimulation,<sup>78</sup> which may improve ThEx cell survival. Of interest, recent data identify FOXP3<sup>+</sup> acquisition by conventional naive T cell-derived Tfh cells in late murine<sup>79</sup> as well as in human germinal centers.<sup>80</sup> These cells acquire suppressive function but maintained B helper cell function.<sup>80</sup> Similarly, gluten-tetramer-positive T cells in celiac disease patients display an “unconventional” FOXP3<sup>+</sup> CD25<sup>-</sup> phenotype, despite otherwise exhibiting a Tph phenotype, including expression of IL-21 and inhibitory receptors but absence of CXCR5. A similar Tph phenotype is present in rheumatoid arthritis<sup>54</sup> and in autoantigen-specific T cells isolated via ARTE from patients with AIH. These cells express IL-21 and IFN- $\gamma$  but not *FOXP3*.<sup>16</sup> These phenotypes at least partially overlap with the ThEx signature described here, with the exception of reduced cytokine expression in the FOXP3<sup>+</sup> subset. Considering the importance of AQP4-specific antibodies in NMOSD and in view of the common clonal origin of FOXP3<sup>+</sup> and FOXP3<sup>-</sup> ThEx cells, we speculate that ThEx cells are indeed related to Tfh/Tph cells induced by chronic antigen-stimulation. However, an alternative Treg origin cannot be excluded, which remains to be analyzed in the future.

In conclusion, our findings suggest a central role of auto-Th cell exhaustion in chronicity and propensity to relapse in chronic

AIDs and a novel role of the canonical transcription factor FOXP3 in CD4 T cell exhaustion. The specific elimination of ThEx cells or profound suppression of their reactivation represents a novel and previously underappreciated target for therapeutic intervention in AID.

### Limitations of the study

The study cohort is small, limiting the validity of HLA-DQ6 associations or correlations between T cell status and clinical status (remission versus active disease/relapse) or treatment status. The study is restricted to blood, and the presence and phenotypes of autoreactive T cells in tissues or CSF needs to be clarified. We cannot exclude a role of Tregs, e.g., targeting different epitopes, since we focused on CD154<sup>+</sup> Tcon and AQP4<sub>101–115</sub>/HLA-DQ6. Future studies need to broadly analyze the peptide/HLA targets of Tcon and Treg in all AIDs analyzed here. Ultimately, several questions remain open: how is the exhausted phenotype induced *in vivo* and where and how is exhaustion reversed; and can the induction or stabilization of the exhausted state or the elimination of exhausted T cells be exploited therapeutically, such as via antigen-specific immune therapy?

### RESOURCE AVAILABILITY

#### Lead contact

Further information and requests for resources and reagents should be directed to and will be fulfilled by the Lead Contact, Alexander Scheffold ([Alexander.Scheffold@uksh.de](mailto:Alexander.Scheffold@uksh.de)).

#### Materials availability

This study did not generate new unique reagents.

#### Data and code availability

The raw paired-end scRNAseq fastq files, as well as processed gene expression and clonotype tables, respectively, are deposited at GEO (accession number is GSE242232) and are publicly available as of the date of publication. Flow cytometry and genotyping data (Infinium Global Screening Array-24 (GSA)) will be available from the [lead contact](#) upon request.

### ACKNOWLEDGMENTS

This research was supported by the German Federal Ministry of Education and Science (BMBF) and the European Joint Program for Rare Diseases (EJPRD) grant AspecT-NMO (01GM1923A) (to A.S., S.F., R.M., and M.W.); BMBF projects 01K12013 and 01EO2106 (to E.S., K.S., and J.H.); CONNECT-GENERATE 01GM1908A and 01GM22088 (to F.L.); the Deutsche Forschungsgemeinschaft (DFG) under Germany's Excellence Strategy—EXC 2167-390884018 (to A.S., P.B., and A.F.); DFG grant SCHE 670 3-1 project no. 433038070, TRR241 project ID 375876048, and TRR355 project no. 490846870 (to A.S. and P.B.); CRC1526 (SFB1526/01, project no. 454193335) (to A.S., E.S., M.H., and M.B.); HU 1294/8-1 (to A.H.); HA 8440/3-1 (to J.H.); SFB1309 (DFG program CRC1309, ID: 325871075) (to J.W.); the European Union via E-Rare Joint Transnational research support (ERA-Net, UltraAIE, LE3064/2-1 to F.L.); HORIZON MSCA 2022 Doctoral Network 101119457—IgG4-TREAT (to F.L.); the ERC starting grant EpiTune (803992) (to J.K.P.); the Clinical Research Priority Program MS (CRPPMS) of the University of Zurich (UZH) and the Suisse SNF grant 32ER30\_187509 (to R.M.); and the Stiftung Pathobiochemie of the German Society for Laboratory Medicine (to F.L.). We thank Anne Schulze for expert technical assistance. We thank Beate Schmitt and Christina LoPorto for sequencing assistance, Abdulrahman Salhab for bioinformatic assistance, and Lucia Bernhardt for establishment of the hairpin construct. We thank Johannes Herkel for his valuable scientific advice. The graphical abstract was created with [BioRender.com](#).

### AUTHOR CONTRIBUTIONS

C.S., P.B., F.P., F.L., and A.S. contributed equally to this work. C.S. and P.B. designed and performed experiments, analyzed the data, generated the figures, and wrote the manuscript. K.-P.W., J.D., K.H.S., I.S., R.M., M.H., A.D., J.H., E.S., G.H., C.B., M.B., V.H., and P.S. provided patient blood samples and collected clinical data. D.E., M.R., and A.P. performed biostatistical analyses of high-throughput microfluidic scRNA-seq data. A.H. and S.-S.S. performed the T cell/B cell cooperation assay. J.G., J.W., J.K.P., and M.Y. performed the bisulfite treatment and methylation analysis. M.W., L.H., and D.B. generated the HLA-DQ6:AQP-4 tetramers. R.N. and R.M. provided the BLS cell line and technical advice. K.S., D.H.B., and E.-M.S. assisted with the orthotopic TCR replacement. M.W. and A.F. performed the array-based genotyping and HLA imputation. A.D. and S.R. supervised the scRNA-seq (Smart-seq2). S.M., N.M., N.K., and G.R.M. performed flow cytometry and sequencing experiments. C.P. performed cell sorting. S.F., F.P., F.L., and A.S. designed the study, evaluated data, and wrote the manuscript. All authors contributed to writing of the manuscript.

### DECLARATION OF INTERESTS

R.N. is a current employee of Cellerys AG.

F.L. discloses speaker honoraria from Grifols, Teva, Biogen, Bayer, Roche, Novartis, and Fresenius; travel funding from Merck, Grifols, and Bayer; and is serving on advisory boards for Roche, Biogen, and Alexion.

R.M. has received unrestricted grants from Biogen, Novartis, Roche, and Third Rock and honoraria for advisory roles and lectures from Roche, Novartis, Biogen, Genzyme, Neuway, CellProtect, Third Rock, and Teva. He is a patent holder and co-holder on the following patents: daclizumab in MS (held by NIH), JCV VP1 for vaccination against PML; JCV-specific neutralizing antibodies to treat PML; and antigen-specific tolerization with peptide-coupled cells, novel autoantigens in MS, and designer neoantigens for tumor vaccination (all held by University of Zurich). He is a co-founder of Abata Therapeutics, Watertown, MA, USA and co-founder and employee of Cellerys AG, Schlieren, Switzerland.

### STAR★METHODS

Detailed methods are provided in the online version of this paper and include the following:

- [KEY RESOURCES TABLE](#)
- [EXPERIMENTAL MODEL AND STUDY PARTICIPANT DETAILS](#)
- [METHOD DETAILS](#)
  - Cell lines
  - Antigenes
  - Antigen-reactive T cell enrichment
  - Flow cytometry
  - Expansion and re-stimulation of antigen-reactive T cells
  - Analysis of functional avidity
  - Peptide Screening
  - HDR Template Design
  - Orthotopic T cell receptor replacement in primary human CD4<sup>+</sup> T cells
  - HLA class II tetramer enrichment
  - T cell/B cell cooperation assay
  - Chronic stimulation assay
  - FOXP3<sup>-/-</sup> via CRISPR/Cas9
  - Bisulfite Treatment and Methylation Analysis
  - Array-based genotyping and HLA imputation
  - Single-cell RNA-seq assay (Smart-seq2)
  - Single-cell transcriptome and TCR repertoire data analysis
- [QUANTIFICATION AND STATISTICAL ANALYSIS](#)

### SUPPLEMENTAL INFORMATION

Supplemental information can be found online at <https://doi.org/10.1016/j.immuni.2024.08.005>.

Received: January 26, 2024  
Revised: May 14, 2024  
Accepted: August 7, 2024  
Published: September 2, 2024

REFERENCES

- Attfeld, K.E., Jensen, L.T., Kaufmann, M., Friese, M.A., and Fugger, L. (2022). The immunology of multiple sclerosis. *Nat. Rev. Immunol.* 22, 734–750. <https://doi.org/10.1038/s41577-022-00718-z>.
- Maschmeyer, P., Chang, H.D., Cheng, Q., Mashreghi, M.F., Hiepe, F., Alexander, T., and Radbruch, A. (2021). Immunological memory in rheumatic inflammation - a roadblock to tolerance induction. *Nat. Rev. Rheumatol.* 17, 291–305. <https://doi.org/10.1038/s41584-021-00601-6>.
- Mitsdoerffer, M., Kuchroo, V., and Korn, T. (2013). Immunology of neuro-myelitis optica: a T cell-B cell collaboration. *Ann. N. Y. Acad. Sci.* 1283, 57–66. <https://doi.org/10.1111/nyas.12118>.
- Bacher, P., and Scheffold, A. (2013). Flow-cytometric analysis of rare antigen-specific T cells. *Cytometry A* 83, 692–701. <https://doi.org/10.1002/cyto.a.22317>.
- Künzli, M., and Masopust, D. (2023). CD4<sup>+</sup> T cell memory. *Nat. Immunol.* 24, 903–914. <https://doi.org/10.1038/s41590-023-01510-4>.
- Yang, J.H.M., Ward-Hartstonge, K.A., Perry, D.J., Blanchfield, J.L., Posgai, A.L., Wiedeman, A.E., Diggins, K., Rahman, A., Tree, T.I.M., Brusko, T.M., et al. (2022). Guidelines for standardizing T-cell cytometry assays to link biomarkers, mechanisms, and disease outcomes in type 1 diabetes. *Eur. J. Immunol.* 52, 372–388. <https://doi.org/10.1002/eji.202049067>.
- Cossarizza, A., Chang, H.D., Radbruch, A., Abrignani, S., Addo, R., Akdis, M., Andra, I., Andreato, F., Annunziato, F., Arranz, E., et al. (2021). Guidelines for the use of flow cytometry and cell sorting in immunological studies (third edition). *Eur J Immunol* 51, 2708–3145. <https://doi.org/10.1002/eji.202170126>.
- Theofilopoulos, A.N., Kono, D.H., and Baccala, R. (2017). The multiple pathways to autoimmunity. *Nat. Immunol.* 18, 716–724. <https://doi.org/10.1038/ni.3731>.
- Liblau, R.S., Latorre, D., Kornum, B.R., Dauvilliers, Y., and Mignot, E.J. (2024). The immunopathogenesis of narcolepsy type 1. *Nat. Rev. Immunol.* 24, 33–48. <https://doi.org/10.1038/s41577-023-00902-9>.
- Su, L.F., Kidd, B.A., Han, A., Kotzin, J.J., and Davis, M.M. (2013). Virus-specific CD4(+) memory-phenotype T cells are abundant in unexposed adults. *Immunity* 38, 373–383. <https://doi.org/10.1016/j.immuni.2012.10.021>.
- Su, L.F., Del Alcazar, D., Stelekati, E., Wherry, E.J., and Davis, M.M. (2016). Antigen exposure shapes the ratio between antigen-specific Tregs and conventional T cells in human peripheral blood. *Proc. Natl. Acad. Sci. USA* 113, E6192–E6198. <https://doi.org/10.1073/pnas.1611723113>.
- Wen, X., Yang, J., James, E., Chow, I.T., Reijonen, H., and Kwok, W.W. (2020). Increased islet antigen-specific regulatory and effector CD4<sup>+</sup> T cells in healthy individuals with the type 1 diabetes-protective haplotype. *Sci. Immunol.* 5, eaax8767. <https://doi.org/10.1126/sciimmunol.aax8767>.
- Jiang, W., Birtley, J.R., Hung, S.C., Wang, W., Chiou, S.H., Macaubas, C., Kornum, B., Tian, L., Huang, H., Adler, L., et al. (2019). In vivo clonal expansion and phenotypes of hypocretin-specific CD4<sup>+</sup> T cells in narcolepsy patients and controls. *Nat. Commun.* 10, 5247. <https://doi.org/10.1038/s41467-019-13234-x>.
- Ooi, J.D., Petersen, J., Tan, Y.H., Huynh, M., Willett, Z.J., Ramarathinam, S.H., Eggenhuizen, P.J., Loh, K.L., Watson, K.A., Gan, P.Y., et al. (2017). Dominant protection from HLA-linked autoimmunity by antigen-specific regulatory T cells. *Nature* 545, 243–247. <https://doi.org/10.1038/nature22329>.
- Scally, S.W., Petersen, J., Law, S.C., Dudek, N.L., Nel, H.J., Loh, K.L., Wijeyewickrema, L.C., Eckle, S.B.G., van Heemst, J., Pike, R.N., et al. (2013). A molecular basis for the association of the HLA-DRB1 locus, citrullination, and rheumatoid arthritis. *J. Exp. Med.* 210, 2569–2582. <https://doi.org/10.1084/jem.20131241>.
- Renand, A., Cervera-Marzal, I., Gil, L., Dong, C., Garcia, A., Kervagoret, E., Aublé, H., Habes, S., Chevalier, C., Vavasseur, F., et al. (2020). Integrative molecular profiling of autoreactive CD4 T cells in autoimmune hepatitis. *J. Hepatol.* 73, 1379–1390. <https://doi.org/10.1016/j.jhep.2020.05.053>.
- Christophersen, A., Lund, E.G., Snir, O., Solà, E., Kanduri, C., Dahal-Koirala, S., Zühlke, S., Molberg, Ø., Utz, P.J., Rohani-Pichavant, M., et al. (2019). Distinct phenotype of CD4<sup>+</sup> T cells driving celiac disease identified in multiple autoimmune conditions. *Nat. Med.* 25, 734–737. <https://doi.org/10.1038/s41591-019-0403-9>.
- Pohl, M., Fischer, M.T., Mader, S., Schanda, K., Kitic, M., Sharma, R., Wimmer, I., Misu, T., Fujihara, K., Reindl, M., et al. (2011). Pathogenic T cell responses against aquaporin 4. *Acta Neuropathol.* 122, 21–34. <https://doi.org/10.1007/s00401-011-0824-0>.
- Jones, M.V., Huang, H., Calabresi, P.A., and Levy, M. (2015). Pathogenic aquaporin-4 reactive T cells are sufficient to induce mouse model of neuromyelitis optica. *Acta Neuropathol. Commun.* 3, 28. <https://doi.org/10.1186/s40478-015-0207-1>.
- Zeka, B., Hastermann, M., Kaufmann, N., Schanda, K., Pende, M., Misu, T., Rommer, P., Fujihara, K., Nakashima, I., Dahle, C., et al. (2016). Aquaporin 4-specific T cells and NMO-IgG cause primary retinal damage in experimental NMO/SD. *Acta Neuropathol. Commun.* 4, 82. <https://doi.org/10.1186/s40478-016-0355-y>.
- Vogel, A.L., Knier, B., Lammens, K., Kalluri, S.R., Kuhlmann, T., Bennett, J.L., and Korn, T. (2017). Deletional tolerance prevents AQP4-directed autoimmunity in mice. *Eur. J. Immunol.* 47, 458–469. <https://doi.org/10.1002/eji.201646855>.
- Yick, L.W., Ma, O.K.F., Chan, E.Y.Y., Yau, K.X., Kwan, J.S.C., and Chan, K.H. (2023). T follicular helper cells contribute to pathophysiology in a model of neuromyelitis optica spectrum disorders. *JCI Insight* 8, e161003. <https://doi.org/10.1172/jci.insight.161003>.
- Sagan, S.A., Moïnfar, Z., Moseley, C.E., Dandekar, R., Spencer, C.M., Verkman, A.S., Ottersen, O.P., Sobel, R.A., Sidney, J., Sette, A., et al. (2023). T cell deletional tolerance restricts AQP4 but not MOG CNS autoimmunity. *Proc. Natl. Acad. Sci. USA* 120, e2306572120. <https://doi.org/10.1073/pnas.2306572120>.
- Varrin-Doyer, M., Spencer, C.M., Schulze-Toppfhoff, U., Nelson, P.A., Stroud, R.M., Cree, B.A.C., and Zamvil, S.S. (2012). Aquaporin 4-specific T cells in neuromyelitis optica exhibit a Th17 bias and recognize Clostridium ABC transporter. *Ann. Neurol.* 72, 53–64. <https://doi.org/10.1002/ana.23651>.
- Linhares, U.C., Schiavoni, P.B., Barros, P.O., Kasahara, T.M., Teixeira, B., Ferreira, T.B., Alvarenga, R., Hygino, J., Vieira, M.M.M., Bittencourt, V.C.B., et al. (2013). The ex vivo production of IL-6 and IL-21 by CD4<sup>+</sup> T cells is directly associated with neurological disability in neuromyelitis optica patients. *J. Clin. Immunol.* 33, 179–189. <https://doi.org/10.1007/s10875-012-9780-2>.
- Vaknin-Dembinsky, A., Brill, L., Kassis, I., Petrou, P., Ovadia, H., Ben-Hur, T., Abramsky, O., and Karussis, D. (2016). T-cell responses to distinct AQP4 peptides in patients with neuromyelitis optica (NMO). *Mult. Scler. Relat. Disord.* 6, 28–36. <https://doi.org/10.1016/j.msard.2015.12.004>.
- Agasing, A.M., Wu, Q., Khatri, B., Borisow, N., Ruprecht, K., Brandt, A.U., Gawde, S., Kumar, G., Quinn, J.L., Ko, R.M., et al. (2020). Transcriptomics and proteomics reveal a cooperation between interferon and T-helper 17 cells in neuromyelitis optica. *Nat. Commun.* 11, 2856. <https://doi.org/10.1038/s41467-020-16625-7>.
- Hofer, L.S., Ramberger, M., Gredler, V., Pescoller, A.S., Rostásy, K., Sospedra, M., Hegen, H., Berger, T., Lutterotti, A., and Reindl, M. (2020). Comparative Analysis of T-Cell Responses to Aquaporin-4 and Myelin Oligodendrocyte Glycoprotein in Inflammatory Demyelinating Central Nervous System Diseases. *Front. Immunol.* 11, 1188. <https://doi.org/10.3389/fimmu.2020.01188>.

29. Muscate, F., Woestemeier, A., and Gagliani, N. (2021). Functional heterogeneity of CD4<sup>+</sup> T cells in liver inflammation. *Semin. Immunopathol.* **43**, 549–561. <https://doi.org/10.1007/s00281-021-00881-w>.
30. Lee, A.Y., Kim, T., and Kim, J.H. (2023). Understanding CD4<sup>+</sup> T cells in autoimmune bullous diseases. *Front. Immunol.* **14**, 1161927. <https://doi.org/10.3389/fimmu.2023.1161927>.
31. Cardon, A., Conchon, S., and Renand, A. (2021). Mechanisms of autoimmune hepatitis. *Curr. Opin. Gastroenterol.* **37**, 79–85. <https://doi.org/10.1097/MOG.0000000000000704>.
32. Wherry, E.J., and Kurachi, M. (2015). Molecular and cellular insights into T cell exhaustion. *Nat. Rev. Immunol.* **15**, 486–499. <https://doi.org/10.1038/nri3862>.
33. Collier, J.L., Weiss, S.A., Pauken, K.E., Sen, D.R., and Sharpe, A.H. (2021). Not-so-opposite ends of the spectrum: CD8<sup>+</sup> T cell dysfunction across chronic infection, cancer and autoimmunity. *Nat. Immunol.* **22**, 809–819. <https://doi.org/10.1038/s41590-021-00949-7>.
34. McKinney, E.F., and Smith, K.G. (2016). T-cell exhaustion: understanding the interface of chronic viral and autoinflammatory diseases. *Immunol. Cell Biol.* **94**, 935–942. <https://doi.org/10.1038/icb.2016.81>.
35. Wiedeman, A.E., Muir, V.S., Rosasco, M.G., DeBerg, H.A., Presnell, S., Haas, B., Dufort, M.J., Speake, C., Greenbaum, C.J., Serti, E., et al. (2020). Autoreactive CD8<sup>+</sup> T cell exhaustion distinguishes subjects with slow type 1 diabetes progression. *J. Clin. Invest.* **130**, 480–490. <https://doi.org/10.1172/JCI126595>.
36. Grebinoski, S., Zhang, Q., Cillo, A.R., Manne, S., Xiao, H., Brunazzi, E.A., Tabib, T., Cardello, C., Lian, C.G., Murphy, G.F., et al. (2022). Autoreactive CD8<sup>+</sup> T cells are restrained by an exhaustion-like program that is maintained by LAG3. *Nat. Immunol.* **23**, 868–877. <https://doi.org/10.1038/s41590-022-01210-5>.
37. Mangani, D., Yang, D., and Anderson, A.C. (2023). Learning from the nexus of autoimmunity and cancer. *Immunity* **56**, 256–271. <https://doi.org/10.1016/j.immuni.2023.01.022>.
38. Lennon, V.A., Wingerchuk, D.M., Kryzer, T.J., Pittock, S.J., Lucchinetti, C.F., Fujihara, K., Nakashima, I., and Weinshenker, B.G. (2004). A serum autoantibody marker of neuromyelitis optica: distinction from multiple sclerosis. *Lancet* **364**, 2106–2112. [https://doi.org/10.1016/S0140-6736\(04\)17551-X](https://doi.org/10.1016/S0140-6736(04)17551-X).
39. Lennon, V.A., Kryzer, T.J., Pittock, S.J., Verkman, A.S., and Hinson, S.R. (2005). IgG marker of optic-spinal multiple sclerosis binds to the aquaporin-4 water channel. *J. Exp. Med.* **202**, 473–477. <https://doi.org/10.1084/jem.20050304>.
40. Jarius, S., Paul, F., Weinshenker, B.G., Levy, M., Kim, H.J., and Wildemann, B. (2020). Neuromyelitis optica. *Nat. Rev. Dis. Primers* **6**, 85. <https://doi.org/10.1038/s41572-020-0214-9>.
41. Schmidt, E., and Zillikens, D. (2013). Pemphigoid diseases. *Lancet* **381**, 320–332. [https://doi.org/10.1016/S0140-6736\(12\)61140-4](https://doi.org/10.1016/S0140-6736(12)61140-4).
42. Bacher, P., Schink, C., Teutschbein, J., Kniemeyer, O., Assenmacher, M., Brakhage, A.A., and Scheffold, A. (2013). Antigen-reactive T cell enrichment for direct, high-resolution analysis of the human naive and memory Th cell repertoire. *J. Immunol.* **190**, 3967–3976. <https://doi.org/10.4049/jimmunol.1202221>.
43. Bacher, P., Heinrich, F., Stervbo, U., Nienen, M., Vahldieck, M., Iwert, C., Vogt, K., Kollet, J., Babel, N., Sawitzki, B., et al. (2016). Regulatory T cell Specificity Directs Tolerance versus Allergy against Aeroantigens in Humans. *Cell* **167**, 1067–1078.e16. <https://doi.org/10.1016/j.cell.2016.09.050>.
44. Bacher, P., Rosati, E., Esser, D., Martini, G.R., Saggau, C., Schiminsky, E., Dargvainiene, J., Schröder, I., Wieters, I., Khodamoradi, Y., et al. (2020). Low-Avidity CD4<sup>+</sup> T Cell Responses to SARS-CoV-2 in Unexposed Individuals and Humans with Severe COVID-19. *Immunity* **53**, 1258–1271.e5. <https://doi.org/10.1016/j.immuni.2020.11.016>.
45. Dao, L.M., Machule, M.L., Bacher, P., Hoffmann, J., Ly, L.T., Wegner, F., Scheffold, A., and Prüss, H. (2021). Decreased inflammatory cytokine production of antigen-specific CD4<sup>+</sup> T cells in NMDA receptor encephalitis. *J. Neurol.* **268**, 2123–2131. <https://doi.org/10.1007/s00415-020-10371-y>.
46. Ramien, C., Yusko, E.C., Engler, J.B., Gamradt, S., Patas, K., Schweingruber, N., Willing, A., Rosenkranz, S.C., Diemert, A., Harrison, A., et al. (2019). T Cell Repertoire Dynamics during Pregnancy in Multiple Sclerosis. *Cell Rep.* **29**, 810–815.e4. <https://doi.org/10.1016/j.celrep.2019.09.025>.
47. Marignier, R., Cobo Calvo, A., and Vukusic, S. (2017). Neuromyelitis optica and neuromyelitis optica spectrum disorders. *Curr. Opin. Neurol.* **30**, 208–215. <https://doi.org/10.1097/WCO.0000000000000455>.
48. Marignier, R., Hacoheh, Y., Cobo-Calvo, A., Pröbstel, A.K., Aktas, O., Alexopoulos, H., Amato, M.P., Asgari, N., Banwell, B., Bennett, J., et al. (2021). Myelin-oligodendrocyte glycoprotein antibody-associated disease. *Lancet Neurol.* **20**, 762–772. [https://doi.org/10.1016/S1474-4422\(21\)00218-0](https://doi.org/10.1016/S1474-4422(21)00218-0).
49. Banwell, B., Bennett, J.L., Marignier, R., Kim, H.J., Brilot, F., Flanagan, E.P., Ramanathan, S., Waters, P., Tenenbaum, S., Graves, J.S., et al. (2023). Diagnosis of myelin oligodendrocyte glycoprotein antibody-associated disease: International MOGAD Panel proposed criteria. *Lancet Neurol.* **22**, 268–282. [https://doi.org/10.1016/S1474-4422\(22\)00431-8](https://doi.org/10.1016/S1474-4422(22)00431-8).
50. Sallusto, F. (2016). Heterogeneity of Human CD4(+) T Cells Against Microbes. *Annu. Rev. Immunol.* **34**, 317–334. <https://doi.org/10.1146/annurev-immunol-032414-112056>.
51. Schoenbrunn, A., Frensch, M., Kohler, S., Keye, J., Dooms, H., Moewes, B., Dong, J., Lodenkemper, C., Sieper, J., Wu, P., et al. (2012). A converse 4-1BB and CD40 ligand expression pattern delineates activated regulatory T cells (Treg) and conventional T cells enabling direct isolation of alloantigen-reactive natural Foxp3<sup>+</sup> Treg. *J. Immunol.* **189**, 5985–5994. <https://doi.org/10.4049/jimmunol.1201090>.
52. Brill, L., Vaknin-Dembinsky, A., Zveik, O., Haham, N., Miller, K., and Benedek, G. (2020). MIF -173G/C polymorphism is associated with NMO disease severity. *J. Neuroimmunol.* **339**, 577120. <https://doi.org/10.1016/j.jneuroim.2019.577120>.
53. Mantei, A., Meyer, T., Schürmann, M., Bebler, C., Bias, H., Krieger, D., Bauer, T., Bacher, P., Helmuth, J., Volk, H.D., et al. (2022). Mycobacterium tuberculosis-specific CD4 T-cell scoring discriminates tuberculosis infection from disease. *Eur. Respir. J.* **60**, 2101780. <https://doi.org/10.1183/13993003.01780-2021>.
54. Rao, D.A., Gurish, M.F., Marshall, J.L., Slowikowski, K., Fonseka, C.Y., Liu, Y., Donlin, L.T., Henderson, L.A., Wei, K., Mizoguchi, F., et al. (2017). Pathologically expanded peripheral T helper cell subset drives B cells in rheumatoid arthritis. *Nature* **542**, 110–114. <https://doi.org/10.1038/nature20810>.
55. Moosmann, C., Müller, T.R., Busch, D.H., and Schober, K. (2022). Orthotopic T-cell receptor replacement in primary human T cells using CRISPR-Cas9-mediated homology-directed repair. *Star Protoc.* **3**, 101031. <https://doi.org/10.1016/j.xpro.2021.101031>.
56. Schober, K., Müller, T.R., Gökmen, F., Grassmann, S., Effenberger, M., Poltorak, M., Stemberger, C., Schumann, K., Roth, T.L., Marson, A., et al. (2019). Orthotopic replacement of T-cell receptor alpha- and beta-chains with preservation of near-physiological T-cell function. *Nat. Biomed. Eng.* **3**, 974–984. <https://doi.org/10.1038/s41551-019-0409-0>.
57. Doherty, D.G., Vaughan, R.W., Donaldson, P.T., and Mowat, A.P. (1992). HLA DQA, DQB, and DRB genotyping by oligonucleotide analysis: distribution of alleles and haplotypes in British caucasoids. *Hum. Immunol.* **34**, 53–63. [https://doi.org/10.1016/0198-8859\(92\)90085-2](https://doi.org/10.1016/0198-8859(92)90085-2).
58. Klitz, W., Maiers, M., Spellman, S., Baxter-Lowe, L.A., Schmeckpeper, B., Williams, T.M., and Fernandez-Viña, M. (2003). New HLA haplotype frequency reference standards: high-resolution and large sample typing of HLA DR-DQ haplotypes in a sample of European Americans. *Tissue Antigens* **62**, 296–307. <https://doi.org/10.1034/j.1399-0039.2003.00103.x>.
59. McKinney, E.F., Lee, J.C., Jayne, D.R.W., Lyons, P.A., and Smith, K.G.C. (2015). T-cell exhaustion, co-stimulation and clinical outcome in

- autoimmunity and infection. *Nature* 523, 612–616. <https://doi.org/10.1038/nature14468>.
60. Long, S.A., Thorpe, J., DeBerg, H.A., Gersuk, V., Eddy, J., Harris, K.M., Ehlers, M., Herold, K.C., Nepom, G.T., and Linsley, P.S. (2016). Partial exhaustion of CD8 T cells and clinical response to teplizumab in new-onset type 1 diabetes. *Sci. Immunol.* 1, eaai7793. <https://doi.org/10.1126/sciimmunol.aai7793>.
  61. Grebinoski, S., and Vignali, D.A. (2020). Inhibitory receptor agonists: the future of autoimmune disease therapeutics? *Curr. Opin. Immunol.* 67, 1–9. <https://doi.org/10.1016/j.coi.2020.06.001>.
  62. Gearty, S.V., Dündar, F., Zumbo, P., Espinosa-Carrasco, G., Shakiba, M., Sanchez-Rivera, F.J., Socci, N.D., Trivedi, P., Lowe, S.W., Lauer, P., et al. (2022). An autoimmune stem-like CD8 T cell population drives type 1 diabetes. *Nature* 602, 156–161. <https://doi.org/10.1038/s41586-021-04248-x>.
  63. Tilstra, J.S., Avery, L., Menk, A.V., Gordon, R.A., Smita, S., Kane, L.P., Chikina, M., Delgoffe, G.M., and Shlomchik, M.J. (2018). Kidney-infiltrating T cells in murine lupus nephritis are metabolically and functionally exhausted. *J. Clin. Invest.* 128, 4884–4897. <https://doi.org/10.1172/JCI120859>.
  64. Kew, D., and Kilpatrick, D.L. (1989). Expression and regulation of the proenkephalin gene in rat Sertoli cells. *Mol. Endocrinol.* 3, 179–184. <https://doi.org/10.1210/mend-3-1-179>.
  65. Li, S., Ren, H., Xu, Y., Xu, T., Zhang, Y., Yin, H., Zhang, W., Li, J., Ren, X., Fang, F., et al. (2020). Long-term efficacy of mycophenolate mofetil in myelin oligodendrocyte glycoprotein antibody-associated disorders: A prospective study. *Neurol. Neuroimmunol. Neuroinflamm.* 7, e705. <https://doi.org/10.1212/NXI.0000000000000705>.
  66. Zhang, C., Zhang, M., Qiu, W., Ma, H., Zhang, X., Zhu, Z., Yang, C.S., Jia, D., Zhang, T.X., Yuan, M., et al. (2020). Safety and efficacy of tocilizumab versus azathioprine in highly relapsing neuromyelitis optica spectrum disorder (TANGO): an open-label, multicentre, randomised, phase 2 trial. *Lancet Neurol.* 19, 391–401. [https://doi.org/10.1016/S1474-4422\(20\)30070-3](https://doi.org/10.1016/S1474-4422(20)30070-3).
  67. Traboulsée, A., Greenberg, B.M., Bennett, J.L., Szczechowski, L., Fox, E., Shkrobot, S., Yamamura, T., Terada, Y., Kawata, Y., Wright, P., et al. (2020). Safety and efficacy of satralizumab monotherapy in neuromyelitis optica spectrum disorder: a randomised, double-blind, multicentre, placebo-controlled phase 3 trial. *Lancet Neurol.* 19, 402–412. [https://doi.org/10.1016/S1474-4422\(20\)30078-8](https://doi.org/10.1016/S1474-4422(20)30078-8).
  68. Cree, B.A.C., Bennett, J.L., Kim, H.J., Weinshenker, B.G., Pittock, S.J., Wingerchuk, D.M., Fujihara, K., Paul, F., Cutter, G.R., Marignier, R., et al. (2019). Inebilizumab for the treatment of neuromyelitis optica spectrum disorder (N-Momentum): a double-blind, randomised placebo-controlled phase 2/3 trial. *Lancet* 394, 1352–1363. [https://doi.org/10.1016/S0140-6736\(19\)31817-3](https://doi.org/10.1016/S0140-6736(19)31817-3).
  69. Damato, V., Evoli, A., and Iorio, R. (2016). Efficacy and Safety of Rituximab Therapy in Neuromyelitis Optica Spectrum Disorders: A Systematic Review and Meta-analysis. *JAMA Neurol.* 73, 1342–1348. <https://doi.org/10.1001/jamaneurol.2016.1637>.
  70. Axtell, R.C., and Raman, C. (2012). Janus-like effects of type I interferon in autoimmune diseases. *Immunol. Rev.* 248, 23–35. <https://doi.org/10.1111/j.1600-065X.2012.01131.x>.
  71. Wu, J.H., Zhou, M., Jin, Y., Meng, Z.J., Xiong, X.Z., Sun, S.W., Miao, S.Y., Han, H.L., and Tao, X.N. (2019). Generation and Immune Regulation of CD4<sup>+</sup>CD25<sup>+</sup>Foxp3<sup>+</sup> T Cells in Chronic Obstructive Pulmonary Disease. *Front. Immunol.* 10, 220. <https://doi.org/10.3389/fimmu.2019.00220>.
  72. Ju, B., Zhu, L., Wang, J., Zheng, J., Hao, Z., Luo, J., Zhang, J., Hu, N., An, Q., Feng, X., et al. (2022). The proportion and phenotypic changes of CD4<sup>+</sup>CD25<sup>+</sup>Foxp3<sup>+</sup> T cells in patients with untreated rheumatoid arthritis. *BMC Immunol.* 23, 41. <https://doi.org/10.1186/s12865-022-00517-0>.
  73. Brill, L., Lavon, I., and Vaknin-Dembinsky, A. (2019). Foxp3<sup>+</sup> regulatory T cells expression in neuromyelitis optica spectrum disorders. *Mult. Scler. Relat. Disord.* 30, 114–118. <https://doi.org/10.1016/j.msard.2019.01.047>.
  74. Ma, X., Qin, C., Chen, M., Yu, H.H., Chu, Y.H., Chen, T.J., Bosco, D.B., Wu, L.J., Bu, B.T., Wang, W., et al. (2021). Regulatory T cells protect against brain damage by alleviating inflammatory response in neuromyelitis optica spectrum disorder. *J. Neuroinflammation* 18, 201. <https://doi.org/10.1186/s12974-021-02266-0>.
  75. Chen, P., Wu, M., Wang, N., Xia, F., Du, F., Liu, Z., Wang, J., Jin, J., Jin, B., Zhao, G., et al. (2022). Expression of CD226 is upregulated on Tr1 cells from neuromyelitis optica spectrum disorder patients. *Brain Behav.* 12, e2623. <https://doi.org/10.1002/brb3.2623>.
  76. Cai, H., Liu, Y., Dong, X., Jiang, F., Li, H., Ouyang, S., Yin, W., He, T., Zeng, Q., and Yang, H. (2023). Analysis of LAP<sup>+</sup> and GARP<sup>+</sup> Treg subsets in peripheral blood of patients with neuromyelitis optica spectrum disorders. *Neurol. Sci.* 44, 1739–1747. <https://doi.org/10.1007/s10072-023-06629-8>.
  77. McMurphy, A.N., Gillies, J., Gizzi, M.C., Riba, M., Garcia-Manteiga, J.M., Cittaro, D., Lazarevic, D., Di Nunzio, S., Piras, I.S., Bulfone, A., et al. (2013). A novel function for FOXP3 in humans: intrinsic regulation of conventional T cells. *Blood* 121, 1265–1275. <https://doi.org/10.1182/blood-2012-05-431023>.
  78. Voss, K., Lake, C., Luthers, C.R., Lott, N.M., Dorjbal, B., Arjunaraja, S., Bauman, B.M., Soltis, A.R., Sukumar, G., Dalgard, C.L., et al. (2021). FOXP3 protects conventional human T cells from premature restimulation-induced cell death. *Cell. Mol. Immunol.* 18, 194–205. <https://doi.org/10.1038/s41423-019-0316-z>.
  79. Wing, J.B., Kitagawa, Y., Locci, M., Hume, H., Tay, C., Morita, T., Kidani, Y., Matsuda, K., Inoue, T., Kurosaki, T., et al. (2017). A distinct subpopulation of CD25<sup>+</sup> T-follicular regulatory cells localizes in the germinal centers. *Proc. Natl. Acad. Sci. USA* 114, E6400–E6409. <https://doi.org/10.1073/pnas.1705551114>.
  80. Le Coz, C., Oldridge, D.A., Herati, R.S., De Luna, N., Garifallou, J., Cruz Cabrera, E., Belman, J.P., Püeschel, D., Silva, L.V., Knox, A.V.C., et al. (2023). Human T follicular helper clones seed the germinal center-resident regulatory pool. *Sci. Immunol.* 8, eade8162. <https://doi.org/10.1126/sciimmunol.ade8162>.
  81. Kressler, C., Gasparoni, G., Nordström, K., Hamo, D., Salhab, A., Dimitropoulos, C., Tierling, S., Reinke, P., Volk, H.D., Walter, J., et al. (2020). Targeted De-Methylation of the FOXP3-TSDR Is Sufficient to Induce Physiological FOXP3 Expression but Not a Functional Treg Phenotype. *Front. Immunol.* 11, 609891. <https://doi.org/10.3389/fimmu.2020.609891>.
  82. Laird, C.D., Pleasant, N.D., Clark, A.D., Sneed, J.L., Hassan, K.M.A., Manley, N.C., Vary, J.C., Jr., Morgan, T., Hansen, R.S., and Stöger, R. (2004). Hairpin-bisulfite PCR: assessing epigenetic methylation patterns on complementary strands of individual DNA molecules. *Proc. Natl. Acad. Sci. USA* 101, 204–209. <https://doi.org/10.1073/pnas.2536758100>.
  83. Arand, J., Spieler, D., Karius, T., Branco, M.R., Meilinger, D., Meissner, A., Jenuwein, T., Xu, G., Leonhardt, H., Wolf, V., et al. (2012). In vivo control of CpG and non-CpG DNA methylation by DNA methyltransferases. *PLoS Genet.* 8, e1002750. <https://doi.org/10.1371/journal.pgen.1002750>.
  84. Krueger, F., and Andrews, S.R. (2011). Bismark: a flexible aligner and methylation caller for bisulfite-Seq applications. *Bioinformatics* 27, 1571–1572. <https://doi.org/10.1093/bioinformatics/btr167>.
  85. Lutsik, P., Feuerbach, L., Arand, J., Lengauer, T., Walter, J., and Bock, C. (2011). BiQ Analyzer HT: locus-specific analysis of DNA methylation by high-throughput bisulfite sequencing. *Nucleic Acids Res.* 39, W551–W556. <https://doi.org/10.1093/nar/gkr312>.
  86. Degenhardt, F., Wendorff, M., Wittig, M., Ellinghaus, E., Datta, L.W., Schembri, J., Ng, S.C., Rosati, E., Hübenal, M., Ellinghaus, D., et al. (2019). Construction and benchmarking of a multi-ethnic reference panel for the imputation of HLA class I and II alleles. *Hum. Mol. Genet.* 28, 2078–2092. <https://doi.org/10.1093/hmg/ddy443>.
  87. Picelli, S., Faridani, O.R., Björklund, A.K., Winberg, G., Sagasser, S., and Sandberg, R. (2014). Full-length RNA-seq from single cells using Smart-seq2. *Nat. Protoc.* 9, 171–181. <https://doi.org/10.1038/nprot.2014.006>.

88. Wu, T.D., and Nacu, S. (2010). Fast and SNP-tolerant detection of complex variants and splicing in short reads. *Bioinformatics* 26, 873–881. <https://doi.org/10.1093/bioinformatics/btq057>.
89. Liao, Y., Smyth, G.K., and Shi, W. (2014). featureCounts: an efficient general purpose program for assigning sequence reads to genomic features. *Bioinformatics* 30, 923–930. <https://doi.org/10.1093/bioinformatics/btt656>.
90. Stubbington, M.J.T., Lönnberg, T., Proserpio, V., Clare, S., Speak, A.O., Dougan, G., and Teichmann, S.A. (2016). T cell fate and clonality inference from single-cell transcriptomes. *Nat. Methods* 13, 329–332. <https://doi.org/10.1038/nmeth.3800>.
91. Hao, Y., Hao, S., Andersen-Nissen, E., Mauck, W.M., 3rd, Zheng, S., Butler, A., Lee, M.J., Wilk, A.J., Darby, C., Zager, M., et al. (2021). Integrated analysis of multimodal single-cell data. *Cell* 184, 3573–3587.e29. <https://doi.org/10.1016/j.cell.2021.04.048>.
92. Korsunsky, I., Millard, N., Fan, J., Slowikowski, K., Zhang, F., Wei, K., Baglaenko, Y., Brenner, M., Loh, P.R., and Raychaudhuri, S. (2019). Fast, sensitive and accurate integration of single-cell data with Harmony. *Nat. Methods* 16, 1289–1296. <https://doi.org/10.1038/s41592-019-0619-0>.
93. Krämer, A., Green, J., Pollard, J., Jr., and Tugendreich, S. (2014). Causal analysis approaches in Ingenuity Pathway Analysis. *Bioinformatics* 30, 523–530. <https://doi.org/10.1093/bioinformatics/btt703>.
94. Wickham, H. (2016). *ggplot2: Elegant Graphics for Data Analysis. Use R!, Second Edition* (Springer International Publishing).
95. Szklarczyk, D., Franceschini, A., Wyder, S., Forslund, K., Heller, D., Huerta-Cepas, J., Simonovic, M., Roth, A., Santos, A., Tsafou, K.P., et al. (2015). STRING v10: protein-protein interaction networks, integrated over the tree of life. *Nucleic Acids Res.* 43, D447–D452. <https://doi.org/10.1093/nar/gku1003>.
96. Trapnell, C., Cacchiarelli, D., Grimsby, J., Pokharel, P., Li, S., Morse, M., Lennon, N.J., Livak, K.J., Mikkelsen, T.S., and Rinn, J.L. (2014). The dynamics and regulators of cell fate decisions are revealed by pseudotemporal ordering of single cells. *Nat. Biotechnol.* 32, 381–386. <https://doi.org/10.1038/nbt.2859>.
97. Levine, J.H., Simonds, E.F., Bendall, S.C., Davis, K.L., Amir el, A.D., Tadmor, M.D., Litvin, O., Fienberg, H.G., Jager, A., Zunder, E.R., et al. (2015). Data-Driven Phenotypic Dissection of AML Reveals Progenitor-like Cells that Correlate with Prognosis. *Cell* 162, 184–197. <https://doi.org/10.1016/j.cell.2015.05.047>.

STAR★METHODS

KEY RESOURCES TABLE

REAGENT or RESOURCE	SOURCE	IDENTIFIER
<b>Antibodies</b>		
CD3-PE (clone: REA613)	Miltenyi Biotec	Cat#130-113-139; RRID: AB_2725967
CD4-APC-Vio770 (clone: M-T466)	Miltenyi Biotec	Cat#130-113-251; RRID: AB_2726053
CD4-VioBlue (clone: REA623)	Miltenyi Biotec	Cat#130-114-534; RRID: AB_2726691
CD4-FITC (clone: REA623)	Miltenyi Biotec	Cat#130-114-585; RRID: AB_2726703
CD8-VioGreen (clone: REA734)	Miltenyi Biotec	Cat#130-110-684; RRID: AB_2659241
CD8-PerCP (clone: BW135/80)	Miltenyi Biotec	Cat#130-113-160; RRID: AB_2725988
CD14-VioGreen (clone: REA599)	Miltenyi Biotec	Cat#130-110-525; RRID: AB_2655057
CD14-PerCP (clone: TÜK4)	Miltenyi Biotec	Cat#130-113-150; RRID: AB_2725978
CD20-VioGreen (clone: LT20)	Miltenyi Biotec	Cat#130-113-379; RRID: AB_2726147
CD20-PerCP (clone: LT20)	Miltenyi Biotec	Cat#130-113-376; RRID: AB_2726144
CD19-BV711 (clone: SJ25C1)	Biolegend	Cat#363022; RRID: AB_2564231
CD27-BV421 (clone: M-T271)	Biolegend	Cat#356418; RRID: AB_2562599
CD45RA-VioGreen (clone: REA562)	Miltenyi Biotec	Cat#130-113-369; RRID: AB_2726139
CD45RO-APC (clone: REA611)	Miltenyi Biotec	Cat#130-113-556; RRID: AB_2733381
CD69-PE (clone: REA824)	Miltenyi Biotec	Cat#130-112-613; RRID: AB_2659065
CD69-PE (clone: FN50)	Biolegend	Cat#310906; RRID: AB_314841
CD154-FITC (clone: REA238)	Miltenyi Biotec	Cat#130-113-612; RRID: AB_2751146
CD154-APC (clone: REA238)	Miltenyi Biotec	Cat#130-113-610; RRID: AB_2733342
CD137-BV605 (clone: 4B4-1)	Biolegend	Cat#309822; RRID: AB_2565997
CD137-PE (clone: REA765)	Miltenyi Biotec	Cat#130-110-763; RRID: AB_2654986
TNF- $\alpha$ -PE-Vio770 (clone: cA2)	Miltenyi Biotec	Cat#130-120-492; RRID: AB_2784483
CD197 (CCR7)-PE-Bio770 (clone: REA108)	Miltenyi Biotec	Cat#130-118-350; RRID: AB_2733213
CCR7-BV785 (clone: G043H7)	Biolegend	Cat#353230; RRID: AB_2563630
CCR7-FITC (clone: REA108)	Miltenyi Biotec	Cat#130-117-700; RRID: AB_2751410
CD25-PE (clone: REA570)	Miltenyi Biotec	Cat#130-113-286; RRID: AB_2733792
CD25-BV650 (clone: BC96)	Biolegend	Cat#302634; RRID: AB_2563807
CD127-APC (clone: REA614)	Miltenyi Biotec	Cat#130-113-413; RRID: AB_2726161
CD127-BV570 (clone: A019D5)	Biolegend	Cat#351307; RRID: AB_10900064
IL-21-PE (clone: REA1039)	Miltenyi Biotec	Cat#130-117-421; RRID: AB_2727941
CD38-APC-Fire810 (clone: S17015A)	Biolegend	Cat#397124; N/A
GM-CSF-APC (clone: REA1215)	Miltenyi Biotec	Cat#130-123-420; RRID: AB_2811516
GM-CSF-PE-Vio770 (clone: REA1215)	Miltenyi Biotec	Cat#130-123-422; RRID: AB_2811517
GM-CSF-PE (clone: REA1215)	Miltenyi Biotec	Cat#130-123-419; RRID: AB_2811515
CD45RO-PE-Vio770 (clone: REA611)	Miltenyi Biotec	Cat#130-113-560; RRID: AB_2751129
CD45RO-PE-Cy5 (clone: UCHL1)	Biolegend	Cat#304208; RRID: AB_314424
CD154 MicroBeads kit	Miltenyi Biotec	Cat#130-092-658; N/A
CD14 MicroBeads, human	Miltenyi Biotec	Cat#130-050-201; RRID: AB_2665482
Anti-PE MicroBeads, ultra pure	Miltenyi Biotec	Cat#130-105-639; RRID: AB_3101796
Anti-APC MicroBeads	Miltenyi Biotec	130-090-855; RRID: AB_244367
CD39-VioBlue (clone: MZ18-23C8)	Miltenyi Biotec	Cat#130-128-928; RRID: AB_2893087
CD45RO-APC-Vio770 (clone: REA611)	Miltenyi Biotec	Cat#130-113-557; RRID: AB_2733130
CD28 pure – functional grade, human (clone: 15E8)	Miltenyi Biotec	Cat#130-093-375; RRID: AB_1036134
CD40 pure – functional grade, human (clone: HB14)	Miltenyi Biotec	Cat#130-094-133; RRID: AB_10839704

(Continued on next page)

**Continued**

REAGENT or RESOURCE	SOURCE	IDENTIFIER
CD3 pure – functional grade, human (clone: OKT3)	Miltenyi Biotec	Cat#130-093-387; RRID: AB_1036144
CD4-BV421 (clone: OKT4)	BioLegend	Cat#317434; RRID: AB_2562134
CD45RA-PE-Cy5 (clone: HI100)	BioLegend	Cat#304110; RRID: AB_314414
Helios-PE-Cy7 (clone: 22F6)	BioLegend	Cat#137236; RRID: AB_2565990
Helios-FITC (clone: REA829)	Miltenyi Biotec	Cat#130-112-629; RRID: AB_2651978
IL-2-BV605 (clone: MQ1-17H12)	BioLegend	Cat#500332; RRID: AB_2563877
IL-2-BV650 (clone: MQ1-17H12)	BioLegend	Cat#500334; RRID: AB_2563878
IL-2-APC-Vio770 (clone: N7.48A)	Miltenyi Biotec	Cat#130-120-249; RRID: AB_2784380
IFN- $\gamma$ -BV570 (clone: 4S.B3)	BioLegend	Cat#502534; RRID: AB_2563880
IFN- $\gamma$ -PerCP-Cy5.5 (clone: 4S.B3)	BioLegend	Cat#502526; RRID: AB_961355
TNF- $\alpha$ -AF700 (clone: Mab11)	BioLegend	Cat#502928; RRID: AB_2561315
Foxp3-AF647 (clone: 206D)	BioLegend	Cat#320114; RRID: AB_439754
Foxp3-PE-Cy7 (clone: 236A/E7)	Invitrogen	Cat#25-4777-42; RRID: AB_2573450
IL-17A-BV650 (clone: N49-653)	BD Biosciences	Cat#563746; RRID: AB_2738402
BCL-6-PE (clone: K112-91)	BD Biosciences	Cat#561522; RRID: AB_10717126
TOX-PE (clone: REA473)	Miltenyi Biotec	Cat#130-120-716; RRID: AB_2801780
PD-1-BV711 (clone: EH12.2H7)	BioLegend	Cat#329928; RRID: AB_2562911
PD-1-FITC (clone: EH12.2H7)	BioLegend	Cat#329904; RRID: AB_940479
PD-1-PE-Dazzle-594 (clone: EH12.2H7)	BioLegend	Cat#329940; RRID: AB_2563659
TIGIT-PE-Dazzle-594 (clone: A15153G)	BioLegend	Cat#372716; RRID: AB_2632931
CTLA-4-BV785 (clone: BNI3)	BioLegend	Cat#369624; RRID: AB_2810582
CTLA-4-BV605 (clone: BNI3)	BioLegend	Cat#369610; RRID: AB_2632779
ICOS-BV750 (clone: C398.4A)	BioLegend	Cat#313558; N/A
CXCR5-PE-Fire700 (clone: J252D4)	BioLegend	Cat#356954; N/A
CXCR5-PE-Dazzle-594 (clone: J252D4)	BioLegend	Cat#356928; RRID: AB_2563689
Ki-67-BV480 (clone: B56)	BD Biosciences	Cat#566172; RRID: AB_2739569
IL-22-PerCP-eFluor710 (clone: IL22JOP)	Invitrogen	Cat#46-7222-82; RRID: AB_2573839
IgD-APC-Cy7 (clone: IA6-2)	BioLegend	Cat#348218; RRID: AB_11203722
Mouse TCR $\beta$ -APC (clone: H57-597)	BioLegend	Cat#109212; RRID: AB_313435
Human TCR $\alpha\beta$ -FITC (clone: IP26)	BioLegend	Cat#306706; RRID: AB_314644
CD4-AF700 (clone: 63D3)	Self-made	N/A
CD14-PacBlue (clone: 63D3)	Self-made	N/A
CD38-AF647 (clone: OKT10)	Self-made	N/A
CD45RA-FITC (clone: 4G11)	Self-made	N/A
CD45RO-FITC (clone: UCHL1)	Self-made	N/A
Tetramer-PE	Miltenyi Biotec	N/A
Tetramer-APC	Miltenyi Biotec	N/A
<b>Peptide Pools</b>		
AQP-4	Peptides & Elephants	N/A
MOG	JPT	N/A
Influenza A H1N1 (HA)	Miltenyi Biotec	Cat#130-099-803
<i>Candida albicans</i> MP65	Miltenyi Biotec	Cat#130-096-776
SLA	Peptides & Elephants	N/A
BP180	Peptides & Elephant	N/A
<b>Chemicals, Peptides, and Recombinant Proteins</b>		
Human AB Serum	Merck	N/A
RPMI-1640 medium	GIBCO, Life Technologies	Cat#52400-025
TexMACS medium	Miltenyi Biotec	Cat#130-097-196

(Continued on next page)

<b>Continued</b>		
REAGENT or RESOURCE	SOURCE	IDENTIFIER
X-Vivo15 medium	Lonza	Cat#BE02-060F
Human IL-2 (Proleukin)	Novartis	N/A
Human IL-4	Miltenyi Biotec	Cat#130-093-922
Human GM-CSF	Miltenyi Biotec	Cat#130-093-866
Brefeldin A	Sigma Aldrich	Cat#B6542
<b>Critical Commercial Assays</b>		
MS Columns	Miltenyi Biotec	Cat#130-042-201
LS Columns	Miltenyi Biotec	Cat#130-042-401
Viability 405/520 Fixable Dye	Miltenyi Biotec	Cat#130-130-404
FoxP3 Staining Buffer Set	Miltenyi Biotec	Cat#130-093-142
Amatax P3 Primary Cell 4-D Nucleofector X Kit S	Lonza	Cat#VPXP-3032
<b>Software and Algorithms</b>		
FlowJo	BD Biosciences	RRID:SCR_008520
MACSQuantify	Miltenyi Biotec	Cat#130-094-556
GraphPad Prism 9.5.1.	GraphPad	RRID:SCR_000306
GSNAP (v2019-06-10)	<a href="https://doi.org/10.1093/bioinformatics/btq057">https://doi.org/10.1093/bioinformatics/btq057</a>	<a href="http://research-pub.gene.com/gmap/archive.html">http://research-pub.gene.com/gmap/archive.html</a>
FeatureCounts (v2.0.1)	<a href="https://doi.org/10.1093/bioinformatics/btt656">https://doi.org/10.1093/bioinformatics/btt656</a>	<a href="https://subread.sourceforge.net/">https://subread.sourceforge.net/</a>
R	R development Core Team	<a href="http://www.R-project.org">http://www.R-project.org</a>
TraCeR (v0.5)	<a href="https://doi.org/10.1038/nmeth.3800">https://doi.org/10.1038/nmeth.3800</a>	<a href="https://github.com/teichlab/tracer">https://github.com/teichlab/tracer</a>
Seurat R package (v4.3.0)	<a href="https://doi.org/10.1016/j.cell.2021.04.048">https://doi.org/10.1016/j.cell.2021.04.048</a>	<a href="https://satijalab.org/seurat/">https://satijalab.org/seurat/</a>
Harmony R package (v0.1.1)	<a href="https://doi.org/10.1038/s41592-019-0619-0">https://doi.org/10.1038/s41592-019-0619-0</a>	<a href="https://github.com/immunogenomics/harmony">https://github.com/immunogenomics/harmony</a>
Monocle3 R package (v1.3.7)	<a href="https://doi.org/10.1038/nbt.2859">https://doi.org/10.1038/nbt.2859</a>	<a href="https://cole-trapnell-lab.github.io/monocle3/">https://cole-trapnell-lab.github.io/monocle3/</a>
Ingenuity Pathway Analysis (IPA, v45868156)	QIAGEN	<a href="http://www.ingenuity.com/products/pathways_analysis.html">http://www.ingenuity.com/products/pathways_analysis.html</a>
<b>Deposited Data</b>		
Sequencing data	Gene expression omnibus	GEO: GSE242232

## EXPERIMENTAL MODEL AND STUDY PARTICIPANT DETAILS

NMOSD and MOGAD patient peripheral EDTA blood samples (50–75ml) were obtained from the Department of Neurology, UKSH Kiel and Lübeck, Germany, the Department of Neurology, Charité Berlin, Germany and the Clinic and Polyclinic for Neurology, University Medical Center Hamburg-Eppendorf, Germany. Buffy coats or EDTA blood samples of all healthy controls were obtained from blood bank donors of the Institute for Transfusion Medicine, UKSH Kiel, Germany, the Charité blood bank, Charité Berlin, Germany or from in-house volunteers (approval by the local ethics committee: NMOSD/MOGAD patients Kiel/Lübeck: 498/19, B300/19; NMOSD patients Berlin: EA1/041/14, EA1/362/20; healthy controls D578/18). AIH patient peripheral EDTA blood samples (50–75ml) were obtained from the Department of Medicine, University Medical Center Hamburg-Eppendorf, Germany (approval by the local ethics committee: PV4081). BP patient peripheral EDTA blood samples (50–75ml) were obtained from the Department of Dermatology, UKSH Kiel and Lübeck, Germany (approval by the local ethics committee: Kiel B323/21, Lübeck 21-368). Peripheral blood mononuclear cells (PBMCs) were freshly isolated from EDTA blood on the day of blood donation by density gradient centrifugation (Biocoll; Biochrom, Berlin, Germany). Demographic data about the study participants is provided in [Table S1](#). All patients and blood donors gave written informed consent.

## METHOD DETAILS

### Cell lines

Bare lymphocyte syndrome (BLS) cell line stably expressing DQA1\*01:02/DQB1\*06:02 (DQw6) were provided by Reza Naghavian and Roland Martin (Neuroimmunology and MS Research Section, University Hospital Zurich, Switzerland) (originally gifted by

W.W. Kwok (Benaroya Research Institute, Seattle). Cells were expanded in RPMI-1640 medium (GIBCO) supplemented with 10% heat-inactivated fetal bovine serum (FCS (Gibco)), 2mM L-glutamine (BIOWEST), 100 IU/mL penicillin/streptomycin (AppliChem GmbH) on 6-well culture plates. During expansion, medium was replenished, and cells were split as required.

### Antigens

AQP-4 and MOG peptide pools of lyophilized 15-mer peptides with 11-amino acid overlap, covering the complete protein sequence were purchased from JPT (Berlin, Germany) and peptides & elephants (Hennigsdorf, Germany). SLA- and BP180 peptide pools of lyophilized 15-mer peptides with 11-amino acid overlap, covering the immunogenic parts of the protein were purchased from peptides & elephants (Hennigsdorf, Germany). Influenza A H1N1 (HA) and *C. albicans* MP65 peptide pools were purchased from Miltenyi Biotec (Bergisch Gladbach, Germany). Peptides were resuspended according to manufacturers' instructions and T cells were stimulated at a concentration of 1 µg/peptide/ml until otherwise indicated.

### Antigen-reactive T cell enrichment

Antigen-reactive T cell enrichment was performed as previously described with slight modifications.  $2.5 \times 10^7$  PBMCs were plated in 2 ml RPMI-1640 medium (GIBCO), supplemented with 5% (v/v) human AB-serum (Sigma Aldrich, Schnelldorf, Germany) in 6-well cell culture plates and stimulated for 7 h in presence of 1 µg/ml CD40 pure antibody (Miltenyi Biotec, Bergisch Gladbach, Germany). 1 µg/ml Brefeldin A (Sigma Aldrich) was added for the last 1.5 h. To multiplex several specificities, the differential stimulated cells were labeled with different concentrations of two CD4-antibody clones (CD4-BV421, clone OKT4, titer 1:20 and 1:200; CD4-APC-Vio770, clone MT-466, titer 1:50 and 1:500). For lower concentrations the respective unconjugated CD4 pure antibody was added at a concentration of 1 µg/ml to block intermixing of the barcode label. Barcoded populations were pooled and labeled with CD154-Biotin followed by anti-Biotin MicroBeads (CD154 MicroBead Kit, Miltenyi Biotec) and magnetically enriched by two sequential MS columns (Miltenyi Biotec). Surface staining was performed on the first column, followed by fixation and intracellular staining on the second column. Frequencies of antigen-specific T cells were determined based on the cell count of CD154+ T cells after enrichment, normalized to the total number of CD4+ T cells applied on the column. For each stimulation, CD154+ background cells enriched from the non-stimulated control were subtracted.

### Flow cytometry

Live/dead discrimination was performed by using Viability 405/520 Fixable Dye (Miltenyi Biotec). For intracellular staining cells were fixed and permeabilized with the FOXP3 staining buffer set (Miltenyi Biotec). Data were acquired on a MACSQuant Analyzer 16 (Miltenyi Biotec), LRS Fortessa (BD Bioscience, San Jose, CA, USA), Northern Lights 3000 (Cytek Biosciences) or Aurora (Cytek Biosciences). Expanded T cell clones were screened on 384-well plates on a MACSQuantX Analyzer (Miltenyi Biotec). FlowJo software (Treestar, Ashland, OR, USA) was used for analysis.

### Expansion and re-stimulation of antigen-reactive T cells

For expansion of antigen-specific memory T cell clones, PBMCs were stimulated for 6 h. CD154+ cells were isolated by magnetic enrichment and further purified by FACS sorting on a FACS Aria Fusion (BD Bioscience, San Jose, CA, USA) based on dual expression of CD154 and CD69 and expression of CD45RO. Purified CD154+ memory T cell clones were expanded in presence of  $1 \times 10^5$  autologous antigen-loaded irradiated feeder cells in TexMACS medium (Miltenyi Biotec), supplemented with 5% (v/v) human AB-serum (GemCell), 200 U/ml IL-2 (Proleukin; Novartis, Nürnberg, Germany), 100 IU/mL penicillin, 100 mg/mL streptomycin, 0.25 mg/mL amphotericin B (Antibiotic Antimycotic Solution, Sigma Aldrich), 1% Non-essential Amino Acid Solution (Sigma Aldrich), 30 ng/mL anti-CD3 (OKT3, Miltenyi Biotec) and 0.5 µg/mL anti-CD28 pure (Miltenyi Biotec). For some experiments 25 µg/mL Abatacept and 5 µg/mL Nivolumab (both provided by the UKSH, Kiel, Germany) were added into the medium in the beginning of the cultures. During expansion for 2-3 weeks, medium was replenished, and cells were split as required. For re-stimulation, fastDCs were generated from autologous CD14+ MACS isolated monocytes (CD14 MicroBeads; Miltenyi Biotec) by cultivation in X-Vivo15 medium (BioWhittaker/Lonza), supplemented with 1000 IU/mL GM-CSF and 400 IU/mL IL-4 (both Miltenyi Biotec). Before re-stimulation expanded T cells were rested in RPMI-1640 supplemented with 5% human AB-serum without IL-2 for 2 days.  $0.3\text{--}1 \times 10^5$  expanded T cells were plated with fastDCs in a 1:1 ratio in 384-well flat bottom plates and re-stimulated for 6 h, with 1 µg/mL Brefeldin A (Sigma Aldrich) added for the last 4 h. To determine the MHC-restriction, in some experiments 20 µg/mL pure HLA-DR (Miltenyi Biotec), HLA-DQ (Biolegend) or HLA-DP (ichor.bio) antibodies were added and pre-incubated for 30 minutes.

### Analysis of functional avidity

For determining the functional avidity, *in vitro* expanded AQP-4-specific T cell clones were re-challenged with decreasing antigen concentrations (1, 0.25, 0.1, 0.025, 0.0025, 0.00025 µg/peptide/mL) and analyzed for re-expression of CD154 and cytokines. Antigen concentrations required for half-maximal response ( $EC_{50}$  values) were calculated from dose-response curves using GraphPad PRISM. These curves were plotted as a semi-logarithmic plot, where the amount of antigen is plotted (on the X axis) as the log of antigen concentration and the response is plotted (on the Y axis) using a linear scale. To compare the  $EC_{50}$  values of different donors, the bottom and top of the curve were defined as 0 and 100%, respectively.

### Peptide Screening

For identifying immunodominant peptides, AQP-4-specific T cells clones were pooled and re-challenged not only with the AQP-4 peptide pool, but also with the single 15-mer peptides with 11-amino acid overlap, covering the complete protein sequence (78 peptides in total, peptides&elephants).

### HDR Template Design

DNA templates were designed *in silico* based on the previously published method<sup>55</sup> and were synthesized by Twist Biosciences (San Francisco, California, USA) in pTwist Amp vectors. Briefly, the constructs comprise the full length of the  $\alpha$  and  $\beta$  chains of the inserting TCRs flanked by left and right homology arms (LHA and RHA) and contain self-cleaving peptides (P2A and T2A) to provide separation, as well as a poly-A tail (bGHpA). The  $\beta$ -chain consists of the human variable region and the murine constant region, which is used as tracking marker.

### Orthotopic T cell receptor replacement in primary human CD4+ T cells

T cell receptor replacement was performed as previously described.<sup>55</sup> In brief, PBMCs were freshly isolated from EDTA blood by density gradient centrifugation, and CD4+ T cells were magnetically isolated by using the CD4+ T Cell Isolation Kit (Miltenyi Biotec) according to the manufacturer's instruction.  $4 \times 10^7$  cells were plated on 6-well cell culture plates in TexMACS medium (Miltenyi Biotec), supplemented with 5% (v/v) human AB-serum (GemCell), 200 U/mL IL-2 (Proleukin; Novartis, Nurnberg, Germany), and 100 IU/mL penicillin, 100 mg/mL streptomycin, 0.25 mg/mL amphotericin B (Antibiotic Antimycotic Solution, Sigma Aldrich). CD4+ T cells were subsequently activated for 2 days using the T Cell Activation/Expansion Kit (Miltenyi Biotec) according to the manufacturer's instruction. After 48 h, the activated CD4+ T cells were harvested, and the activation beads were removed by placing the cell suspension in the magnetic field of the MACSiMAG Separator (Miltenyi Biotec). For each nucleofection,  $1 \times 10^6$  cells were used and mixed with 20  $\mu$ M ribonucleoprotein (RNP) mixtures (Integrated DNA Technologies, Coralville, IA, USA) and an HDR template (1  $\mu$ g) (Twist Biosciences, San Francisco, California, USA). The RNPs (all components Integrated DNA Technologies, Coralville, IA, USA) were generated in 2 sequential steps: First, the guide RNAs were prepared by mixing equal volumes of tracrRNA (80  $\mu$ M stock) with hTRAC crRNA (80  $\mu$ M stock) (TRACguide1: TGGATTAGAGTCTCTCAGC, TRACguide2: ACAAACTGTGCTAGACATG, TRACguide3: AGAGTCTCTCAGCTGGTACA) and heating at 95°C for 5 minutes, followed by cooling to RT. In the second step, guide RNAs were assembled with Cas9 nuclease by mixing equal volumes of Cas9 nuclease (6  $\mu$ M) and gRNA (40  $\mu$ M) and incubated at RT for 15 minutes. An electroporation enhancer was added to the RNP mixtures. The P3 Primary Cell 4D-Nucleofector X Kit S (Lonza) and a 4D nucleofector X unit (Lonza) with the EH100 electroporation program were used for electroporation. Electroporated cells were immediately transferred to 96-well cell culture plates in TexMACS medium (Miltenyi Biotec), supplemented with 5% (v/v) human AB-serum (GemCell), 200 U/mL IL-2 (Proleukin; Novartis, Nurnberg, Germany), and 100 IU/mL penicillin, 100 mg/mL streptomycin, 0.25 mg/mL amphotericin B (Antibiotic Antimycotic Solution, Sigma Aldrich) and were incubated for 5 days at 37°C, 5% CO<sub>2</sub>. After 5 days, TCR-transgenic CD4+ T cells were FACS sorted on a FACS Aria Fusion (BD Bioscience, San Jose, CA, USA) based on their mouse TCR $\beta$  expression and were further expanded for 2-3 weeks in presence of  $2 \times 10^5$  irradiated allogeneic feeder cells until subsequent functional assays were performed. For FACS sorting, cells were stained with fluorochrome-conjugated antibodies to CD4-Vioblu, CD3-PE, CD8-PerCP, CD14-PerCP, CD20-PerCP (all Miltenyi Biotec) and mouse TCR  $\beta$  chain-APC, as well as human TCR  $\alpha/\beta$  chain-FITC (both Biolegend). During expansion medium was replenished, and cells were split as required.

### HLA class II tetramer enrichment

HLA-DQ6:AQP-4(Peptide26:TVAMVCTRKISIAKS; AQP4<sub>101-115</sub>) tetramers were customized by Miltenyi Biotec (Bergisch Gladbach, Germany) conjugated to two different fluorochromes (PE and APC).  $2-4 \times 10^7$  freshly isolated PBMCs were stained for 1h at 37°C in 200  $\mu$ l TexMACS medium (Miltenyi Biotec) under constant rotation. The tetramers were each used in a 1:11 ratio (2  $\mu$ g/mL). The cells were washed, labeled with anti-PE and anti-APC Microbeads (Miltenyi Biotec) and magnetically enriched by two sequential MS columns (Miltenyi Biotec). Surface staining was performed on the column, followed by fixation and intracellular staining on the second column. Frequencies of antigen-specific T cells were determined based on the cell count of tetramer APC/PE double positive T cells after enrichment, normalized to the total number of CD4+ T cells applied on the column.

### T cell/B cell cooperation assay

AQP-4-reactive T cell clones from NMOSD patients and healthy donors were co-cultured for 5 days with heterologous memory or naive B cells at a 1:4 ratio in the presence of the AQP-4 peptide pool. CD19+ B cells were isolated from PBMC by magnetic enrichment and further purified by FACS sorting on a FACS Aria Fusion (BD Bioscience, San Jose, CA, USA) as DAPI-CD4-CD19+CD38-IgD- memory B cells and either IgD+ naive or IgD- memory B cells. To block T cell help, an antibody against CD40L (clone 24-31; 10  $\mu$ g/ml) and/or recombinant soluble IL-21 receptor (Biolegend; 10  $\mu$ g/ml) were added. After 5 days, plasmablast formation was assessed by staining of single-cell suspensions on ice and samples were acquired on an LSRFortessa cell analyzer (BD Bioscience). Live/dead discrimination was performed by staining with DAPI. Plasmablasts were identified as CD27<sup>high</sup> CD38<sup>high</sup>.

### Chronic stimulation assay

PBMCs were freshly isolated from EDTA blood by density gradient centrifugation, and naive CD4+ T cells were magnetically isolated using the Naive CD4+ T Cell Isolation Kit II (Miltenyi Biotec) according to the manufacturer's instructions and further purified by FACS

sorting based on dual expression of CD4 and CD127 and lack of expression of CD25 and CD45RO.  $1 \times 10^5$  cells were plated in a 1:1 ratio with autologous irradiated APCs on 96-well cell culture plates in TexMACS medium (Miltenyi Biotec) supplemented with 5% (v/v) human AB-serum (GemCell), 200 U/mL IL-2 (Proleukin; Novartis, Nurnberg, Germany), 100 IU/mL penicillin, 100 mg/mL streptomycin, 0.25 mg/mL amphotericin B (Antibiotic Antimycotic Solution, Sigma Aldrich) and 0.5  $\mu$ g/mL anti-CD28 pure (Miltenyi Biotec). CD4+ T cells were subsequently activated once or daily with 1  $\mu$ g/mL staphylococcus enterotoxin b (SEB) over a period of 7 days. During the expansion, the medium was replenished every day. After 7 days, CD4+ T cells were re-stimulated with SEB. For re-stimulation, APCs were generated from autologous CD14+ MACS isolated monocytes (CD14 MicroBeads; Miltenyi Biotec). Prior to re-stimulation expanded T cells were rested for 2 days in RPMI-1640 supplemented with 5% human AB-serum without IL-2.  $5 \times 10^4$  expanded T cells were plated with APCs at a 1:1 ratio in 384-well flat bottom plates and re-stimulated for 6 h, with 1  $\mu$ g/mL Brefeldin A (Sigma Aldrich) added for the last 4 h.

### FOXP3<sup>-/-</sup> via CRISPR/Cas9

PBMCs were freshly isolated from EDTA blood by density gradient centrifugation, and CD4+ T cells were magnetically isolated by using the Naïve CD4+ T Cell Isolation Kit II (Miltenyi Biotec) according to the manufacturer's instruction.  $2 \times 10^7$  cells were plated on 12-well cell culture plates in TexMACS medium (Miltenyi Biotec), supplemented with 5% (v/v) human AB-serum (GemCell), 200 U/mL IL-2 (Proleukin; Novartis, Nurnberg, Germany), and 100 IU/mL penicillin, 100 mg/mL streptomycin, 0.25 mg/mL amphotericin B (Antibiotic Antimycotic Solution, Sigma Aldrich). CD4+ T cells were subsequently activated for 2 days using the T Cell Activation/Expansion Kit (Miltenyi Biotec) according to the manufacturer's instructions. After 48 h, the activated CD4+ T cells were harvested, and the activation beads were removed by placing the cell suspension in the magnetic field of the MACSiMAG Separator (Miltenyi Biotec). For each nucleofection,  $2 \times 10^5$ – $1 \times 10^6$  cells were used and mixed with ribonucleoprotein (RNP) mixtures (Integrated DNA Technologies, Coralville, IA, USA). The RNPs (all components Integrated DNA Technologies, Coralville, IA, USA) were prepared in 2 sequential steps: First, the guide RNAs were prepared by mixing equal volumes of tracrRNA (100  $\mu$ M stock) with crRNA (100  $\mu$ M stock) (FOXP3guide1: AGGACCCGATGCCCAACCCC, FOXP3guide2: GCAGCTGCGATGGTGGCATG, FOXP3guide3: CCCACCCACAGGGATCAACG) and heating at 95°C for 5 minutes, followed by cooling to RT and pooling all three tracrRNA-crRNA mixtures. In the second step, guide RNAs were assembled with Cas9 nuclease by mixing 2  $\mu$ L of Cas9 nuclease (60 pmol) and 3  $\mu$ L gRNA and incubated at RT for 10 minutes. An electroporation enhancer was added to the RNP mixtures. The P3 Primary Cell 4D-Nucleofector X Kit S (Lonza) and a 4D nucleofector X unit (Lonza) with the EH100 electroporation program were used for electroporation. A pulse-only control was processed equally. Electroporated cells were immediately transferred to 96-well cell culture plates in TexMACS medium (Miltenyi Biotec), supplemented with 5% (v/v) human AB-serum (GemCell), 200 U/mL IL-2 (Proleukin; Novartis, Nurnberg, Germany), and 100 IU/mL penicillin, 100 mg/mL streptomycin, 0.25 mg/mL amphotericin B (Antibiotic Antimycotic Solution, Sigma Aldrich) and were incubated overnight at 37°C, 5% CO<sub>2</sub>. The next day, samples were divided equally between two wells and irradiated autologous APCs were added in equal proportions, followed by the chronic stimulation assay (see section above).

### Bisulfite Treatment and Methylation Analysis

The DNA methylation degree of CpG sites in the *FOXP3-TSDR* region was determined by NGS-based high-resolution bisulfite amplicon sequencing (BAS, similar to<sup>81</sup>) or bisulfite hairpin amplicon sequencing (BHAS).<sup>82,83</sup> Briefly, DNA was isolated from AQP4-reactive T cell clones. For BAS, DNA was isolated using the QIAmp DNA Mini Kit (QIAGEN) according to manufacturer's instructions. For BHAS, cells were lysed in 10mM TrisHCl (Carl Roth), 5mM EDTA (Carl Roth) and 3  $\mu$ g Proteinase K (Sigma-Aldrich) and incubated for 3–4 h at 65 °C. For BHAS, inactivation of Proteinase K was done by adding 1 mM Pefabloc<sup>®</sup>SC (Sigma-Aldrich) for 1 h at room temperature. DNA was digested using 10 U NlaIII (NEB) in 1x CutSmart buffer (NEB) over night at 37 °C. Reaction was heat-inactivated for 20 min at 80 °C. NlaIII-specific hairpin-linker (50 pmol) was ligated (T4 DNA Ligase, NEB) over night at 16 °C. Subsequently, bisulfite treatment was performed on both, BAS and BHAS samples, using ZYMO RESEARCH "EZ DNA Methylation-Gold Kit" according to manufacturer's instructions. Bisulfite-treated DNA was eluted and *FOXP3-TSDR* bisulfite amplicons were generated by PCR. PCR Amplicons were purified (for BAS: QIAquick PCR Purification Kit (Qiagen Germany, 28106); for BHAS: Excision of product-specific bands from an agarose gel and purification using Gel/PCR DNA Fragments Extraction Kit (Avegene)). Amplicons were subjected to next-generation sequencing (paired-end; 2x300bp). Reads of BAS samples were aligned and evaluated using the bis-mark package.<sup>84</sup> For BHAS, methylation information was extracted using BiQ Analyzer HT.<sup>85</sup>

### Array-based genotyping and HLA imputation

DNA was extracted by the DNA laboratory of the Institute of Clinical Molecular Biology (Kiel University, Kiel, Germany) from whole blood or PBMCs. Genotyping was performed using the Infinium Global Screening Array-24 (GSA), version 3.0 (Illumina). Imputation of alleles in the HLA region was performed for the classical HLA class I loci HLA-A, -B, -C and the class II loci HLA-DQA1, -DQB1, -DPA1, -DPB1, -DRB1 at 2-field full context resolution from quality-controlled SNP genotype data. Pre-imputation SNP genotypes from the extended HLA region (chromosome 6: 29–34Mb) were extracted and used as input for HLA genotype prediction with the random-forest based machine learning tool HIBAG (version 1.20.0) using the multi-ethnic reference model published by Degenhardt et al.,<sup>86</sup> which was modified to include the variants available on the GSA. Classical HLA alleles with a marginal posterior probability from imputation <0.3 were excluded.

### Single-cell RNA-seq assay (Smart-seq2)

For single-cell RNA-seq, PBMCs were stimulated for 6 h, CD154+ memory cells were isolated by MACS and further purified by FACS sorting on a FACS Aria Fusion (BD Bioscience, San Jose, CA, USA) based on dual expression of CD154 and CD69 and expression of CD45RO. Cells were directly sorted into skirted 96-well PCR plates which were equipped with 2  $\mu$ l lysis buffer (nuclease-free water with 0.2% Triton-X 100 solution (Roche Diagnostics GmbH, Mannheim, Germany) with 4 U/ $\mu$ L RNase Inhibitor (New England Biolabs)) in advance. After FACS sorting, plates were shortly centrifuged (30 sec, 200xg) and immediately frozen at  $-80^{\circ}\text{C}$  until shipment. Library preparation and sequencing was performed at the DRESDEN-*concept* Genome Center (DcGC, TU Dresden, Germany). The workflow was based on the previously described SMARTseq2 protocol.<sup>87</sup> After thawing the samples, 2  $\mu$ l of a primer mix was added (5 mM dNTP (Invitrogen), 0.5  $\mu$ M dT-primer\*, 4 U RNase Inhibitor (NEB)). RNA was denatured for 3 minutes at  $72^{\circ}\text{C}$  and the reverse transcription was performed at  $42^{\circ}\text{C}$  for 90 min after filling up to 10  $\mu$ l with RT buffer mix for a final concentration of 1X superscript II buffer (Invitrogen), 1 M betaine, 5 mM DTT, 6 mM  $\text{MgCl}_2$ , 1  $\mu$ M TSO-primer\*, 9 U RNase Inhibitor and 90 U Superscript II. After synthesis, the reverse transcriptase was inactivated at  $70^{\circ}\text{C}$  for 15 min. The cDNA was amplified using 2X Kapa HiFi HotStart Readymix (Roche) at a final 1X concentration and 0.1  $\mu$ M UP-primer\* under following cycling conditions: initial denaturation at  $98^{\circ}\text{C}$  for 3 min, 22 cycles [ $98^{\circ}\text{C}$  20 sec,  $67^{\circ}\text{C}$  15 sec,  $72^{\circ}\text{C}$  6 min] and final elongation at  $72^{\circ}\text{C}$  for 5 min. The amplified cDNA is purified using 0.6X volume of hydrophobic Sera-Mag Beads (Cytiva: GE24152105050250,) and DNA was eluted in 12  $\mu$ l nuclease free water. The cDNA quality and concentration of a few representative samples was determined with the Fragment Analyzer (Agilent).

For library preparation, 2  $\mu$ l amplified cDNA was tagmented in 1X Tagmentation Buffer using 0.8  $\mu$ l bead-linked transposome (Illumina DNA Prep, (M) Tagmentation, Illumina) at  $55^{\circ}\text{C}$  for 15 min in a total volume of 4  $\mu$ L. The reaction was stopped by adding 1  $\mu$ l of 0.1 % SDS ( $37^{\circ}\text{C}$ , 15 min). Magnetic beads were bound to a magnet, the supernatant was removed, beads were resuspended in 4  $\mu$ l indexing PCR Mix containing 1x KAPA HiFi HotStart Ready Mix (Roche). After adding 700 nM unique dual indexing primers (i5 and i7) using Echo Acoustic Liquid Handler (Echo 525, Beckman Coulter), the reaction mixture was subjected to a PCR ( $72^{\circ}\text{C}$  3 min,  $98^{\circ}\text{C}$  30 sec, 12 cycles [ $98^{\circ}\text{C}$  10 sec,  $63^{\circ}\text{C}$  20 sec,  $72^{\circ}\text{C}$  1 min],  $72^{\circ}\text{C}$  5 min). After PCR, libraries are quantified with a Tecan plate reader Infinite 200 pro in 384 well black flat bottom low volume plates (Corning) using AccuBlue Broad range chemistry (Biotium) and equimolarly pooled using Echo Acoustic Liquid Handler (Echo 525, Beckman Coulter GmbH).

The pooled libraries were then purified with 0.9x volume Sera-Mag SpeedBeads, followed by a double size selection with 0.6x and 0.9x volume of beads. Re-double size selection with 0.6x and 0.9x volume of beads was performed if needed. Sequencing was performed after quantification using a Fragment Analyzer on an Illumina Novaseq 6000 aiming at an average sequencing depth of 0.5 mio 100 bp paired-end fragments per cell.

dT-primer: C6-aminolinker-AAGCAGTGGTATCAACGCAGAGTTCGAC TTTTTTTTTTTTTTTTTTTTTTTTTTTTTTTTTTTVN, where N represents a random base and V any base beside thymidine;

TSO-primer: AAGCAGTGGTATCAACGCAGAGTGCAGTGCT CGTGATrGrGrG, where rG stands for ribo-guanosine;

UP-primer: x-AAGCAGTGGTATCAACGCAGAG\*T where x stands for C6-Amino-link and \* for PTO-Binding

### Single-cell transcriptome and TCR repertoire data analysis

Fragments were aligned to the human reference genome hg38 with support of Ensembl 98 splice sites using the aligner gsnap (v2019-06-10).<sup>88</sup> Counts per gene and cell were obtained based on the overlap of the uniquely mapped fragments with the same Ensembl annotation using featureCounts (v2.0.1).<sup>89</sup> T cell receptor sequences were assembled per cell using TraCeR (v0.5).<sup>90</sup>

Based on the raw counts, the main analyses were performed with the R package Seurat v4.3.0.<sup>91</sup> Exclusively features detected in at least 1% of the cells and cells with less than 10% mitochondrial gene expression, at least 500 covered features, and 10,000 reads were considered for further analyses. After normalizing and scaling the data with the R functions NormalizeData and ScaleData, dimensionality reduction was performed with RunPCA based on the top 5% of the most variable genes. To control for the technical bias caused by different sequencing runs, the R package harmony v0.1.1<sup>92</sup> was applied. Ribosomal genes were excluded from all analyses.

The principal component analysis (PCA) was performed using the R function prcomp. Differentially expressed genes were determined using the FindMarkers function from the Seurat package with the option MAST based on all genes that were detected in a fraction of at least 0.1 cells in either of the two conditions. The differentially expressed genes (adjusted p values < 0.05) were uploaded in the IPA (Ingenuity Pathway Analysis version 45868156) software.<sup>93</sup> A selected subset of the top enriched canonical pathways was plotted using ggplot2 R package<sup>94</sup> (Figure 2B). Normalized expression values were scaled to z-scores using the R function scale and visualized in bubble plots. The cells with a normalized count >0.01 were considered positive. The protein-protein interaction network was created with the R package igraph v1.4.1 using the Fruchterman-Reingold layout algorithm. Single nodes were removed from the figure. The lines indicate a connection between genes based on the STRING database v10<sup>95</sup> using medium confidence. The trajectory analysis was performed with the R package monocle3 v1.3.1<sup>96,97</sup> using selected immunological genes as shown in Figure 2E. The starting point was chosen with the R function order\_cells and is the cell in the main trajectory path with the largest distance to the Treg group. In the heatmap showing the gene expression values in relation to the pseudotime, a sliding window approach was applied with a window size equal to 10. The genes were ordered by hierarchical clustering. Metasignature analyses were based on the sum of rank normalized expression values for each investigated gene group.

The TCR network plots were created using igraph v1.4.1. package (one edge per TCR clone). The size of the nodes shows the TCR clonality (number of cells with the same VDJ sequence for both alpha and beta strands). The shared clone sizes are the sum of the clonality of both groups.

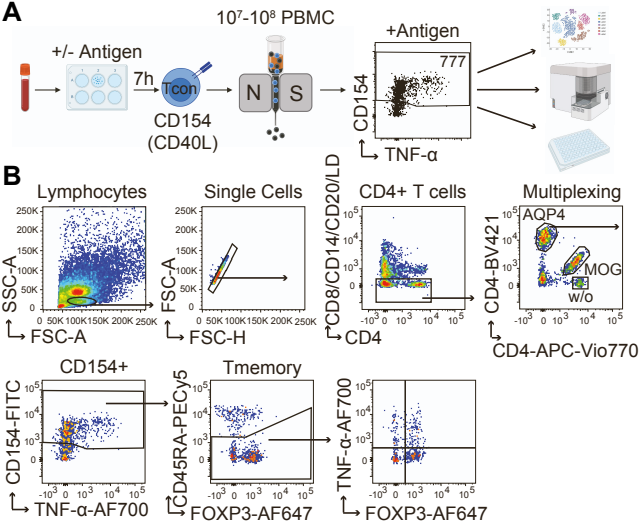
### QUANTIFICATION AND STATISTICAL ANALYSIS

Flow cytometry data were analyzed with FlowJo software version 10.7.1. (Treestar, Ashland, OR, USA). For statistical analysis GraphPad PRISM software version 9.5.1. (GraphPad Software, La Jolla, CA, USA) was used. Statistical parameters including the exact value of  $n$ , the definition of center, dispersion and precision measure, and statistical significance are reported in the Figures and the Figure Legends. Statistical tests were selected based on appropriate assumptions regarding data distribution and variance characteristics. Significance was set at  $p < 0.05$ .

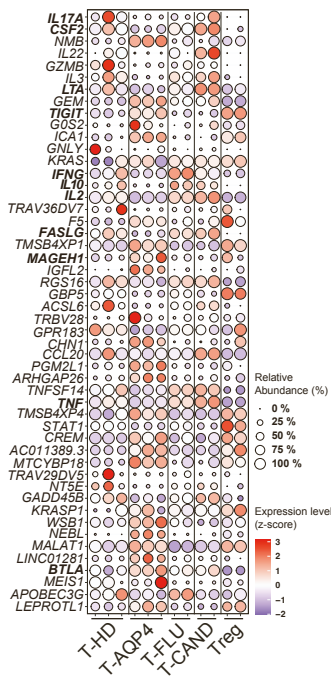
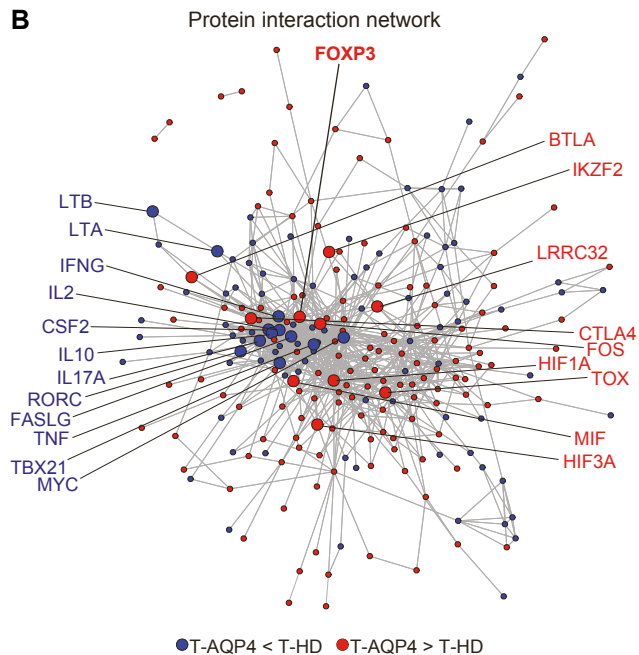
## Supplemental information

### **Autoantigen-specific CD4<sup>+</sup> T cells acquire an exhausted phenotype and persist in human antigen-specific autoimmune diseases**

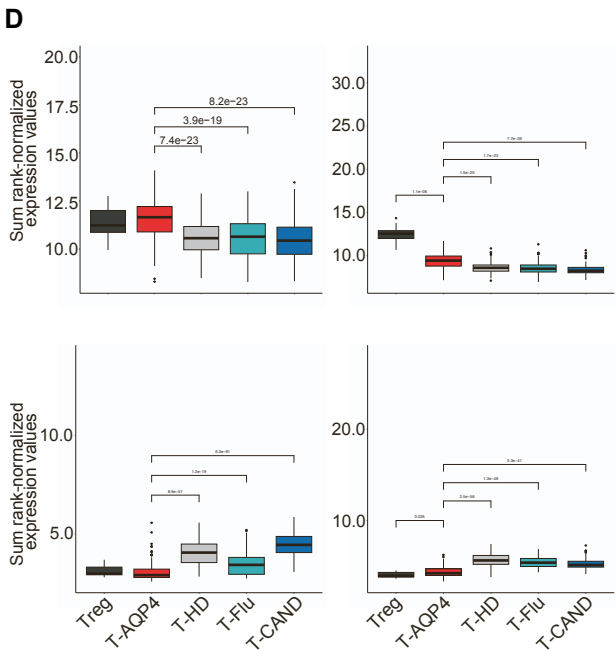
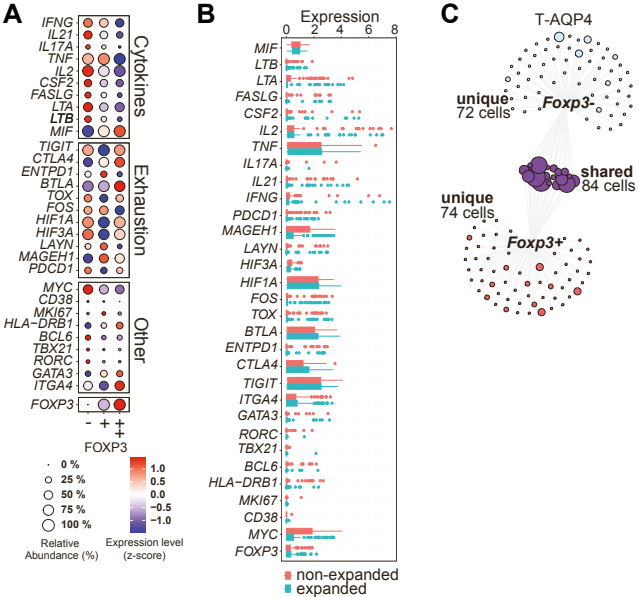
**Carina Saggau, Petra Bacher, Daniela Esser, Mahdi Rasa, Silja Meise, Nicola Mohr, Nora Kohlstedt, Andreas Hutloff, Sarah-Sophie Schacht, Justina Dargvainiene, Gabriela Rios Martini, Klarissa H. Stürner, Ina Schröder, Robert Markewitz, Johannes Hartl, Maria Hastermann, Ankelien Duchow, Patrick Schindler, Mareike Becker, Carolin Bautista, Judith Gottfreund, Jörn Walter, Julia K. Polansky, Mingxing Yang, Reza Naghavian, Mareike Wendorff, Ev-Marie Schuster, Andreas Dahl, Andreas Petzold, Susanne Reinhardt, Andre Franke, Marek Wieczorek, Lea Henschel, Daniel Berger, Guido Heine, Maïke Holtsche, Vivien Häußler, Christian Peters, Enno Schmidt, Simon Fillatreau, Dirk H. Busch, Klaus-Peter Wandinger, Kilian Schober, Roland Martin, Friedemann Paul, Frank Leypoldt, and Alexander Scheffold**



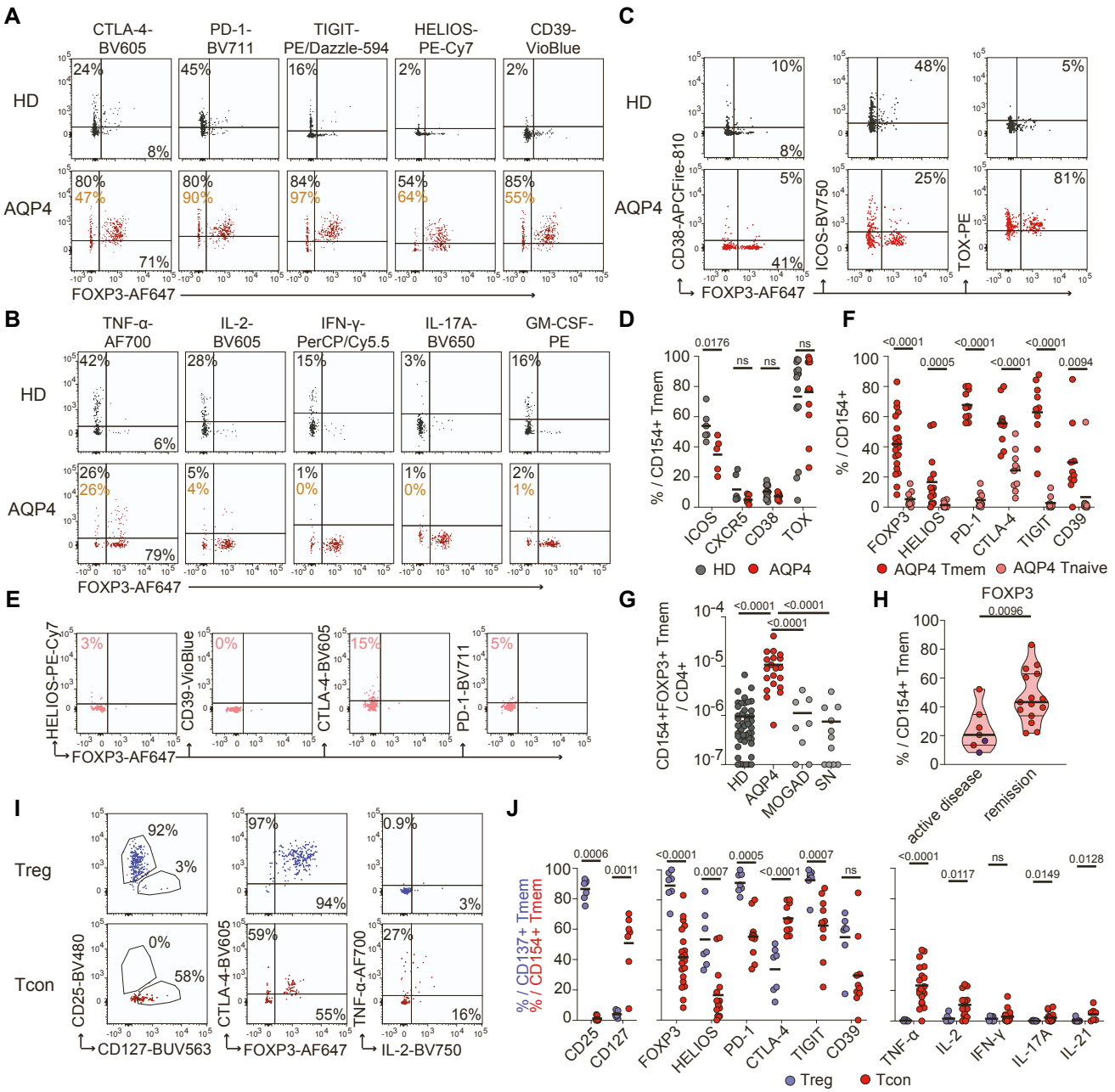
**Supplemental Figure 1: Antigen-reactive T cell enrichment (ARTE), related to Figures 1-6. (A)** Schematic of ARTE: PBMCs were stimulated with or without AQP4 or MOG peptide pools for 7 hours and reactive T cells were detected according to upregulation of CD154 (CD40L). CD154<sup>+</sup> cells were magnetically enriched from 25-50 million PBMCs. Dotplot example shows AQP4-reactive CD154<sup>+</sup> cells after magnetic enrichment. Absolute cell count of CD154<sup>+</sup> isolated from 50 million PBMCs is indicated. Figure created with Biorender.com. **(B)** Gating strategy of AQP4-reactive T cells detected by ARTE including multiplexing of differently stimulated samples (w/o antigen, MOG, AQP4). For Multiplexing cells were labeled with different CD4-antibodies and mixed.

**A****B**

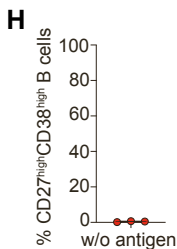
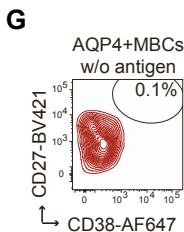
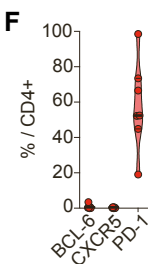
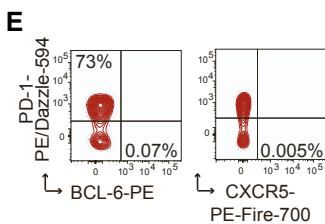
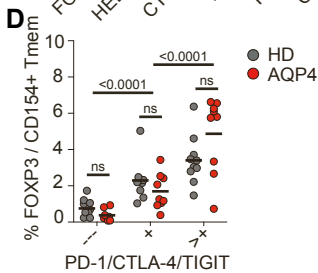
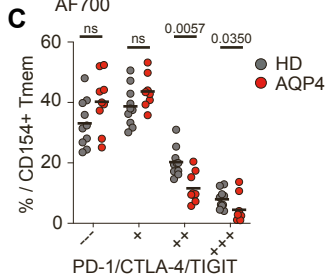
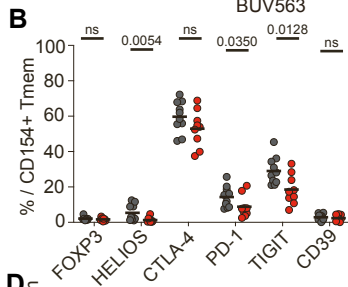
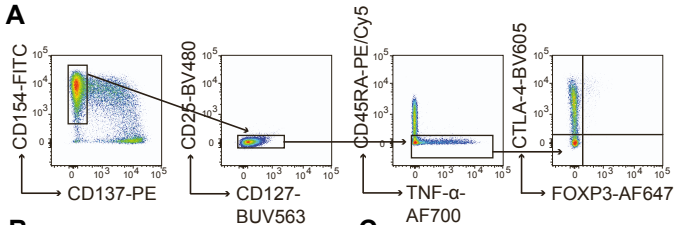
**Supplemental Figure 2: Top50 differentially expressed genes between T-AQP4 and T-HD and protein network interaction analysis, related to Figure 2. (A)** Bubble plot showing the normalized expression of the Top50 differentially expressed genes of AQP4-reactive CD154+ T cells between healthy donors (T-HD; n=3) and AQP4-NMOSD patients (T-AQP4; n=3) according to fold change (adjusted p-values <0.05). Normalized expression of the same genes of *Influenza*- (T-FLU; n=2) and *C. albicans*-specific T cells (T-CAND; n=2) as well as polyclonally activated Tregs (Treg; n=2) were plotted as control. The size of the bubble shows the proportion of cells expressing the respective gene, and the colors show the relative average expression of the genes in all the cells belonging to each group. **(B)** Undirected bioinformatic protein network analysis based on all differentially expressed genes between healthy donors (T-HD) and AQP4-NMOSD patients (T-AQP4).



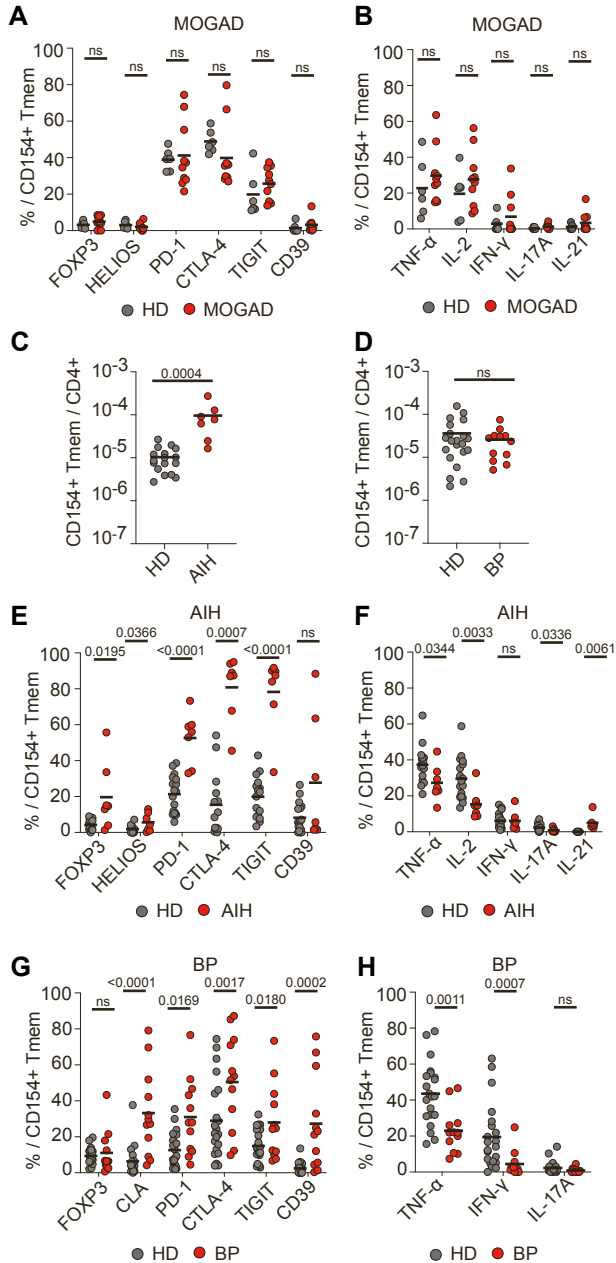
**Supplemental Figure 3: Developmental trajectory of ThEx cells supported by TCR clonality data, related to Figure 2. (A)** Bubble plot showing the normalized expression of selected marker genes in AQP4-reactive CD154+ T cells of AQP4-NMOSD patients (T-AQP4; n=3) according to their normalized expression of *FOXP3* (*FOXP3*- (-), *FOXP3* intermediate (+) *FOXP3* high (++)). The size of the bubble shows the proportion of cells expressing the respective gene, and the colors show the relative average expression of the genes in all the cells belonging to each group. **(B)** Box plots showing the normalized expression of selected marker genes comparing clonally expanded (clone frequency>1) and non-expanded (clone frequency=1) T cell receptors within T-AQP4 cells. **(C)** T cell receptor (TCR) network plot of AQP4-reactive CD154+ T cells from AQP4-NMOSD patients (T-AQP4; n=3) comparing the TCRs of *FOXP3*+ and *FOXP3*- AQP4-reactive T cells. Each node indicates one TCR clone. The size of the node shows the TCR clonality. Blue color indicates uniquely *FOXP3*- TCRs, pink color indicates uniquely *FOXP3*+ TCRs and purple color indicates TCRs shared between *FOXP3*+ and *FOXP3*-. **(D)** Gene signature analysis: boxplots comparing AQP4-reactive CD154+ T cells from NMOSD patients (T-AQP4; n=3) and healthy donors (T-HD; n=3) with *C. albicans*-reactive T cells (T-CAND; n=2), *Influenza*-reactive T cells (T-Flu; n=2) and polyclonally activated CD137+ Tregs (Treg; n=2). Shown is the sum of rank normalized expression values based on 4 selected gene groups representing the different Th subset signatures (Tfh, Treg, Th1, Th17).



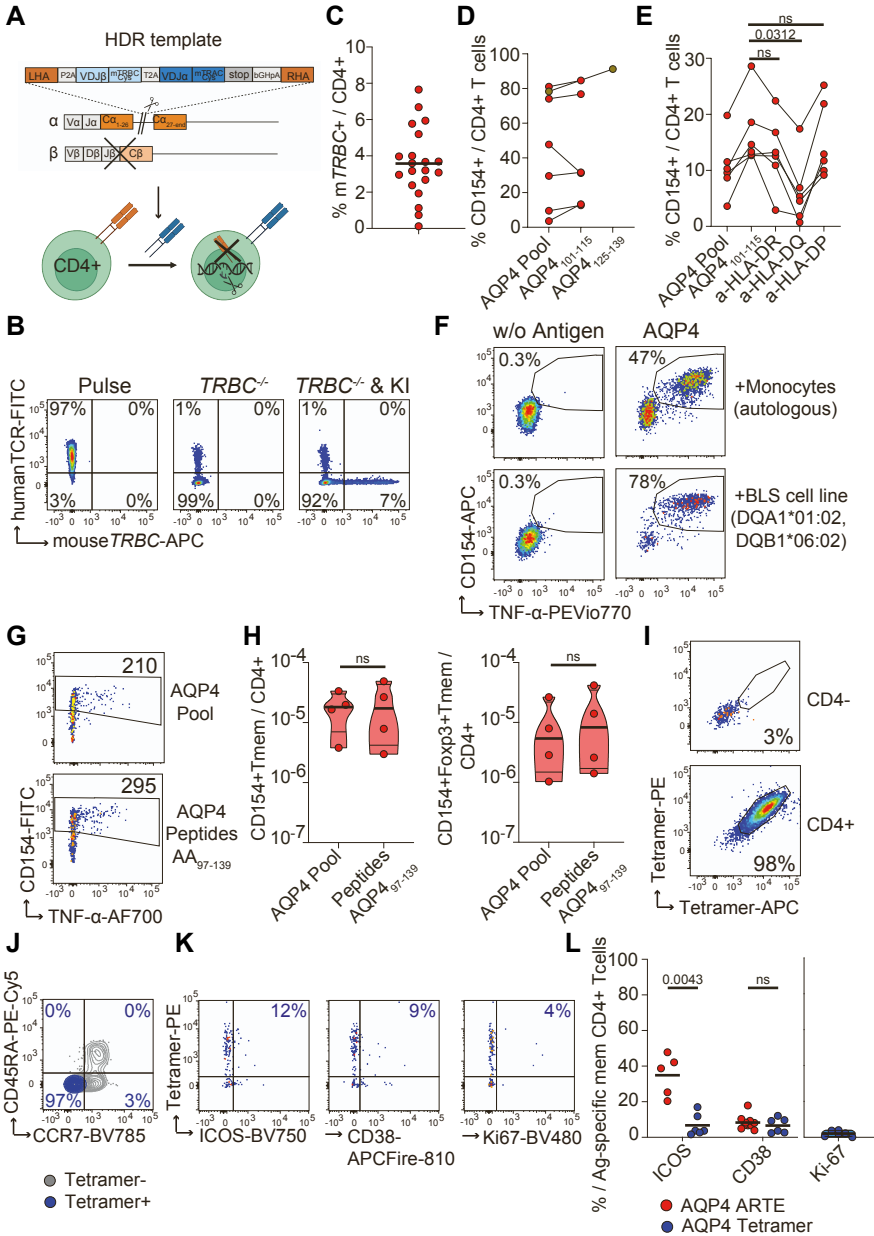
**Supplemental Figure 4: Flow cytometric analysis of AQP4-reactive CD4+ T cells following ARTE, related to Figure 3.** Dotplot examples of **(A)** *ex vivo* co-inhibitory receptor (CTLA-4, PD-1, TIGIT), FOXP3, HELIOS and CD39 or **(B)** *ex vivo* cytokine expression by AQP4-reactive CD154+ Tmem in healthy donors (HD) and AQP4-NMOSD patients (AQP4) detected by ARTE. Percentages of cells within all CD154+Tmem (black) and within CD154+FOXP3+ Tmem (orange) are indicated. **(C)** Dotplot examples of *ex vivo* expression of chronic activation markers CD38 and ICOS and transcription factor TOX by AQP4-reactive CD154+ Tmem in healthy donors (HD) and AQP4-NMOSD patients (AQP4) detected by ARTE. **(D)** Proportion of ICOS, CXCR5, CD38 and TOX expression within AQP4-reactive CD154+ Tmem in healthy donors (HD; n=6-17) and AQP4-NMOSD patients (AQP4; n=5-12). **(E)** Dotplot examples of *ex vivo* expression of HELIOS, CD39, CTLA-4 and PD-1 of AQP4-reactive naïve CD154+ T cells detected by ARTE. Percentage within naïve CD154+ T cells is indicated. **(F)** Comparison between CD45RA+ naïve (Tnaive; n=10) and CD45RA- memory (Tmem; n=11-20) CD154+ T cells in AQP4-NMOSD patients (AQP4). **(G)** Frequencies of AQP4-reactive CD154+FOXP3+CD45RA- memory (Tmem) CD4+ T cells in healthy donors (HD; n=48) and NMOSD patients n=39 (AQP4; n=20, MOG antibody-associated disease (MOGAD); n=8, seronegative (SN); n=11). **(H)** Proportion of FOXP3 expression within AQP4-reactive CD154+ Tmem from AQP4-NMOSD patients according to their clinical status, active disease (n=7, new onset, or relapse, <3 month since last disease flare, one patient was measured twice during active disease indicated by purple color of the dots) and stable remission (n=15). **(I)** Dotplot examples of *ex vivo* CD25, CD127, CTLA-4, FOXP3, IL-2 and TNF- $\alpha$  expression by AQP4-reactive CD154+ Tmem (Tcon) and CD137+ Tmem (Tregs) in AQP4-NMOSD patients detected by ARTE. Percentages of cells within all CD154+ Tcon and CD137+ Tregs are indicated. **(J)** *Ex vivo* proportion of CD25, CD127, FOXP3, HELIOS, co-inhibitory receptor (CTLA-4, PD-1, TIGIT) and CD39 as well as cytokine (TNF- $\alpha$ , IL-2, IFN- $\gamma$ , IL-17A, IL-21) expressing cells within AQP4-reactive CD154+ Tmem and CD137+ Tmem in AQP4-NMOSD patients (Tcon; n=7-20, Treg; n=7). Each symbol in **(D, F, G, H, J)** represents one donor, horizontal lines indicate mean. Truncated violin plots with quartiles and range are shown in **(H)**. Statistical differences: Two-tailed Mann-Whitney test or unpaired t test in **(D, F, G, H, J)**. Decision was based on an upstream normal distribution test.



**Supplemental Figure 5: Low frequencies of ThEx cells can be found upon polyclonal stimulation of CD4 memory T cells in healthy donors and NMOSD patients and T cell/B cell cooperation assay, related to Figure 4. (A)** Gating strategy of PMA and Ionomycin activated CD4 memory T cells. **(B)** *Ex vivo* proportion of FOXP3, HELIOS, co-inhibitory receptor (CTLA-4, PD-1, TIGIT) and CD39 expressing cells within polyclonally activated CD154+ Tmem from healthy donors (HD; n=10) and AQP4-NMOSD patients (AQP4; n=9). **(C)** *Ex vivo* proportion of cells expressing none, single, double, or triple co-inhibitory receptors (CTLA-4, PD-1 or TIGIT) within polyclonally activated CD154+ Tmem in healthy donors (HD; n=10) and AQP4-NMOSD patients (AQP4; n=9) **(D)** Proportion of FOXP3 positive polyclonally activated CD154+ Tmem from healthy donors (HD; n=10) and AQP4-NMOSD patients (AQP4; n=9) expressing none, single or >1 co-inhibitory receptor (PD-1, CTLA-4 or TIGIT). **(E)** Contour plot examples of Tfh marker (PD-1, CXCR5, BCL-6) expression of expanded AQP4-reactive T cell clones. Percentages within CD4+ T cells are indicated. **(F)** Proportion of Tfh marker (BCL-6, CXCR5, PD-1) expression within CD4+ T cells of expanded AQP4-reactive T cell clones (n=7). **(G)** Contour plot example of CD27 and CD38 staining showing the co-culture of one AQP4-reactive T cell clone with heterologous memory B cells in absence of the antigen (AQP4). Percentage of CD27<sup>high</sup>CD38<sup>high</sup> plasmablasts is indicated. **(H)** Proportion of CD27<sup>high</sup>CD38<sup>high</sup> memory B cells co-cultured with AQP4-reactive T cells clones in absence of the antigen (AQP4) (n=3). Each symbol in **(B, D)** represents one T cell clone. Truncated violin plots with quartiles and range are shown in **(B)**. Each symbol in **(B-D)** represents one donor, horizontal lines indicate mean. Statistical differences: Two-tailed Mann-Whitney test or unpaired t test in **(B-D)**. Decision was based on an upstream normal distribution test. Each symbol in **(F, H)** represents one T cell clone. Truncated violin plots with quartiles and range are shown in **(F)**.



**Supplemental Figure 6: Flow cytometric analysis of SLA-, BP180- and MOG-reactive CD4+ T cells following ARTE, related to Figure 5.** *Ex vivo* cytometric characterization of SLA-, BP180- and MOG-reactive CD154+ T cells following ARTE. **(A)** *Ex vivo* proportion of FOXP3, HELIOS, co-inhibitory receptor (CTLA-4, PD-1, TIGIT) and CD39 expressing cells within MOG-reactive CD154+ Tmem from healthy donors (HD; n=) and MOGAD patients (MOGAD; n=). **(B)** *Ex vivo* Cytokine expression (TNF- $\alpha$ , IL-2, IFN- $\gamma$ , IL-17A, IL-21) of MOG-reactive CD154+ Tmem in healthy donors (HD; n=6) and MOGAD patients (MOGAD; n=10). **(C)** Frequencies of SLA-reactive CD154+CD45RA- memory CD4+ T cells (Tmem) in healthy donors (HD; n=17) and AIH patients (n=7). **(D)** Frequencies of BP180-reactive CD154+CD45RA- memory CD4+ T cells (Tmem) in healthy donors (HD; n=21) and BP patients (n=12). **(E)** *Ex vivo* proportion of FOXP3, HELIOS, co-inhibitory receptor (CTLA-4, PD-1, TIGIT) and CD39 expressing cells within SLA-reactive CD154+ Tmem from healthy donors (HD; n=14-17) and AIH patients (AIH; n=7). **(F)** *Ex vivo* Cytokine expression (TNF- $\alpha$ , IL-2, IFN- $\gamma$ , IL-17A, IL-21) of SLA-reactive CD154+ Tmem in healthy donors (HD; n=4-17) and AIH patients (AIH; n=7). **(G)** *Ex vivo* proportion of FOXP3, CLA, co-inhibitory receptor (CTLA-4, PD-1, TIGIT) and CD39 expressing cells within BP180-reactive CD154+ Tmem from healthy donors (HD; n=21) and BP patients (BP; n=12). **(H)** *Ex vivo* Cytokine expression (TNF- $\alpha$ , IFN- $\gamma$ , IL-17A) of BP180-reactive CD154+ Tmem in healthy donors (HD; n=21) and BP patients (BP; n=12). Each symbol in **(A-H)** represents one donor, horizontal lines indicate mean. Statistical differences: Two-tailed Mann-Whitney test or unpaired t test in **(A-H)**. Decision was based on an upstream normal distribution test.



**Supplemental Figure 7: Identification of immunodominant AQP4 epitopes in NMOSD patients via orthotopic T cell receptor (TCR) replacement, related to Figure 6.**

**(A)** Schematic of the TCR replacement including the homology-directed repair (HDR) template design: The HDR template comprises the full length of the  $\alpha$ - and  $\beta$ -chains of the inserting TCRs flanked by left and right homology arms (LHA and RHA) and contains self-cleaving peptides (P2A and T2A), as well as a poly-A tail (bGHpA). The  $\beta$ -chain consists of the human variable region and the murine constant region, which is used as tracking marker. Clonally expanded TCRs from three AQP4-NMOSD patients were re-expressed via orthotopic TCR replacement using CRISPR/Cas9 knock-in into the *TCRA*-locus of primary CD4<sup>+</sup> T cells, and simultaneous *TCRB*-locus<sup>-/-</sup> leading to exclusive expression of the transgenic TCR. Figure created with Biorender.com. **(B)** Dotplot examples of human and mouse TCR staining in TCR-transgenic cells of the pulse control, the *TCRB*<sup>-/-</sup> only control of the endogenous TCR and the simultaneous *TCRB*<sup>-/-</sup> of the endogenous TCR and Knock-in (KI) of the AQP4-specific transgenic TCR. The transgenic TCRs consist of the human variable region and the murine constant region. **(C)** Proportion of mouse TRBC+CD4<sup>+</sup> T cells after TCR replacement via CRISPR/Cas9 shown for all TCRs replaced from 3 AQP4-NMOSD patients (n=20). **(D)** Identification of two immunodominant peptides (AQP4<sub>101-115</sub> and AQP4<sub>125-139</sub>) in one AQP4-NMOSD patient by restimulation of TCR-transgenic T cells (n=7) with the AQP4 peptide pool and single peptides covering the complete protein sequence. **(E)** Proportion of CD154<sup>+</sup> T cells of expanded AQP4-specific TCR-transgenic cells (n=6) of one AQP4-NMOSD patient restimulated with the whole AQP4 peptide pool or the identified immunodominant peptide (AQP4<sub>101-115</sub>) with and without HLA blocking antibodies. **(F)** Dotplot examples of the restimulation of AQP4-reactive T cell clones in presence of autologous monocytes or DQw6 BLS cells. Percentages of CD154+TNF- $\alpha$ + T cells are indicated. **(G)** Dotplot examples of the *ex vivo* detection of AQP4-reactive CD4<sup>+</sup> T cells by ARTE. Absolute cell counts after magnetic enrichment from 2.5x10<sup>7</sup> PBMCs stimulated with the whole AQP4 peptide pool or a selection of six peptides are indicated. **(H)** Comparison of frequencies of AQP4-reactive CD154<sup>+</sup> Tmem and CD154+FOXP3<sup>+</sup> Tmem in HLA-DQ6<sup>+</sup> AQP4-NMOSD patients (n=4) stimulated with the whole AQP4 peptide pool versus six selected peptides (AQP4<sub>97-139</sub>). **(I)** Dotplot examples of tetramer staining of TCR-transgenic CD4<sup>+</sup> T cells. Percentage of tetramer+ cells within CD4<sup>+</sup> and CD4<sup>-</sup> T cells is indicated. **(J)** Contour plot example of CD45RA and CCR7 staining of antigen-specific CD4<sup>+</sup> T cells detected via tetramer enrichment overlaid with two different colors representing tetramer APC/PE double positive cells (blue) and tetramer- cells (grey). **(K)** Dotplot examples of antigen-specific CD4<sup>+</sup> T cells in AQP4-NMOSD patients detected by tetramer enrichment. Percentages of cells within tetramer APC/PE double positive cells are indicated. **(L)** Comparison of the proportion of ICOS, CD38 and Ki-67 expression within antigen-specific CD4<sup>+</sup> T cells detected by ARTE or tetramer enrichment in AQP4-NMOSD patients (AQP4 ARTE; n=5-10, AQP4 tetramer; n=6). For Ki-67 no ARTE data is available. Each symbol in **(H, L)** represents one donor. Each symbol in **(C, D, E)** represents one replaced TCR. Horizontal lines indicate mean. Truncated violin plots with quartiles and range are shown in **(H)**. Statistical differences: Two-tailed Mann-Whitney test in **(E, H, L)**.